Title
FMCW Lidar: Scaling to the Chip-Level and Improving Phase-Noise-Limited Performance

Author
Sandborn, Phillip Alan McGinnis

Publication Date
2017

Peer reviewed|Thesis/dissertation

FMCW Lidar: Scaling to the Chip-Level and Improving Phase-Noise-Limited Performance

By

Phillip Alan McGinnis Sandborn

A dissertation submitted in partial satisfaction of the

requirements for the degree of

Doctor of Philosophy

in

Engineering – Electrical Engineering and Computer Sciences

in the

Graduate Division

of the

University of California, Berkeley

Committee in charge:

Professor Ming C. Wu, Chair
Professor Bernhard E. Boser
Professor Kris J. Pister
Professor Liwei Lin

Fall 2017

Abstract

FMCW Lidar: Scaling to the Chip-Level and Improving Phase-Noise-Limited Performance

by

Phillip A.M. Sandborn

Doctor of Philosophy in Electrical Engineering

University of California, Berkeley

Professor Ming C. Wu, Chair

Lidar (light detection and ranging) technology has the potential to revolutionize the way automated systems interact with their environments and their users. Most lidar systems in the industry today rely on pulsed (or, "time-of-flight") lidar, which has reached limits in terms of depth resolution. Coherent lidar schemes, such as frequency-modulated continuous-wave (FMCW) lidar, offer significant advantage in achieving high depth resolution, but are often too complex, too expensive, and/or too bulky to be implemented in the consumer industry. FMCW, and its close cousin, swept-source optical coherence tomography (SS-OCT) are often targeted towards metrology applications or medical diagnostics, where systems can easily cost upwards of $30,000.

In this dissertation, I present my work in chip-scale integration of optical and electronic components for application in coherent lidar techniques. First, I will summarize the work to integrate a typically bulky FMCW lidar control system onto an optoelectronic chip-stack. The chip-stack consists of an SOI silicon-photonics chip and a standard CMOS chip. The chip was used in an imaging system to generate 3D images with as little as 10um depth precision at stand-off distances of 30cm.

Second, I will summarize my work in implementing and analyzing a new post-processing method for FMCW lidar signals, called "multi-synchronous re-sampling" (MK-re-sampling). This involved Monte Carlo studies of laser phase noise under non-linear signal processing schemes, so I will show stochastic simulations and experimental results to demonstrate the advantages of the new re-sampling method. QS-re-sampling has the potential to improve acquisition rate, accuracy, SNR, and dynamic depth range of coherent imaging systems.

To my inspiration and foundation: Mom and Dad

Table of contents

List of figures

List of tables

Acknowledgments

These things never happen in a void.

I need to thank countless people, including advisors, colleagues, friends, and family. First, I'm grateful to Prof. Ming Wu, my advisor throughout my graduate school career. He always offers grounded advice. In addition, I'm thankful to my dissertation committee, who also comprised my Qualifying Committee: Profs. Bernhard Boser, Kris Pister, and Liwei Lin.

Throughout my graduate career, several colleagues deserve special shout-outs. Niels Quack, a post-doc in the Wu group when I first entered the program, fostered a sense of progress and team integrity in the EPHI project, and offered many hours of advice during our meetings at the I-House Bar. Behnam Behroozpour is an incredible peer, colleague, and friend. Behnam and I spent several years working together on FMCW Lidar, and we learned an incredible amount from each other. I will cherish that relationship as we move on in our careers. Also, my thanks goes out to the members of the Wu Group, the Chang-Hasnain Group, and the Yablonovitch Group, who made the 253m office a home of sorts for five and a half years.

The beginning of grad school at Berkeley was marked by the beginning of several friendships that will surely last beyond graduation – Eliot Bessette, Ethan Schaler, and Thomas Rembert have been there for so many good times, and I'll never forget the years we spent helping each other through the hardest parts of being graduate students, and laughing through the best parts of our twenties.

Half-way through grad school, I met Jeanmarie. No one has ever made me happier to be where I am, to be doing what I'm doing, with the people I do it with. Jeanmarie, you bring so much love into my life. Thank you for being there for me through thick and thin – I love you.

Lastly, I would not be where I am today without the love and support of my parents, Peter and Tammy Sandborn. Mom and Dad, so much of who I am today is a reflection of you, not only because of how you raised me, but also because of the solace and encouragement I receive from you from three-thousand miles away. I hope you are proud, and so I dedicate my dissertation to you both.

1 Introduction

1.1 3D Imaging as an Enabling Technology for Intelligent Machines

As computers, robots, and systems in general become more useful, more integrated, and more necessary as parts of our working, cultural, and social lives, we crave more natural and flexible experiences for interfacing with these systems. This represents a paradigm shift from designing so-called "user-input devices," such as the oft-referred-to keyboard and mouse, to designing "human-computer-interactions," reflecting the shifting roles of computers in our lives. This shift from "input" to "interaction" requires that computers and systems have the capability to understand, interpret, and themselves interact with users as well as the environments which they inhabit. An important aspect of this new paradigm of "interaction" is the ability to sense and interpret the physical environment, whether that is the ability to recognize objects, gestures, or other agents.

Three-dimensional imaging has emerged as a critical component of next-generation computers. As a sensing modality, it is a natural way for robots to find paths through dynamic human environments, and it is critical for mapping physically unknown spaces.
In this introduction, first, I will discuss a plethora of current applications of 3D imaging, in the hopes of demonstrating the emerging ubiquity of the technology; second, I will briefly discuss several sensing modalities which are not the focus of this dissertation. I will then introduce several light-based direct range measurement sensors (lidar). Lastly, I will discuss the emergence of integrated photonics, and explain its merits as a platform for developing and producing state-of-the-art 3D imaging sensors for the applications that are discussed.

1.1.1 Current Applications of 3D Imaging

3D imagers have applications that span myriad fields. In particular, market insight firms have identified consumer-grade lidar for 3D imaging as a technology that will be in high-demand for use in autonomous vehicles and driver-assist applications [1]. In addition to robotic navigation, 3D imaging has been found to be an invaluable technology for both professional and consumer applications. In particular, lidar for 3D imaging is evolving beyond its original use as an aerial 3D mapping tool and into a critical technology for imaging at distances from short (1 meter) to long (100s of meters).

Advanced driver assistance systems (ADAS) and self-driving vehicles have the potential to significantly reduce pedestrian-related vehicle accidents and fatalities [2], significantly decrease the net cost of commercial truck accidents [3], and improve traffic congestion in large urban areas [4]. ADAS-enabled vehicles and autonomous vehicles will likely be equipped with numerous imaging systems inside and outside the car. For example, several different imaging modalities, from stereo vision to scanning lidar, have been integrated into autonomous vehicles for use in navigation, localization, and object identification [5]. Range-finding systems have already been integrated into ADAS systems for adaptive cruise control (ACC), in which the vehicle can sense the range and velocity of objects in its vicinity and adjust its own acceleration in order to maintain safe following distances [6].

In medical applications, physicians and medical technicians often desire extremely high-resolution, non-invasive procedures for detecting and diagnosing patient medical problems. For example, ophthalmologists often diagnose eye-related issues by examining a cross-sectional or three-dimensional image of the patient's eye. This application requires short-range (<10cm) and

high range-precision (on the order of 1s to 10s of microns) in order to properly identify and possibly treat eye-related issues [7–10]. In dentistry and orthodontics, three-dimensional models of a patient's teeth are often taken using a mold impression, but three-dimensional imaging tools are becoming more important in securing "patient acceptance" of proper orthodontic therapy [11].

1.1.2 Overview of 3D Imaging and Sensing Technology

Depth imaging sensors take on many forms, and are often classified by their modalities – optical, ultrasonic, and radar are notable modalities for ranging. Optical modalities span a variety of technologies, from stereo imaging, structured light, reflectance modeling, and other camera-based imaging sensors, to direct measurement of distance using light, as is the case with time-of-flight lidar sensors. Ultrasound and radar are classical modalities which use the known wavespeed of a signal in a medium to calculate distance to various reflective targets. Stereo, structured light, and reflectance modeling are methods which infer 3D surfaces from two-dimensional projections, so they are sometimes referred to as indirect 3D imagers. In contrast, lidar, ultrasound, and radar, which return a direct measurement for range, can be referred to as direct 3D imagers. Myriad studies have examined the performance and limits of both indirect and direct 3D imagers, so we will dedicate the next section solely to the study of lidar time-of-flight sensors, which are most directly related to the topic of this dissertation.

1.2 Light-Based Direct Range Measurement Sensors (Lidar)

Lidar can take on several different modalities, which can be classified by their dependence on incoherence or coherence of the laser source which is used. Each of these methods uses the optical path of the target reflector to effectively modulate the envelope intensity of the detected signal. Time-of-flight (pulsed) and amplitude-modulated continuous-wave (AMCW) sensors detect range by measuring temporal properties of the received light intensity. Frequency-modulated continuous-wave (FMCW) and optical coherence tomographic (OCT) sensors map properties of the received optical field (amplitude and phase) into intensity, and attempt to leverage knowledge of both the amplitude and phase in order to detect range.

1.2.1 Pulsed Time-of-Flight (TOF)

TOF lidar uses the known fact that light travels at a fixed speed through a medium with a constant refractive index ($3x10^8$ m/s in air). Examples of pulsed time-of-flight (TOF) systems can be found in [12,13]. The transmitted pulse must be reflected by the target object, and collected by an aperture at the receiver. Range is measured by determining the difference in time of arrival and the time of transmission of the pulse. Fig. 1-1 shows a simple schematic outlining the operating principles of pulsed TOF lidar.

The pulse can be created by an incoherent LED source or a high-power mode-locked laser, depending on system cost, optical output power, or power consumption constraints. The depth resolution of such a system is limited by the timing resolution in electronics. This indicates that the minimum range that can be measured by TOF systems is limited to single centimeters. The maximum range of TOF systems is primarily limited by the link budget of the free-space path in the system. The loss of the free-space path often directly scales with the distance of the path. This means that the allowed transmitted power and receiver sensitivity together indicate a maximum range beyond which the amplitude of a target reflector is too low to detect. With typical receiver sensitivities in commercial TOF systems today, the maximum range is limited to

100-200 meters [13]. Higher-power systems for aerial mapping and other scientific endeavors, maximum range can be extended to several kilometers [14].

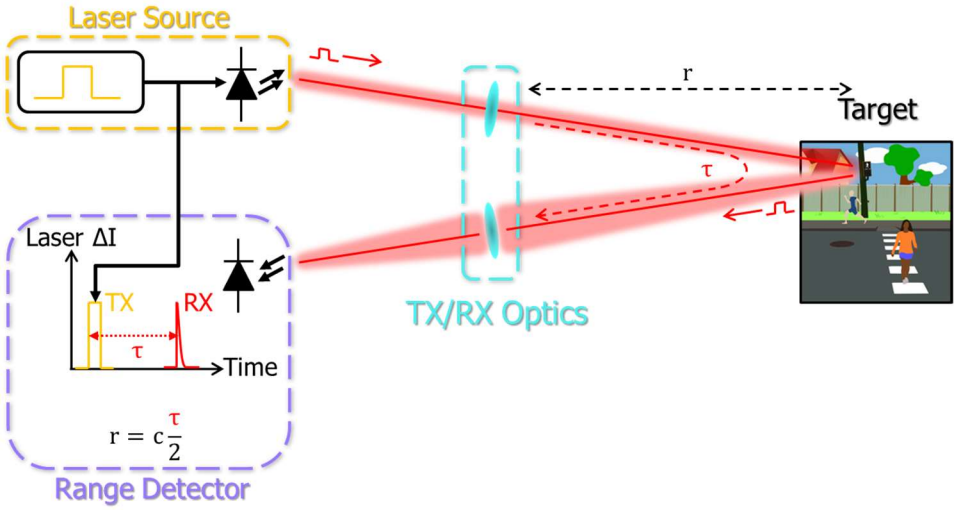

Fig. 1-1. Schematic for pulsed TOF lidar. A laser source transmits an optical pulse, which is reflected by a target surface. The difference between the transmit time and receive time encodes distance to the target.

1.2.2 Amplitude Modulated Continuous Wave (AMCW) Lidar

Amplitude-modulated continuous-wave (AMCW) lidar uses similar principles to TOF lidar, in that a target delay is measured at the receiver. However, in the case of AMCW, an intensity pattern is encoded on the transmitted optical power, such as a linear radio frequency chirp. For AMCW, the free-space path encodes a phase shift on the RF chirp, which can be detected accurately by measuring the intermediate frequency after mixing the received intensity signal with a non-delayed electronic version of the chirp. Examples of AMCW lidar systems have been studied in [15,16]. Fig. 1-2 shows a simple schematic outlining the operating principles of AMCW lidar.

The depth resolution of this implementation is limited by the system's capability to resolve the delay-induced phase shift. In the case of an RF chirp, the resolution is actually limited by the spread of frequencies exhibited by the chirp, B. For example, the resolution exhibited by a system with 1 GHz excursion on the RF chirp is 15 centimeters. In order to achieve single-centimeter resolution, it would be necessary to have an excursion on the order of 15 GHz, which quickly shows the limits of electronic amplitude-modulation.

The maximum range of AMCW systems can be limited by several factors. Similar to TOF systems, AMCW maximum range can be limited by the optical link budget. Less intuitively, and in the case of the RF-chirp system, the maximum range can be limited by the maximum frequency that can be detected at the receiver. By modifying the period of the RF-chirp, the maximum range can be extended, but at the cost of acquisition time.

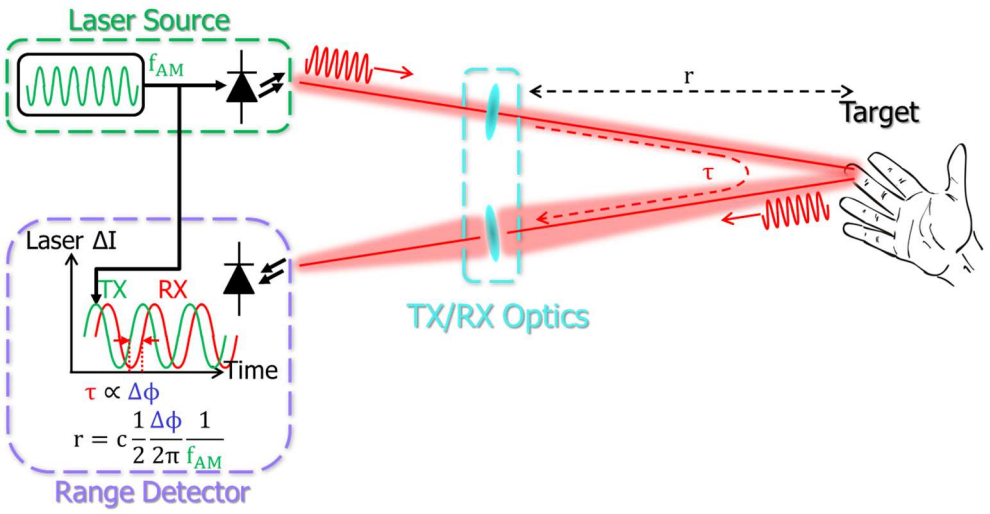

Fig. 1-2. Schematic for amplitude-modulated continuous-wave lidar. A laser source transmits an intensity modulated optical wave, which is reflected by a target surface. The difference between the transmitted signal phase and the received signal phase encodes distance to the target.

1.2.3 Frequency Modulated Continuous Wave (FMCW) Lidar

Frequency-modulated continuous-wave (FMCW) lidar can analytically be shown as a comparable method to RF-chirped AMCW lidar, except where the chirped field is the optical field of a tunable laser. Where chirped AM lidar uses the laser as a carrier for an RF signal, and the RF signal is applied to the intensity of the light source, chirped FM lidar modulates the phase of the light source (usually a single-mode laser) such that the optical frequency of the light source is modulated directly. A free-space path encodes a phase shift on the optical chirp, and the phase shift is detected by mixing the reflected chirp with a non-delayed version of the chirp. This mixing occurs at the photodiode upon detection, so no special design beyond good detector design is needed to achieve this mixing effect. A schematic for FMCW lidar is shown in Fig. 1-3.

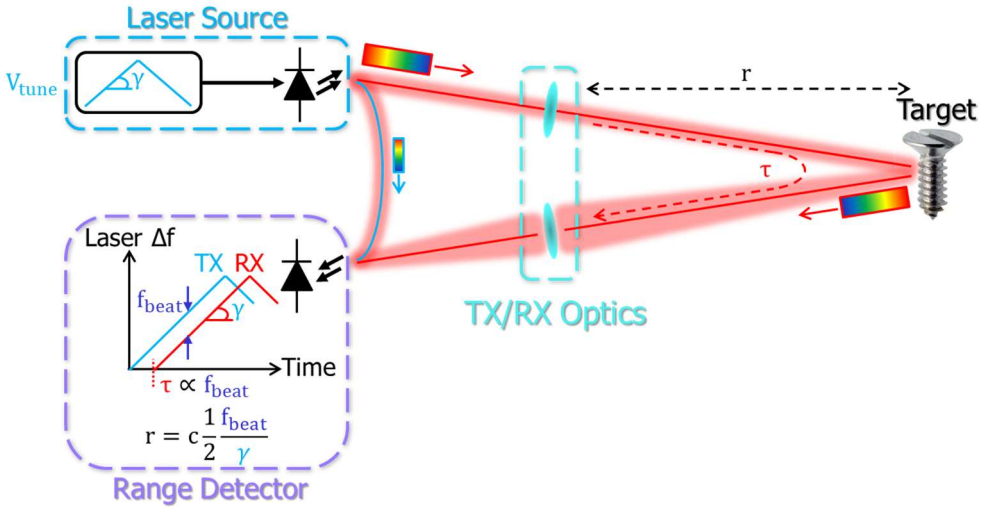

Fig. 1-3. Schematic for frequency-modulated continuous-wave lidar. A laser source transmits a frequency-modulated optical wave, which is reflected by a target surface. The beat frequency on the receiver photodiode encodes distance to the target.

The descriptions of chirped-AMCW lidar and chirped-FMCW lidar are very similar, but differ in several important ways. Firstly, the modality of the chirp is different in each case: an AM chirp modulates the intensity of a light source, while an FM chirp modulates the phase of the light source. Secondly, the mixing method is different in each case: delayed and non-delayed AM chirps are electronic signals manifested as current or voltage, so they must be mixed with an RF mixer, while FM chirps are electric field signals which superimpose on a photodiode. The photodiode detects power in electric fields, not amplitude, thus the photodiode is well-modeled as an ideal square-law detector, performing the mixing step on conversion of signals to the electronic domain. This allows for simple detection of signals with minimal electronic signal conditioning. Thirdly, the resolution in both cases is limited by the frequency excursion of the intensity modulation (AMCW) or frequency modulation (FMCW), but AMCW intensity modulation is limited by achievable electronic bandwidths, 10s of GHz for state-of-the-art electronics, while FMCW is limited by the tuning ranges of laser diodes, which can easily be in the range of 100s of GHz or even a few THz. This allows FMCW methods to achieve much higher transform-limited resolution, and thus FMCW is useful for metrological and precision manufacturing applications. Instantiations of FMCW and FMCW-like systems are described further in the next few sections.

1.2.4 Fiber-Optic Sensors and Optical Frequency Domain Reflectometry

The terminology for FMCW lidar used heavily in this dissertation is adapted primarily from the field of radar. However, other fields with applications other than free-space object imaging/detection have also embraced similar principles under different monikers. In this section, I highlight the use of coherent ranging in fiber-optic sensors in which very small environmental or structural changes are of interest. The methodology in this field is often referred to as "optical frequency-domain reflectometry" (OFDR), and many engineering challenges in this field are relevant to the development of FMCW imaging lidar. Traditionally, the problems being addressed in OFDR are referred to as "distributed sensing," "fault detection," and "link health assessment."

Distributed sensing of and fault detection in fibers can be achieved using time-resolved reflectometry ("optical time-domain reflectometry" or OTDR), which suffers from similar limitations to pulsed TOF lidar. For short optical links such as those used in avionics or rack-to-rack links in datacenters, using OTDR is challenging to use for localizing faults. For this reason, OFDR methods (using principles analogous to those described for FMCW herein) have been proven to exhibit high resolution fault-detection, proving useful for short distance measurement.

In addition, OT- and OFDR methods have been shown to be useful techniques for fiber-optic environmental sensors. For example, optical fibers embedded in large structures such as buildings or bridges are subject to thermal stresses, tensile/compressive stresses, and sometimes torsional stresses. Calibrating and probing these optical fibers with reflectometry methods allows for the detection of stresses with great precision, allowing efficient preventative maintenance to take place.

1.2.5 Swept-Source Optical Coherence Tomography (SS-OCT)

In a field of research closely related to FMCW lidar, known as Fourier-domain optical coherence tomography (FD-OCT), 3D reconstructions of biological tissues can be acquired with extremely high precision (10s of microns) [7–9]. This technology is commonly applied to ophthalmologic imaging for medical diagnostics [10]. Recent work in this field has extended the maximum range of a subset of FD-OCT systems, known as swept-source OCT (SS-OCT), beyond a typical working distance of 2 centimeters to a working distance of 1.5 meters [17,18].

Similar to FMCW lidar sensors, SS-OCT systems also suffer from issues stemming from non-linearity of tunable lasers, therefore many solutions proposed in SS-OCT literature focus on innovative and efficient post-processing architectures. So-called “k-clock resampling” systems track the optical frequency of a swept source accurately and resample raw target signals with uniformly-spaced samples in optical frequency [19]. Other implementations have demonstrated the use of non-linear discrete Fourier transforms (NDFTs) in the reconstruction of target signals exhibiting non-linearity [20]. SS-OCT systems have shown extremely high resolution, though only recent studies presented in [17,18] have shown extension of SS-OCT methods beyond working ranges of 2-cm. In addition, these systems use tunable lasers with exceptional optical frequency excursion (80nm in [17]; 100nm in [18]). Such tunable lasers with coherence lengths on the order of 10s to 100s of meters are very expensive, and prohibit the use of such 3D imaging systems for ubiquitous and/or cost-sensitive applications.

1.3 Integrated Photonics for Datacom and Sensors

Integrated photonics has emerged as a key technology in the fields of telecommunication, sensors, and quantum computing. Photonic carrier signals have several advantages over electronic carrier signals, and perhaps the most significant advantage is the low loss of light through optical waveguides. Resistance and capacitance of wires cause significant attenuation of electrical signals, increasing the amount of energy needed to transmit signals over significant distances. Even at the smallest scales, this attenuation is considered a limiting factor in the energy consumption of chips. Significant research and industrial effort has focused on the integration of optical transceivers and optical links from the long-haul applications (submarine telecommunication), all the way to the intrachip scale for links between regions on a single CPU. In this dissertation, we will give an overview of current and future photonic integrated circuit (PIC) technologies, some applications of PIC technology for sensor technology, and some specific applications of PICs for lidar.

1.3.1 Overview of Integrated Photonic Technologies

Most optical sensors can be modeled as optical links, where the goal is to characterize some property of the link itself. For example, in the case of a lidar measurement, we are interested in the physical length of the link. It is therefore useful to study PIC technologies by studying the backbone components of a single optical interconnect. Namely, we will give a broad overview of the following components and their integration progress: the light emitter (an LED or laser diode), the modulation scheme (direct or external), the waveguide, the fiber coupling scheme (usually a grating coupler), and the photo-receiver. In addition, we will give a short overview of typical platforms on which these components can be integrated, though we refer the reader to other references for a more exhaustive study of the numerous technology platforms.

Light emitting diodes (LEDs) and lasers operating in the near-infrared and infrared wavelengths are often implemented with III-V materials, and can have complex integration processes for integration on a silicon platform.

Direct modulation theory can be applied to laser diodes integrated on silicon or other substrates, but other research has also focused on the application of external intensity and phase modulators. Once light has been coupled onto a PIC, signals can be modulated onto the amplitude and/or phase of the carrier photons by thermal, mechanical, or electrical means. Intensity modulators can be cascaded in various configurations to create more complex structures, such as single-side-band (SSB) modulators (also known as I/Q modulators), which are useful in modulating a wavelength shift onto a single-wavelength optical carrier.

Optical waveguides have been developed in many processes, with the goal of creating effective routing structures between transmitter and receivers. The design of waveguides often calls for the use of silicon-on-insulator (SOI) technology, because it offers optical confinement in the vertical dimension. Waveguides fabricated in SOI processes are often limited by their propagation loss, usually due to roughness induced in the processing of the SOI wafer. In addition, waveguides in SOI processes must be designed to be single-mode, exhibit minimal dispersion, exhibit low bending loss, and exhibit minimal crossing loss (in the case of data center optical switches or on-chip routing). For applications requiring frequency discriminators for sensing, long delay lines may be required, pushing the limits of waveguides on a particular SOI process.

Optical signals are often coupled on to and off of PICs through some kind of fiber-coupling scheme. The challenge with optical coupling is transforming the optical mode supported by a fiber into a mode supported by the waveguides on chip. If there is significant mode mismatch somewhere in this link between fiber mode and waveguide mode, the coupler can have large insertion loss. In addition, couplers are usually designed to maximize an optical bandwidth over which there is minimal insertion loss.

Integrated photoreceivers on PICs vary by platform and optical wavelength. At the telecom wavelengths, around 1550nm, germanium is a promising direct-band-gap material with the potential of integrating with crystalline silicon.

1.3.2 Notable Integrated Photonic Lidar Sensors

Integrated photonics has enabled several new lidar technologies in the past half-decade. These include various instantiations of integrated lidar sources, beam steering devices, and integrated receivers. As is the case with integrated photonics in data communication applications, integrated photonics has the potential to make lidar systems smaller, more scalable, and less expensive.

Several beam-steering devices have been shown previously. In [21], the authors demonstrate a 1D optical phased array (OPA) steerable in one dimension by an array of 32 thermo-optic phase modulators, and in the second dimension by tuning the wavelength of a broadly tunable laser. In a similar demonstration, a 1D optical phased array with non-uniform emitter spacing is presented in [22], which optimizes beam steering side-lobe suppression. Successful demonstration of a fixed pattern 2D beam-steering OPA has been presented in [23]. The prospects of fully-integrated beam-steering devices such as those referenced here are very promising in the development of “solid-state” lidar, eliminating the need for sensors with mechanical parts and thus improving sensor reliability and lifetime. The promise of solid-state beam scanning has prompted several commercial ventures in beam-steering development, most notably the efforts announced by Quanergy ([24]) and Velodyne ([25]) in the past few years.

In addition to integrated beam steering devices, several receivers have been successfully demonstrated for both FMCW and optical coherence tomography applications. In FMCW applications, it may become desirable to create sensors that multiplex the receiver design, in such a way that “flash” lidar can be achieved for high-resolution imaging. This has been demonstrated by the “nanophotonic coherent imager,” [26], in which an array of grating couplers is used in conjunction with a micro-lens array to distribute received light to a camera-like array of coherent receivers. In addition, integrated in-phase/quadrature (I/Q) receivers have gained attention in extremely high resolution applications, due to their ability to resolve conjugate ambiguity in range measurements [27].

Integrated receiver arrays have become an important technology for pulsed TOF sensors. Avalanche photodiodes (APDs) have been identified as a receiver technology with very high sensitivity, but have historically been expensive to develop due to device yield issues. Several research and commercial ventures have addressed this issue and demonstrated that reliable APD arrays can be fabricated and used in long-range lidar applications [13,28].

1.4 Structure of the dissertation

This dissertation covers several topics in detail. In Chapter 2, I will outline working principles of FMCW lidar, along with practical considerations regarding component design and noise considerations. Also in Chapter 2, I will outline methodology for analyzing and numerically simulating laser phase noise. In Chapter 3, I will detail the analysis and design of optoelectronic phase locked loops (OPLLs) and their utility in FMCW lidar. This will include detailed summary of my work in packaging, testing, and using an OPLL at the chip-scale, and I will show 3D imaging results using this OPLL. In Chapter 4, I will detail the "K-clock" resampling method and variations in this signal processing method for improving the performance of non-linear FMCW lidar. This will include error analysis, numerical analysis using the phase noise simulation framework outlined in Chapter 2, and experimental results showing the usefulness of k-clock and "multi-k-clock" resampling methods. Finally, in Chapter 5, I will summarize the dissertation, and outline future visions and possible future directions for 3D imaging lidar. This includes some open questions regarding the analysis, methods, and experiments presented herein.

2 Practical FMCW Lidar Considerations

2.1 Principles and Fundamental Limits of Linear FMCW Lidar

Frequency-modulated continuous-wave lidar, as outlined in Section 1.2.3, is based on the modulation of laser wavelength, and uses principles of interferometry to probe the unknown length of an asymmetric interferometer. Fig. 2-1. shows several critical components of this interferometric probe, including the tunable laser, asymmetric interferometer, target characteristics, and receiver. As presented in this figure, the tunable laser exhibits a linear frequency sweep over an excursion denoted by Δf, in units of Hertz, at a sweep rate of γ, in units of Hertz per second (or Hz^2). The chirped laser is divided into two paths – a "target" arm (depicted as the upper arm), and a "local" arm (depicted as the lower arm). The splitting ratio of this optical coupler can be determined so as to optimize the lidar link budget, outlined in Section 2.2. The target is depicted with a one-way distance, r, in units of meters, an associated round-trip delay, τ, in units of seconds. In addition, a given target may have a velocity along the optical axis, denoted by v, in units of meters per second. The optical combiner couples light from the upper and lower arms of the interferometer, before impinging on a photoreceiver. In Fig. 2-1, the photo-receiver is depicted as a single-ended photodiode (PD) with a transimpedance amplifier (TIA). Interference signals are recorded and processed with data acquisition tools, denoted by the "Post-Processing" block.

In the following sections, I will outline the general properties of each of the primary components as depicted in Fig. 2-1.

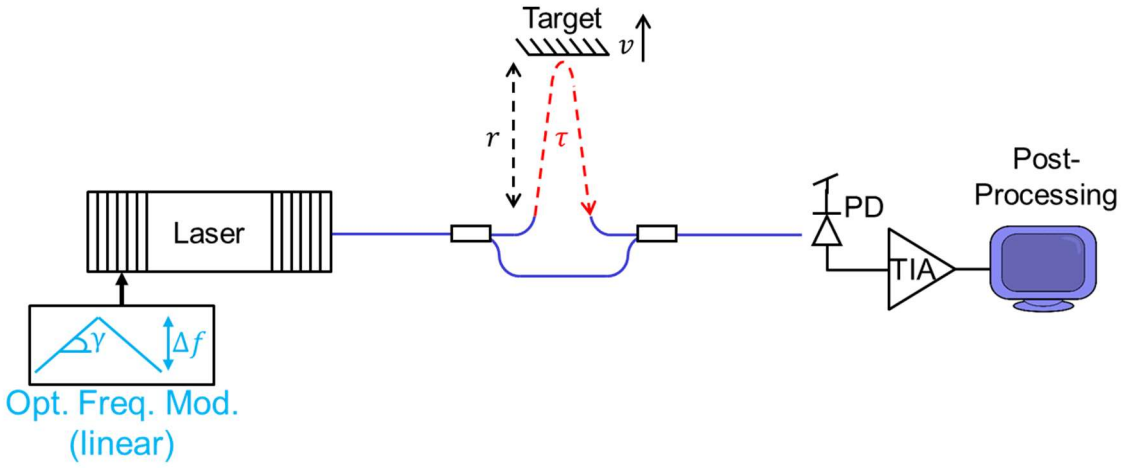

Fig. 2-1. FMCW Lidar as an interferometric probe. A laser with a continuum of optical frequencies can be launched into an interferometer in which one arm of the interferometer is some unknown distance to a reflecting object. Depending on the asymmetry between the arms of the interferometer, it will exhibit a wavelength-dependent response which can be measured with a photoreceiver and post-processed to infer target distance.

2.1.1 Tunable Lasers

Due to the interferometric nature of the FMCW measurement, it is necessary to use lasers whose wavelength can be modulated over some modest or broad wavelength range. Several solutions can be used to achieve this wavelength "tuning," and these solutions vary in terms of capability and cost.

Lasers emit light according to cavity characteristics and gain medium characteristics of the physical devices. By design, a laser cavity can support few or many optical modes with

different wavelengths. In this dissertation, we are concerned primarily with devices that lase at a single wavelength, and where that wavelength can be "tuned" over some modest wavelength range. Laser tuning is often achieved by some controllable modification to the laser cavity. This can take the form of a physical displacement of one or both of the cavity reflectors, or a modulation of the effective index of the cavity by heating/cooling or injection of electrical carriers. In addition, various gain-controllable and/or phase-shifting elements can be included to select a single cavity mode out of several or many possible cavity modes.

In this dissertation, we study three types of tunable lasers: MEMS-cavity tuned vertical cavity surface emitting lasers (MEMS-VCSELs), short-cavity distributed Bragg reflector semiconductor lasers (SC-DBR-SCLs), and thermally-tuned VCSELs (DBR VCSELs). These lasers vary in terms of their tuning response (continuous excursion, frequency-modulation response) and tuning noise (typically referred to as "linewidth" or "coherence length"). Table 2-1 gives representative values for these laser sources in terms of relevant characteristics for FMCW lidar.

Table 2-1. Some Laser Sources for FMCW Lidar

Laser Source	Nominal Frequency Excursion	Frequency Modulation Response (FM Response)	Nominal Linewidth	Reference
MEMS-VCSEL	**< 2.5THz (< 20nm)**	60KHz-1MHz	< 60MHz	[29], [30]
SC-DBR-SCL	**< 150GHz (< 1.2nm)**	**< 60MHz**	< 60MHz	[31]
DBR VCSEL (directly modulated)	**< 400GHz (<3.2nm)**	< 20KHz	**<10MHz**	[32,33]

2.1.2 Mach-Zehnder Interferometer and Balanced Photodetection

In general, an interferometer is characterized as having a single input and a single output, with two or more optical paths supported between the input and output. Many kinds of interferometers exist, but in this dissertation, we are concerned with a particular type of interferometer, known as a Mach-Zehnder Interferometer (MZI).

A common interferometric structure is known as the Michelson Interferometer, shown in Fig. 2-2a). A beam splitter and two mirrors create two optical round trip paths (L_1 and L_2), and are co-incident on the photodetector. A similar structure, though markedly more configurable, is known as the Mach-Zehnder Interferometer, and is shown in Fig. 2-2b). Two beam splitters are used to send light down two paths and recombine them at a pair of detectors. Various modifications to the paths between BS1 and M1, M1 and BS2, BS1 and M2, and M2 and BS2 can be made to change the optical delay through the two paths. Fig. 2-2b) shows one such modification, where a retroreflector is used to increase the length of one arm of the MZI over the length of the other arm.

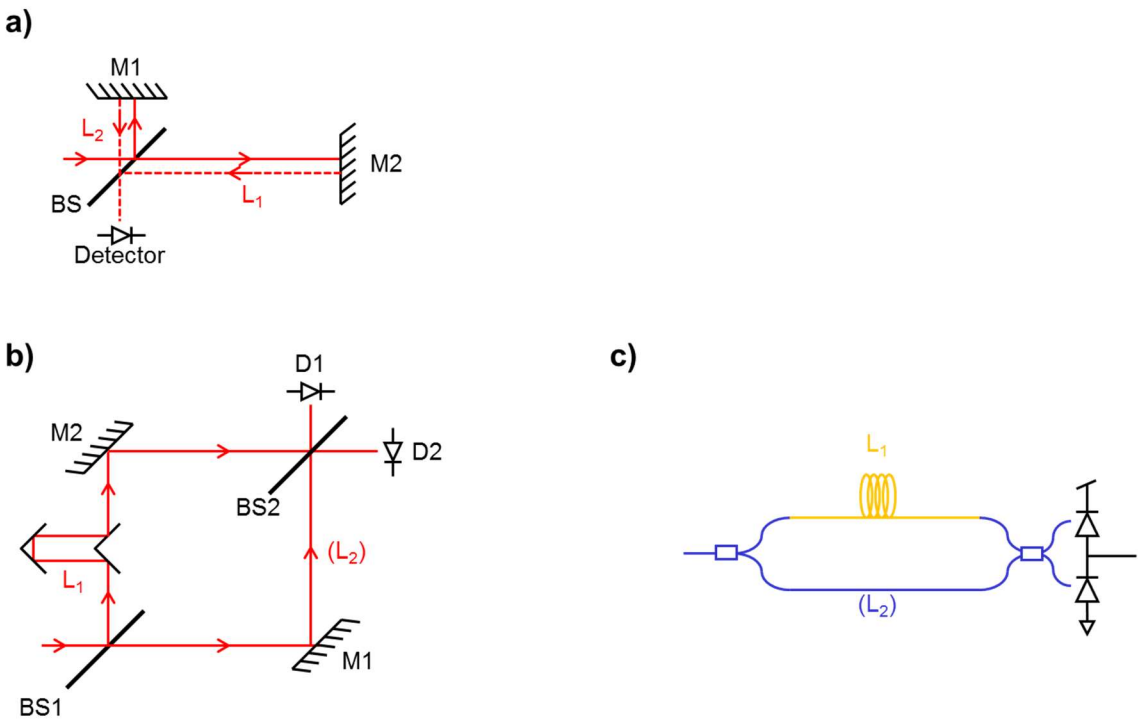

Fig. 2-2. Interferometric architectures. A) a standard Michelson interferometer, in which two path lengths are determined by reflectors M1 and M2 and their distances from an entrance beam splitter, BS. B) A flexible variation of the Michelson design known as a Mach-Zehnder Interferometer (MZI), in which two path lengths are determined by independently modified paths. C) a waveguide configuration of an MZI depicted using optical single-mode fibers of different lengths.

MZIs can also be implemented with waveguides, as shown schematically in Fig. 2-2c). Optical couplers can exhibit beam-splitter-like behavior, and optical path differences between two arms of the MZI can be induced by optical delay lines in various types of waveguides, such as optical fiber or ridge waveguides on photonic chips. Assuming similar path loss, and assuming the spectral response of components is similar, the interferometers in Fig. 2-2 should all exhibit identical interferometric behavior. In practice, path loss, non-uniform spectral response of components, and dispersion effects will cause deviations in the response of each interferometer.

With generic treatment of wavelength-dependent refractive index, we can derive the optical frequency response of an MZI. Consider the interferometer of Fig. 2-2c), with asymmetric path lengths of L_1 and L_2, and consider the waveguides to have identical effective indices of refraction. At a particular optical frequency, ν, the waveguides exhibit a refractive index of $n(\nu)$, and we can calculate the optical phase at the output of the asymmetric waveguide outputs:

$$\phi_1(\nu) = 2\pi\nu\frac{L_1 n(\nu)}{c_0};\ \phi_2(\nu) = 2\pi\nu\frac{L_2 n(\nu)}{c_0} \tag{2.1}$$

The condition for maximum interference occurs when the phases of each output are different by precisely an integer multiple of 2π, giving the condition,

$$\frac{\phi_2(\nu)-\phi_1(\nu)}{2\pi} = m = \frac{\nu n(\nu)}{c_0}(L_2 - L_1) \tag{2.2}$$

In order to calculate the free spectral range (FSR) of the MZI, which is defined as the distance between adjacent constructively interfering optical frequencies, we take the derivative of m with respect to optical frequency, ν:

$$\frac{dm}{d\nu} = \frac{(L_2 - L_1)}{c_0}\left[n(\nu) + \nu\frac{dn(\nu)}{d\nu}\right] \tag{2.3}$$

The FSR can be written:

$$FSR = \frac{c_0}{(L_2 - L_1)n_g} \tag{2.4}$$

Where we have used the common notation for group index, n_g, taking into account first order dispersion effects in the waveguide. This analysis shows an important consideration in designing interferometers using dispersive waveguides – one must use the group index when calculating the optical length of asymmetric arms.

Light with a given arbitrary time-varying phase can be coupled into both arms of the MZI through a directional coupler such as that depicted in Fig. 2-3. Light from each arm is delayed by some time, τ_1 for the upper arm and τ_2 for the lower arm. Given an input field described by $E_{in}(t) = E_0 \cdot \exp\big(j\phi(t)\big)$, where E_0 is a constant amplitude and $\phi(t)$ is some time-varying optical phase, the input to each arm of a directional coupler (used as a combiner) can be written:

$$E_{upper}(t) = E_{in}(t - \tau_1) = E_0 \cdot exp\big(j\phi(t - \tau_1)\big) \tag{2.5}$$

$$E_{lower}(t) = E_{in}(t - \tau_2) = E_0 \cdot exp\big(j\phi(t - \tau_2)\big) \tag{2.6}$$

The output of a 50/50 directional coupler is characterized by coefficients:

$$a(z) = cos(Kz)\, e^{i\beta z} \tag{2.7}$$

$$b(z) = i\, sin(Kz)\, e^{i\beta z} \tag{2.8}$$

Where z is chosen such that $|a(z)|^2 = |b(z)|^2 = 1/2$. These coefficients describe the output field after a directional coupler of length z, waveguide mode propagation constant β, and a waveguide coupling coefficient K, which itself is a function of the waveguide geometry. For reference, a simple directional coupler is depicted in Fig. 2-3.

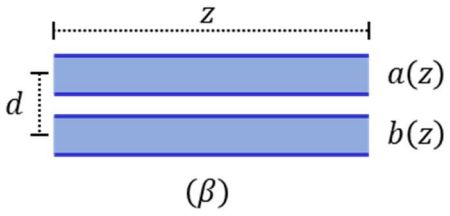

Fig. 2-3. Simple directional coupler. The directional coupler is a pair of waveguides in which modes from one waveguide can evanescently couple into the other waveguide. If light is injected into the first waveguide (waveguide A here), it will oscillate between the first and second waveguides. The output field of waveguide A will be the input field multiplied by the coefficient, $a(z)$, and the output field of waveguide B will be the input field multiplied by the coefficient $b(z)$. The magnitude and phase of the coefficients depends on mode propagation constants in the waveguides, the separation between the waveguides, and the length over which the coupling occurs.

The input to the first photodiode is thus:

$$E_{PD1}(t) = a(z)E_{upper}(t) + b(z)E_{lower}(t) \tag{2.9}$$

$$E_{PD}\ (t) = \frac{1}{\sqrt{2}}e^{i\beta z}E_0 \cdot \left[exp\big(j\phi(t - \tau_1)\big) + i\, exp\big(j\phi(t - \tau_2)\big)\right] \tag{2.10}$$

While the input to the second photodiode is given:

$$E_{PD2}(t) = a(z)E_{lower}(t) + b(z)E_{upper}(t) \tag{2.11}$$

$$E_{PD2}(t) = \frac{1}{\sqrt{2}} e^{i\beta z} E_0 \cdot \left[exp\left(j\phi(t-\tau_2)\right) + i\, exp\left(j\phi(t-\tau_1)\right)\right] \tag{2.12}$$

The photocurrent for each diode is proportional to the intensity of each field:

$$|E_{PD1}(t)|^2 = E_0^2 \cdot \left[1 + sin\left(\phi(t-\tau_1) - \phi(t-\tau_2)\right)\right] \tag{2.13}$$

$$|E_{PD2}(t)|^2 = E_0^2 \cdot \left[1 - sin\left(\phi(t-\tau_1) - \phi(t-\tau_2)\right)\right] \tag{2.14}$$

The output current of the photodiodes in balanced configuration will therefore be proportional to the difference in power between the two directional coupler outputs:

$$I_{out}(t) = 2K_{PD}E_0^2\, sin\left(\phi(t-\tau_1) - \phi(t-\tau_2)\right) \tag{2.15}$$

If the laser is frequency swept, the phase of the optical field takes the form:

$$\phi(t) = 2\pi\left[\frac{\gamma t^2}{2} + f_0 t\right] + \phi_0 \tag{2.16}$$

Where γ is the chirp rate of the laser (Hz/s), f_0 is the initial optical frequency of the chirp (Hz), and ϕ_0 is a phase offset. This means that the output photocurrent takes the form:

$$I_{out}(t) = 2K_{PD}E_0^2\, sin\left(2\pi\left[\gamma(\tau_2-\tau_1)t + \frac{\gamma}{2}(\tau_1^2 - \tau_2^2) + f_0(\tau_2-\tau_1)\right]\right) \tag{2.17}$$

The time-varying portion of the photocurrent phase is a linear function of the difference, $(\tau_2 - \tau_1)$, indicating that the frequency of the sinusoid is constant, and takes on the value:

$$\omega_{beat} = 2\pi \cdot \gamma(\tau_2 - \tau_1) \tag{2.18}$$

2.1.3 Range and Velocity Measurement

If a target interferometer is constructed as shown in Fig. 2-1, it will exhibit a sinusoidal intensity response with $FSR = \frac{c_0}{L_2 n_g - 2rn_0}$, where we have used n_g as the group index of the local fiber, and n_0 as the index of air. In order to measure range, we can use the tunable laser to sweep through several or many FSR's of the interferometer. The fractional number of interference fringes observed over a fixed frequency sweep indicates the delay difference between the arms of the interferometer, and therefore the arm length of the target arm. If the tunable laser sweep is fixed in terms of optical wavelength excursion (say, with frequency excursion Δf_{laser}) and is linear over a fixed time (say, a time T), the intensity output of the interferometer will oscillate as it sweeps through fringes, and the frequency of this oscillation, or "beat frequency" f_{beat} will be a direct indicator of the FSR and therefore the range of the target. An expression for f_{beat} is given as $f_{beat} = \frac{\Delta f_{laser}}{T}\frac{1}{FSR} = \gamma\tau$, where we have written the simplification as a sweep rate, γ [Hz/s] ($\gamma = \frac{\Delta f_{laser}}{T}$) multiplied by a characteristic MZI delay, τ [s] ($\tau = \frac{1}{FSR}$).

This means that we can perform an efficient and fast Fourier transform on the output signal and generate a spectrum where the x-axis directly corresponds to the optical path length difference of the MZI. This represents a very computationally efficient method to measure range with somewhat arbitrary precision. The precision can be analyzed by examining the bin width in the Fourier domain for the analysis of f_{beat}:

$$\delta f = \frac{1}{T} = \frac{\gamma}{\Delta f_{laser}} \tag{2.19}$$

Since the delay, τ, is proportional to beat frequency, we can write delay resolution as

$$\delta\tau = \frac{\delta f}{\gamma} = \frac{1}{\Delta f_{laser}} \tag{2.20}$$

This represents what is commonly referred to as the "Fourier resolution" of an FMCW scheme. Two targets that exhibit delays with differences smaller than $\delta\tau$ cannot be distinguished, even after sinc-interpolation (by zero-padding in the time domain). This is a fundamental advantage of FMCW lidar over other lidar schemes – resolution of FMCW systems can be improved simply by increasing the frequency excursion of the tunable source. The Fourier resolution is distinctly not limited by the measurement electronics, making it an attractive method for achieving extremely high precision without expensive electronics in the receiver.

It is convenient to interpret the beat frequency in this scenario using the schematic in Fig. 2-4. The transmitted signal and reflected signal each exhibit a linear optical chirp, and the difference in optical frequencies at the combiner is exactly the beat frequency observed at the intensity output of the interferometer. In the green-shaded area of the figure, the beat frequency will be related to the delay, τ, by constant of proportionality γ. Range can be calculated by multiplying the beat frequency measured during the single ramp by the constant, $c/(2\gamma)$.

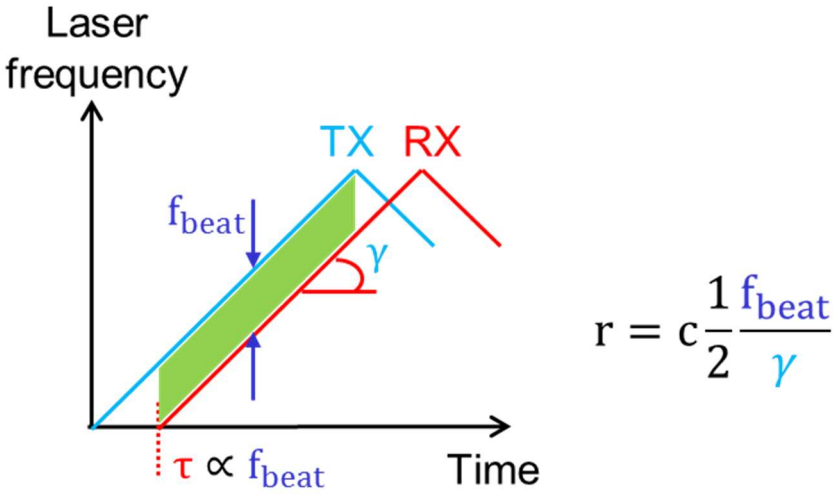

Fig. 2-4. MZI beat frequency intuition with a swept-source laser. The transmitted signal has an optical frequency chirp (depicted here as linear, though it may be non-linear in some cases). The received signal is delayed by the longer arm of an interferometer, and the two signals are mixed together with an optical combiner and a photodiode, and the difference in optical frequency between the transmitted and received chirps represents the oscillation frequency of the intensity of the interferometer. In the linear case, the beat frequency is proportional to the delay of the received signal with constant of proportionality equal to the slope, γ, of the chirp.

By examining the schematic in Fig. 2-4, we can intuit the effect of Doppler shifts in FMCW lidar measurements. The typical Doppler shift in radar is given by the equation,

$$f = \left(\frac{c}{c+v_s}\right) f_0 \tag{2.21}$$

Where f_0 is the frequency of the original carrier wave, c is the speed of light in air, and v_s is the velocity of the source on axis with the receiver (positive v_s corresponding to an object moving away from the receiver). This represents a shift of the received optical chirp by some amount higher (for an object moving towards the receiver) or lower (for an object moving away from the receiver). This shift causes a shift in the observed beat frequency, as shown in Fig. 2-5, where the red "RX" curve is shifted up by some amount dependent on the target velocity. In general, the beat frequency shift due to target delay and target velocity cannot be resolved independently.

However, by making two measurements, range and velocity can be somewhat decoupled. In Fig. 2-5, the beat frequency measured during the "up-ramp" (shaded green), and the beat frequency measured during the "down-ramp" (shaded yellow) are clearly modulated differently. In the case of zero doppler shift, these frequencies would be identical, though with the doppler shift, the up-ramp beat is modulated down in frequency while the down-ramp beat is modulated up in frequency. Assuming that the range during the measurement is changing slowly enough, the two effects can be decoupled with some uncertainty resolution.

Other methods also exist for decoupling range and velocity in an FMCW measurement, though we refer the reader to other sources since they are not a main focus in this dissertation. We note here that the simple method described here and other methods described in previous studies for decoupling range and velocity are seen as an important advantage of FMCW lidar over other forms of lidar, such as pulsed time-of-flight lidar. Velocity measurement is an important feature for segmentation of measurements in a point cloud – i.e., the ability to distinguish points that belong to a moving object versus points that belong to a stationary object. Velocity signatures also allow object recognition algorithms to efficiently parse and classify objects.

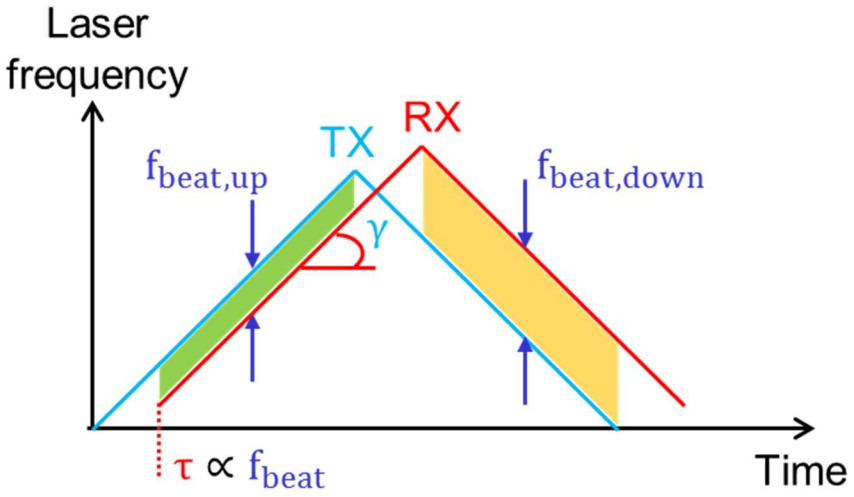

Fig. 2-5. Doppler shift processing with FMCW lidar. The received optical frequency chirp will be doppler shifted up or down by an amount related to the velocity of the reflecting target. In general, there is always ambiguity in range/velocity measurement, due to the fact that both range and velocity modulate the received signal similarly, i.e. by modulating the measured beat frequency. However, assuming the target is moving slowly relative to the ramp period of the laser tuning, the range and velocity can be decoupled by making two measurements: one beat measurement with an "up-ramp", and another with a "down-ramp". The difference in beat frequencies represents the frequency shift due to velocity, while the average represents the range.

2.2 CW Lidar Link Budget

We can consider the lidar optical path to be comprised of a signal link from laser transmission to receiver via free-space coupling and target reflection. We can define a link budget for this system by placing constraints on maximum output power, assuming efficiencies for fiber-to-free-space and free-space-to-fiber coupling, considering beam divergence as a function of target distance, and target reflection efficiency. Each of these considerations will be outlined in the next few sub-sections. Fig. 2-6 shows a graphical outline of some link budget considerations. We will consider maximum output in terms of eye-safety standards; free-space coupling efficiency will be analyzed using typical lens design characteristics; divergence will be modeled by adapting the phenomenological "radar range equation" for use at optical

wavelengths; target loss will be calculated based on standard Lambertian reflection assumptions. We will define detector shot noise and thermal noise floors for direct and coherent detection to define a detector-limited signal-to-noise ratio (SNR). Laser phase noise can also affect this link budget, and will be considered in section 2.2.5.2.

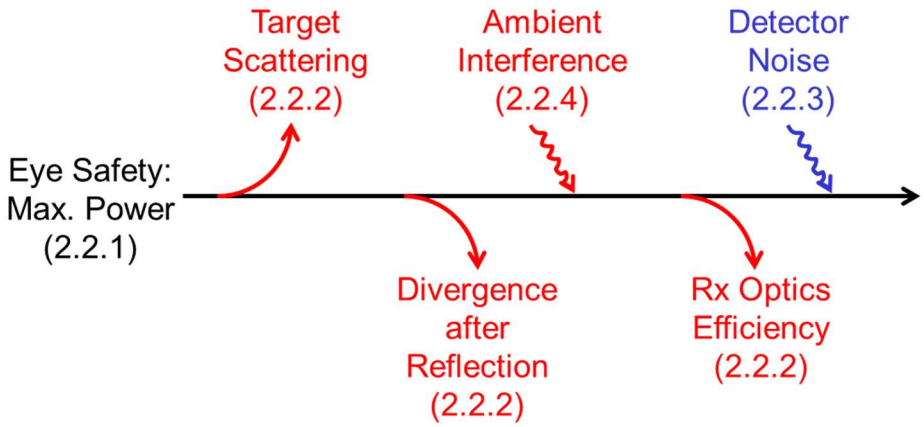

Fig. 2-6. Link budget considerations: This figure outlines several of the losses and noise considered in this section, and the sections in which they are covered.

2.2.1 Eye-Safety Considerations

Laser light has immense potential to damage the human visual system. Not considering the effects of pulsed lasers, which have very high instantaneous powers, CW laser light exhibits different pathological effects at different wavelengths. In lidar, wavelengths considered are usually in the classically-defined ranges of visible, infrared, and near infrared, covering a wavelength range from 400nm to 3000nm. In this spectrum, safety thresholds are defined based on retinal and corneal burn. These thresholds are specified as a "maximum permissible exposure" (MPE), and is measured in terms of energy or power density of a light source.

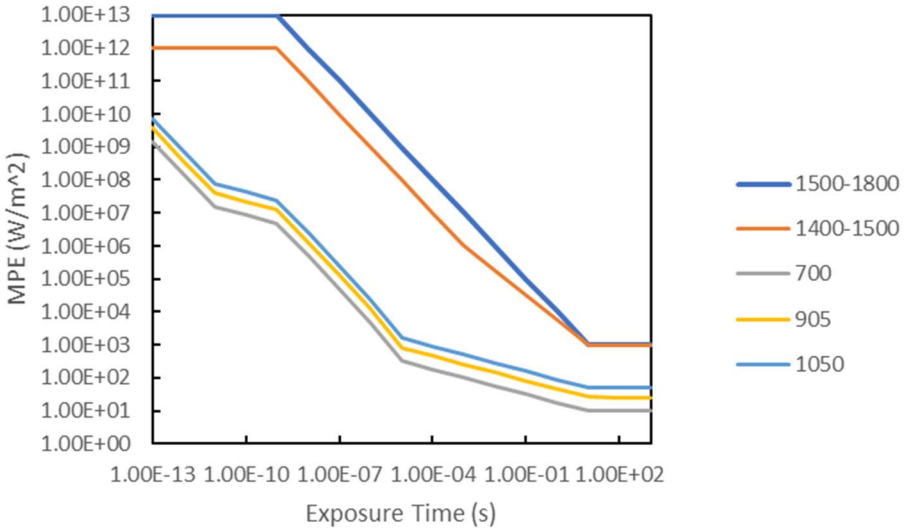

Fig. 2-7. Ocular maximum permissible exposure vs. exposure time for several lidar wavelengths; based on standard tables found at [https://workspace.imperial.ac.uk/physics/Public/physicsdocs/about/safety/files/MPE-tables.pdf].

For an operating wavelength of 1550nm, operating in CW condition, and using a 5-millimeter diameter aperture, the maximum output power can be calculated:

$$P_{max}(1550nm, CW, 5mm) = MPE(1550nm, 100s) \times \pi\left(\frac{5mm}{2}\right)^2 = 19.6mW\ (12.9dBm) \tag{2.22}$$

This aperture for continuous-wave 1550nm with 5mm aperture is a reasonable application specification – ubiquitous lidar applications will be deployed in close proximity to drivers and pedestrians who can potentially stare directly into the aperture of the lidar system.

At 905nm, another common lidar wavelength, we can calculate the maximum power:

$$P_{max}(905nm, CW, 5mm) = MPE(905nm, 100s) \times \pi\left(\frac{5mm}{2}\right)^2 = 0.5mW\ (-3dBm) \tag{2.23}$$

This makes 1550nm a desirable operating wavelength, due to eye-safety considerations. However, there may be other link budget considerations that will influence wavelength selection. For example, SNR of a lidar link budget can be increased significantly through the use of avalanche photodiodes (APDs), which are more easily manufactured for wavelengths with lower MPE. It is important to consider a plethora of details beyond eye-safety when analyzing the link budget of the lidar system being designed. Here, we will consider CW lidar systems (or quasi-CW, or "shuttered" CW), so we will use 10mW at 1550nm as a rule of thumb in further calculations. We note that eye-safe maximum power should be re-calculated for different exposure times and different wavelengths, with corresponding detector characteristics.

2.2.2 One-Way Lidar Equation based on the Radar Equation

Once coupled into free-space, the electromagnetic wave experiences divergence and scattering from transmitter to target and back to receiver. We can examine loss due to divergence and scattering by considering the phenomenological equations used in radar design. These are known as "radar equations," and capture most first order divergence and scattering effects of standard radar targets. They are derived from basic geometric principles and some reasonable assumptions about the target reflection, namely, that the transmitted light is either focused or radially radiated, and that the target reflection is radially scattered with some Lambertian assumptions.

In this dissertation, we will consider the "one-way radar equation" to develop a simple "one-way lidar equation," as opposed to the sometimes referred to "two-way" equation. "Two-way" refers to the assumption that light is radially scattered between the transmitter and target, in addition to the radially scattered light between the target and receiver. "One-way" refers to the assumption that light is only radially scattered between the target and receiver. We will consider cases in which we can focus our transmitted beam close to some diffraction limit for an assumed target distance. In this section, this means we will only consider scattering effects of the target, and we will neglect divergence of the transmitted beam and absorption along the entire two-way path.

The "one-way" radar equation is given below:

$$P_{rx} = P_{tx} \cdot e^{-2\alpha z} \cdot \gamma \cdot \frac{\pi\left(\frac{D}{2}\right)^2}{\left(\frac{4\pi z^2}{2}\right)} \cdot cos(\varphi) \cdot \eta \tag{2.24}$$

Each multiplicative term in this equation is a phenomenological description of a physical process in the free-space link: absorption is modeled a coefficient, α, over a target distance z; reflectivity is modeled as a multiplicative loss. γ; the target is assumed to radiate spherically such that the surface area of the reflected radiation at the receiver distance is the surface area of a hemisphere with radius z; the area of the receiver aperture is modeled as a circular aperture with diameter D; the specularity of the target is modeled by the Lambertian term, $\cos(\varphi)$; and losses at the receiver in the conversion from free-space coupling to system waveguides are modeled as a

receiver efficiency, η. As an important note, the primary modification of this equation to create the "two-way" radar equation is the inclusion of a divergence between transmitter and target, modeled as an additional spherical radiation from the transmitter. This makes the received power inversely proportional to $1/z^4$ in the "two-way" case, as opposed to inversely proportional to $1/z^2$ as shown in eq. (2.24).

2.2.3 Detector Noise and Signal to Noise Ratio in FMCW Lidar

In analyzing the differences between pulsed TOF lidar and coherent FMCW lidar, we can examine each scheme's detector-limited SNR. The signal powers for direct (incoherent, intensity) measurements, as is the case for pulsed TOF, and coherent FMCW measurements, are given by:

$$S_{direct}^2 = K_{PD}^2 P_{rx}^2 \tag{2.25}$$

$$S_{coherent}^2 = K_{PD}^2 P_{rx} P_{LO} \tag{2.26}$$

The primary difference in these two measurements is the presence of the local oscillator power, P_{LO} in coherent detection.

We will consider two sources of detector noise, thermal (or "Johnson") noise, and current shot noise. Thermal noise describes effects of random material-dependent fluctuations on the signal in the receiver, while shot noise describes the effects of the discrete nature of electrons on the signal in the receiver. Noise spectral density is described for each effect by the equations below:

$$\sigma_{Thermal}^2 = \frac{4kT}{R} \tag{2.27}$$

$$\sigma_{shot}^2 = 2q(K_{PD} P_{DC}) \tag{2.28}$$

Where k is the Boltzmann constant, T is the effective temperature of the thermal noise source, R is the effective resistance for the thermal noise source, q is the fundamental unit of charge, K_{PD} is the receiver responsivity in A/W, and P_{DC} is the DC component of the incident light on the photo-receiver. The quantities of eqs. (2.27) and (2.28) have units of A^2/Hz, so they represent constant power spectral density noise levels. The DC optical power for an FMCW measurement is usually dominated by the local oscillator component, so the DC photocurrent can be written approximately as $I_{DC} = K_{PD} P_{LO}$

We can write the SNR for direct and coherent detection by writing S^2/σ_{total}^2 for each architecture:

$$SNR_{direct} = \frac{K_{PD}^2 P_{rx}^2}{\frac{4kT}{R} + 2q(K_{PD} P_{DC})} \tag{2.29}$$

$$SNR_{coherent} = \frac{K_{PD}^2 P_{rx} P_{LO}}{\frac{4kT}{R} + 2q(K_{PD} P_{LO})} \tag{2.30}$$

These expressions for coherent detection SNR yields an important design consideration for FMCW systems: namely, that the signal power (numerator) can be increased by increasing P_{LO}, until the shot noise component dominates the thermal noise of the detector. After this point, the SNR does not improve with increasing P_{LO}. This represents an advantage of FMCW measurements – coherent detection allows such systems to be fundamentally limited by shot noise, and not the thermal noise of the detector.

2.2.4 Solar Background Considerations

In addition to detector noise, ambient clutter can interfere with lidar measurements. Background noise, usually due to solar radiation that penetrates the earth's atmosphere, can enter lidar receivers and cause some amount of interference. In this section, we perform a simple analysis to show the dependence of coherent detection on solar background radiation.

A typical solar radiation spectrum is reproduced in Fig. 2-8. This spectrum follows a typical black-body curve, and also shows several atmospheric absorption lines due to ozone, oxygen gas, water, and carbon dioxide. In our analysis, we will focus mainly on the radiation spectrum in the immediate vicinity of 1550nm, and assume it is constant over a wavelength range of a few nanometers.

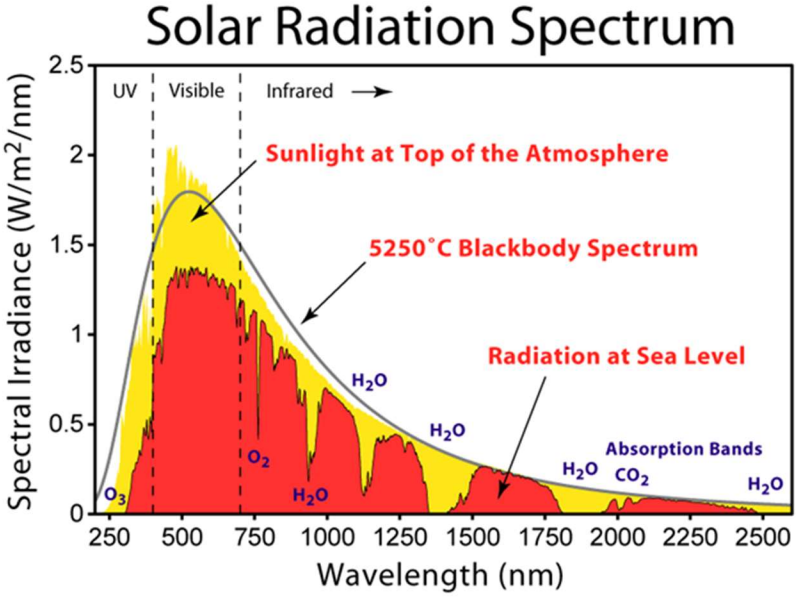

Fig. 2-8. Solar radiation spectrum, following a typical black-body spectrum with several atmospheric absorption lines. Reproduced from http://www.globalwarmingart.com/wiki/File:Solar_Spectrum_png.

As can be seen from Fig. 2-8, the solar spectral irradiance (SSI) around 1550nm is approximately $SSI(\lambda = 1550nm) \approx 0.1\frac{W}{m^2 \cdot nm}$. Assuming a constant SSI in the neighborhood of 1550nm, we can calculate a solar spectral density in units of W/Hz:

$$S_{Solar} = SSI \cdot Area \cdot \frac{1nm}{120GHz} \tag{2.31}$$

Assuming an aperture of 1 inch, this gives a solar spectral density around 1550nm to be $S_{Solar} = 4.2 \times 10^{-1}\ \ W/Hz$.

Solar spectral irradiance will cause several new sources of noise in a coherent detector. Firstly, the solar background can potentially have enough power to increase the magnitude of shot noise over that caused by the local oscillator. Secondly, the solar background, due to its spectral spread, will mix with itself generating a new noise source. Thirdly, the solar background will mix with the local oscillator, generating yet another noise source. Each of these effects has a different dependence on the SSI during the measurement. Due to the relatively low intensity of SSI relative to the local oscillator, we will neglect the effects of solar-induced shot noise in coherent detection SNR. For analytical derivations of the noise sources, we refer readers to [34].

Solar self-mixing spectral density can be written:

$$\sigma^2_{solar-sola} = 4K^2_{PD}(S^2_{solar}\Delta\nu)\ [A^2/Hz] \tag{2.32}$$

Where $\Delta\nu$ is the optical bandwidth of the solar spectrum entering the receiver. The optical bandwidth may be a feature of the irradiance during the measurement, or the bandwidth of an optical filter placed on the receiver.

Solar-local oscillator mixing spectral density can be written:

$$\sigma^2_{solar-LO} = 4K^2_{PD}(P_{LO}S_{solar})\ [A^2/Hz] \tag{2.33}$$

The spectral density of solar-LO mixing is independent of the optical bandwidth of the SSI or optical filter. In coherent detection, we will assume that thermal noise is negligible by design, so that we can write the SNR with solar background as:

$$SNR_{coherent} = \frac{K^2_{PD}P_{rx}P_{LO}}{2q[K_{PD}\cdot P_{LO}]+4K^2_{PD}[P_{LO}S_{solar}]+4K^2_{PD}[S^2_{solar}\Delta\nu]} \tag{2.34}$$

This SNR shows three possible regimes for solar-limited coherent detection: LO-shot noise dominated, solar-LO mixing dominated, or solar-solar mixing dominated. We can immediately delineate these solar-limited regimes. LO-shot noise dominates when $S_{solar} < \frac{q}{2K_{PD}}$. Solar-LO mixing dominates when $\frac{q}{2K_{PD}} < S_{solar} < \frac{P_{LO}}{\Delta\nu}$. Solar-solar mixing dominates when $\frac{P_{LO}}{\Delta\nu} < S_{solar}$.

Shot noise limited SNR can still be written as $SNR_{shot} = \frac{K_{PD}P_{rx}}{2q}$; solar-LO limited SNR can be written as $SNR_{solar-LO} = \frac{P_{rx}}{4S_{solar}}$; solar-solar limited SNR can be written as $SNR_{solar-solar} = \frac{P_{rx}P_{LO}}{4[S^2_{solar}\Delta\nu]}$. These expressions indicate that solar-limited SNR is not fundamentally limited by solar-solar mixing, but could be limited by solar-LO or LO-shot noises. The dominant effect depends on the solar spectral irradiance during the measurement. Using a set of assumptions given in Table 2-2, we can derive a curve for minimum received power in the presence of sunlight.

Table 2-2. Assumed properties for solar-limited detection analysis.

Property	Variable	Assumed Value
Local Oscillator Power	P_{LO}	10mW
Receiver Electronic Bandwidth	Δf	100kHz
Transmitted Optical Power	P_{tx}	10mW
Target Reflectivity	γ	0.1
Lambertian Factor	$\cos(\varphi)$	0.5
Circular Receiver Aperture Diameter	D	10cm
SNR Threshold	SNR_{min}	0dB

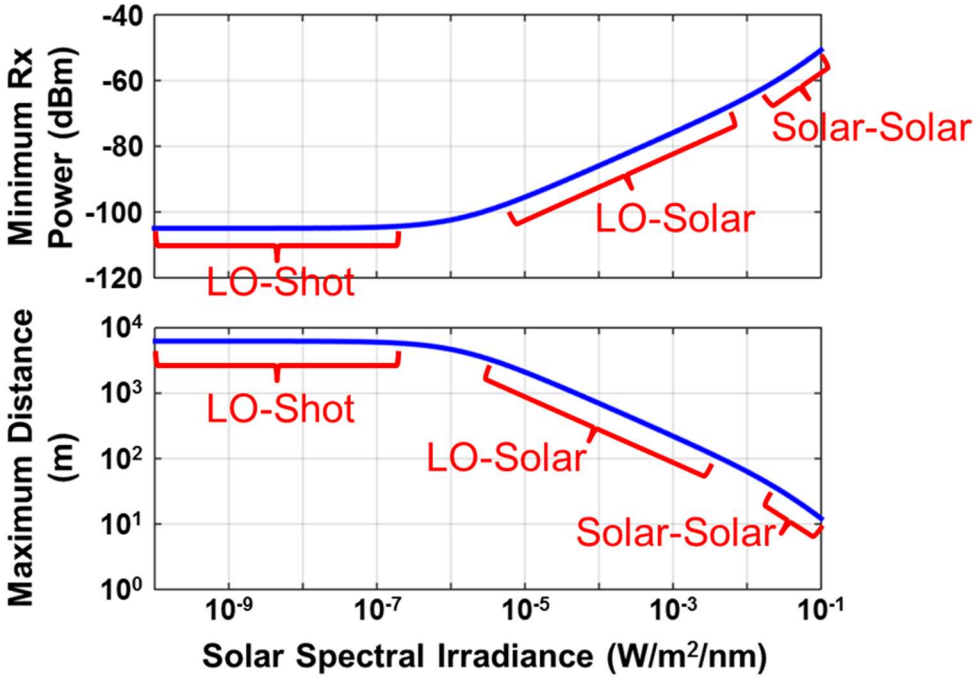

Fig. 2-9. Solar-limited coherent detection limits. Using values in *Table 2-2*, minimum power is calculated using the one-way lidar equation and the mentioned solar noise limits.

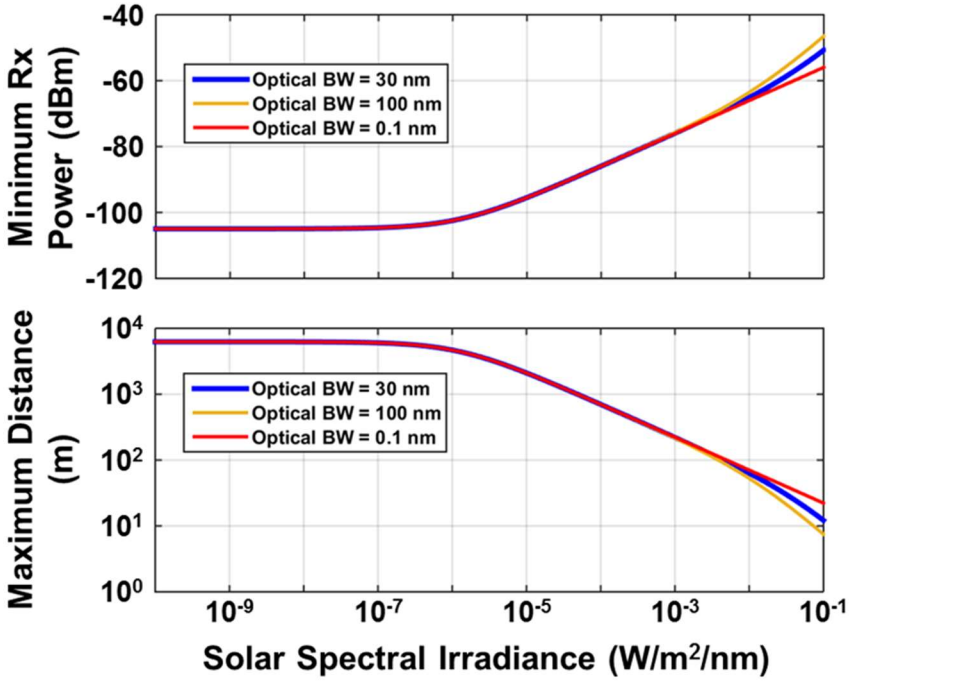

Fig. 2-10. Solar-limited coherent detection limits for different optical bandwidths. As can be seen from this graphic, changing the optical filter bandwidth for the receiver only shows appreciable SNR improvement at high solar spectral irradiance.

2.2.5 Laser Phase Noise in FMCW Lidar

We will first summarize previous analytical studies of laser phase noise and detector noise in FMCW lidar systems, then show numerical simulation and experimental verification of these analytical studies.

Phase noise is often described by "laser linewidth," the optical spectral width of a single-wavelength source. This description assumes that the noise on the frequency of the laser has a uniform power spectral density. For analytical purposes in this dissertation, we will use this assumption about laser frequency noise, but we note that it is important to verify this assumption before applying this analysis to other systems. In this section, we outline key results from phase noise analysis, but refer readers to [35] for a detailed derivation of these results from statistical principles.

Laser spontaneous emission often dominates the fluctuations in laser frequency. A spontaneously emitted photon has a frequency (energy) identical to that of the stimulated photons, but exhibits a random phase. The spontaneously emitted photon perturbs the net electric field of the laser output in magnitude and phase. In this analysis, we will neglect the magnitude fluctuation due to spontaneous emission. The electric field of the laser output can be written as

$$E(t) = cos\big(\phi(t) + \phi_n(t)\big) \tag{2.35}$$

where $\phi(t)$ represents deterministic laser phase, which can be a single-frequency or frequency-swept waveform, and $\phi_n(t)$ represents the noise process on laser phase. Spontaneous emission can be modeled as a zero-mean stationary random process. It can be shown that the first time-derivative of the noise process, $\dot{\phi_n}(t) = \frac{d\phi_n(t)}{dt}$, can be assumed to have a white power spectral density, such that

$$S_{\dot{\phi_n}}(\omega) \equiv \Delta\omega \tag{2.36}$$

A detailed analysis given in [35] shows that the power spectral density (shifted to baseband) of the electric field given in eq. (2.35) will be defined as

$$S_E^o(\omega) = \frac{\Delta\omega}{(\Delta\omega/2)^2+\omega^2} \tag{2.37}$$

when laser is operated as a single-frequency source. This Lorentzian lineshape is defined by its full-width half-max (FWHM), which is exactly equal to the parameter, $\Delta\omega$. This parameter is appropriately referred to as linewidth, and completely specifies the laser spontaneous emission phase noise process given the white-noise assumption of eq. (2.36), see Fig. 2-11. This assumption is not always appropriate, but serves as a good first-order approach to designing linear and non-linear FMCW systems, as we will show in the next sections. We refer readers to [36] for analysis and discussion of non-Gaussian noise in laser linewidth analysis.

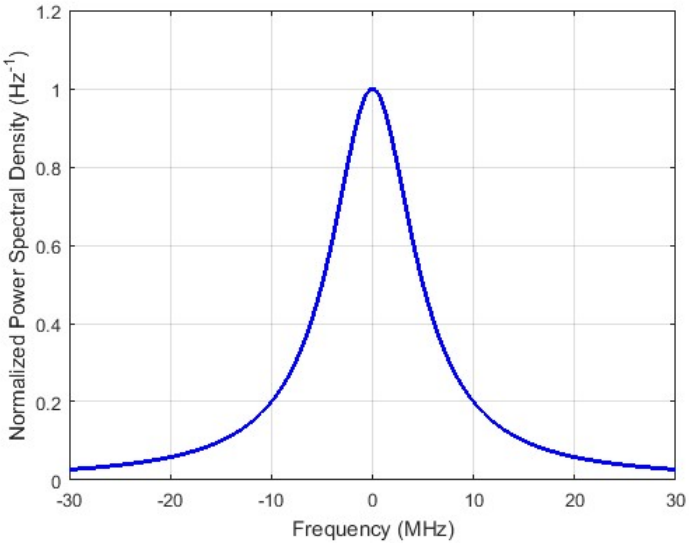

Fig. 2-11. Lorentzian lineshape for laser with 10 MHz linewidth.

Further analysis shows the effect of laser phase noise on the spectrum of an interferometric beat signal. We can write the electric field at the output of an asymmetric interferometer as the sum of the original field and a delayed copy of that field:

$$E_{total}(t) = cos\big(\phi(t) + \phi_n(t)\big) + cos\big(\phi(t-\tau) + \phi_n(t-\tau)\big) \tag{2.38}$$

It can be shown that the optical power is given by:

$$P(t) = cos[\phi(t) - \phi(t-\tau) + \phi_n(t) - \phi_n(t-\tau)] + DC\ terms \tag{2.39}$$

Where we note that the random processes $\phi_n(t)$ and $\phi_n(t-\tau)$ are identical except for the time-shift of τ (they are not independent processes). We will write this noise difference term as $\Delta\phi_n(t,\tau)$. The current induced on a photodiode due to this signal will be proportional to the optical power. This photocurrent, expressed as

$$i(t) \propto cos[\phi(t) - \phi(t-\tau) + \Delta\phi_n(t,\tau)] \tag{2.40}$$

When the laser frequency is linearly swept, such that the deterministic phase term is given by

$$\phi(t) - \phi(t-\tau) = \gamma\tau t + \omega_0\tau - \frac{\gamma\tau^2}{2} \tag{2.41}$$

analysis can show that the photocurrent power spectral density at baseband can be written:

$$S_i^o(\omega,\tau,T) = Tsinc^2\left(\frac{T\omega}{2}\right)e^{-\frac{2\tau}{\tau_c}} + \frac{\tau_c}{1+\left(\frac{\omega\tau_c}{2}\right)^2}\left\{1 - e^{-\frac{2\tau}{\tau_c}}\left[cos(\omega\tau) + \frac{2}{\omega\tau_c}sin(\omega\tau)\right]\right\} \tag{2.42}$$

where T is the window over which the spectrum is analyzed, and τ_c is defined as "coherence time," is given by $\tau_c = 2/\Delta\omega$. The figure below shows a plot of this spectrum for $\tau/\tau_c = 1$ and $T = 125\mu s$.

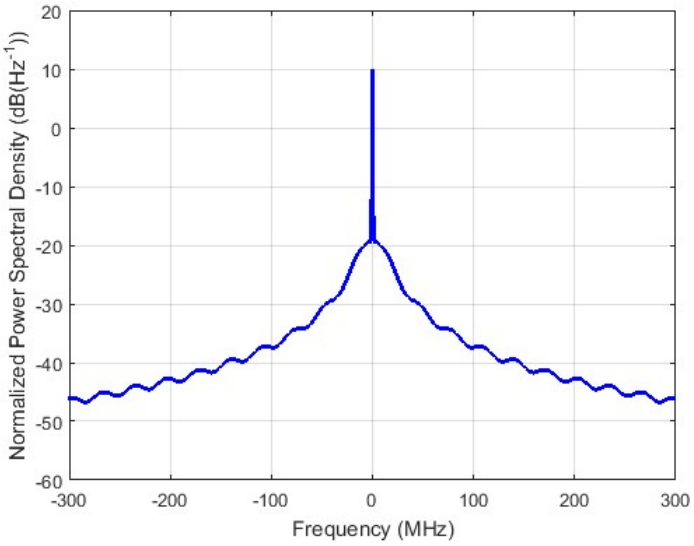

Fig. 2-12. Photocurrent spectrum for $\tau/\tau_c = 1$ and $T = 125\mu s$.

The result in Eq. (2.42) allows the calculation of SNR over target distance for a laser with linewidth equal to $\Delta\omega$. We can use this result to verify numerical simulations of FMCW signals with phase noise.

2.2.5.1. Numerical Verification Through Monte Carlo Method

We can numerically verify the analysis in Section 2.2.5 via Monte Carlo simulations. We can numerically converge to the analytical result of laser electric field spectrum shown in Fig. 2-11 by modeling the underlying statistics of laser frequency noise. The results shown in Fig. 2-13 show the average spectra of 100 time-domain simulations of laser frequency noise, showing that this simulation method is valid. The simulated linewidth was 10 MHz.

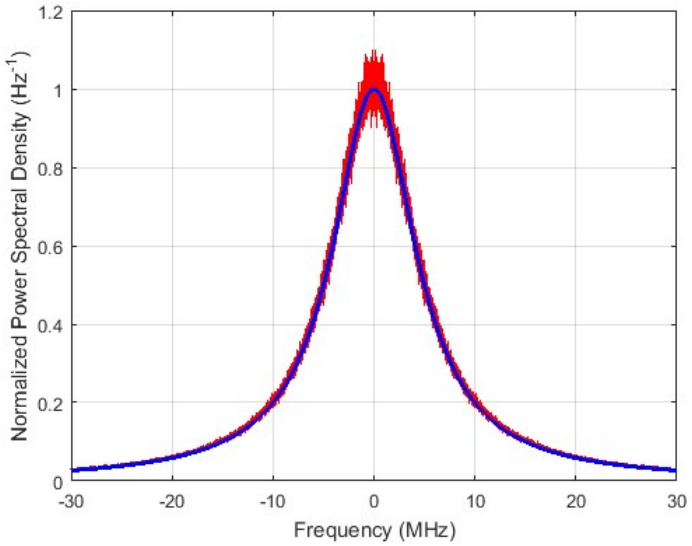

Fig. 2-13. Numerical verification of Lorentzian lineshape with Monte Carlo simulation(N = 100; $\Delta\omega = 2\pi$[10MHz])

We can extend the simulation to implement an asymmetric interferometer, effectively simulating a reference or target length. If we use the Monte Carlo numerical method, we can perform 100 time-domain simulations of interferometer beats, and we can verify beat spectral

analysis shown in Fig. 2-12. Fig. 2-14 shows the spectra resulting from interference beat modeling using the Monte Carlo method, showing agreement with the analytical results.

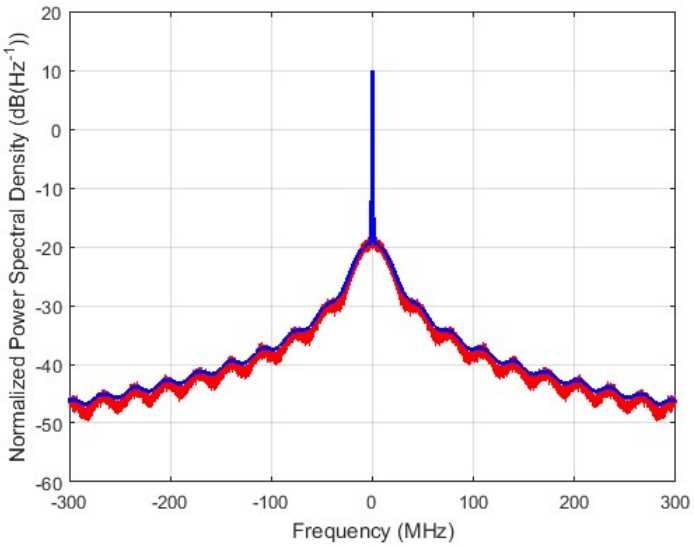

Fig. 2-14. Numerical verification of photocurrent spectrum for $\tau/\tau_c = 1$ and $T = 125\mu s$.

2.2.5.2. SNR in FMCW Lidar, Including Laser Phase Noise

Using the results derived and verified earlier in Section 2.2.5, we can derive a phase-noise-limited SNR. On examination of eq. (2.42), we can apply a scalar for absolute photocurrent ($K_{PD}^2 P_{rx} P_{LO}$) and write SNR using phase noise and detector noise (assumed to be shot noise):

$$SNR_{total} = \frac{s^2}{n_{phase}^2 + n_{shot}^2} \tag{2.43}$$

We will use the following definitions for signal and noise:

$$s^2 = K_{PD}^2 \left[P_{tx} \cdot T sinc^2\left(\frac{T\omega}{2}\right) e^{-\frac{2\tau}{\tau_c}} \cdot L_{LE} \right] P_{LO} \tag{2.44}$$

$$n_{phase}^2 = K_{PD}^2 \left[P_{tx} \cdot \frac{\tau_c}{1+\left(\frac{\omega\tau_c}{2}\right)^2} \left\{ 1 - e^{-\frac{2\tau}{\tau_c}} \left[cos(\omega\tau) + \frac{2}{\omega\tau_c} sin(\omega\tau) \right] \right\} \cdot L_{LE} \right] P_{LO} \tag{2.45}$$

$$n_{shot}^2 = \sigma_{shot}^2 = 2q(K_{PD} P_{LO}) \tag{2.46}$$

As can be seen in eq. (2.44), the signal power includes two extra factors: one due to signal attenuation from phase noise effects, and another (L_{LE}) meant to reflect the loss due to the one-way lidar equation. The phase noise is also attenuated by the loss due to the one-way lidar equation, but, notably, the shot noise does not. This means that the noise limit in a system depends on the amount of laser power received and the power level of the local oscillator. Fig. 2-15 displays the results when eqs. (2.43)-(2.46) are used to calculate a maximum detectable range. Contours represent the maximum detectable range for a given laser linewidth and optical transmit power for a particular receiver condition.

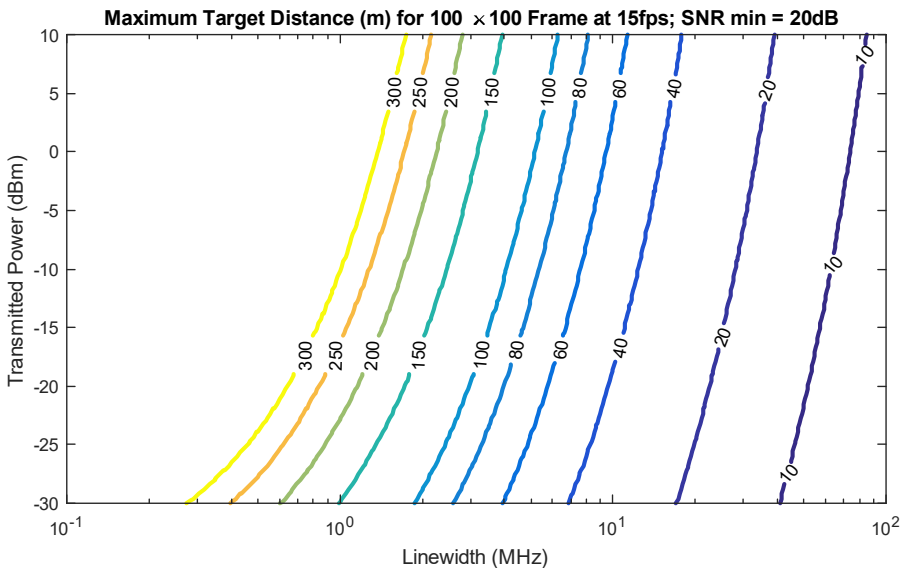

Fig. 2-15. Maximum distance based on SNR including phase noise, shot noise, and target attenuation from the one-way lidar equation.

2.2.6 Beam Steering Considerations

Most of this dissertation focuses on the design, development, and implementation of the light source and receiver, though the method by which a full 3D image is acquired must be considered when designing a complete system. Several schemes exist for acquiring a 2D array of depth measurements. A common scheme requires raster scanning a single pixel lidar sensor around the desired field of view. This scheme has been successfully integrated into some commercial products, though these systems are limited in their frame acquisition rates by the limited speed of the scanner. Another scheme requires illumination of the entire field of view at once, and an array of receivers to collect and process the reflected signals. This scheme can achieve higher frame rates due to the inherent parallelization in the scheme, though it is often severely limited in maximum range. Maximum range is limited due to eye-safety restrictions, given that the transmitted light must now be used over a large field of view and the maximum permissible exposure *per receiver* must now be lower. This reduces the SNR for each receiver, reducing the maximum range of each sensor.

3 FMCW Lidar Utilizing Optoelectronic Phase Locked Loop (OPLL)

3.1 Feedback in Optoelectronic Systems

Lasers have historically been very useful in coherent communication, and RF/mm-wave generation. However, these systems were often bulky and expensive, due to strict requirements on the noise (linewidth) of the lasers used. Semiconductor lasers are interesting candidates for integration due to their low cost and capability to be integrated into compact platforms, but often have higher intrinsic noise (linewidth). Optoelectronic phase-locked loops (OPLLs) have shown significant promise in being able to render semiconductor lasers useful in laser phase-noise-constrained systems, due to the fact that low-cost lasers can be used. Various types of optoelectronic feedback and feedforward systems have been explored extensively in the literature, for applications in "coherence cloning" [37], linewidth reduction [38], phase-controlled laser aperture arrays [39], among many others (we refer readers to a comprehensive exploration of OPLL applications in [40]. In this chapter, we will focus on a particular OPLL architecture, first explored by [41], for use as a control scheme for tunable laser sweeps.

This chapter is structured as follows: first, we will discuss principles and transfer function analysis of the OPLL for swept-source control; second, we will discuss in detail the integration of such an OPLL at the chip-scale; lastly, we will show imaging results using the integrated OPLL in a configuration for FMCW lidar.

3.2 Optoelectronic Phase-Locked Loop Principles and Analysis for Swept-Source Control

Phase-locked loops (PLLs) are often used in electronic frequency synthesis. Essentially, a feedback scheme generates a signal that is phase-matched to an input control signal, sometimes with a multiplier. PLLs have widespread application in clock synthesis and signal demodulation.

In the case of the optoelectronic PLL (OPLL), we are interested in using the feedback loop to suppress noise added by the VCO. Specifically, we are interested in using the PLL input oscillator to control the phase of a tunable-laser/MZI beat signal. Because the noise of the MZI beat signal is related to the phase noise of the tunable laser, we expect that the OPLL should be capable of reducing the phase noise of the laser, with certain spectral limitations. In this chapter, we will review the typical design of a Type-II PLL, parameterize the PLL's VCO noise transfer function, and examine the constraints of VCO design using a tunable-laser/MZI.

3.2.1 The Integrator/Tunable Laser/MZI as a Voltage-Controlled-Oscillator

A "charge-pump" PLL is constructed according to Fig. 3-1, with four primary components: the phase-frequency detector (PFD); the charge-pump (CP); the loop filter (LF); and the voltage-controlled oscillator (VCO). The PFD accomplishes the job of detecting the frequency-difference between the input signal and the output signal, and providing negative feedback based on this difference. This coarse frequency detection naturally shifts to detecting the phase-difference between the input and output, thus the phase difference can be used as well. The charge-pump transduces the PFD output into a current signal. The current signal is conditioned by the loop-filter to generate a control voltage, which controls the phase of the VCO. The VCO contributes one pole to the PLL transfer function, while the loop filter contributes another pole. Since there are two poles are at the origin for the open-loop transfer function, this is referred to as a "Type-II" PLL [42].

Type-II PLL parameters can be selected to optimize the system transfer function for desired behavior. Typically, designers may optimize for stability (via phase-margin design) and damping (via transient analysis and quantification of settling time). Table 3-1 gives the transfer function for each block shown in Fig. 3-1.

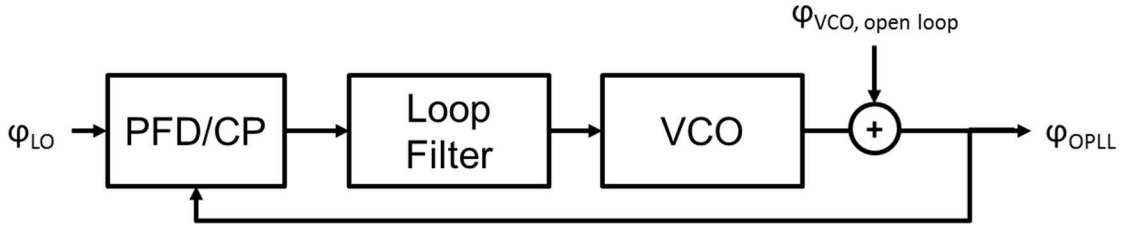

Fig. 3-1. Block diagram for phase-locked loop.

Table 3-1 Transfer Functions for Type-II PLL

Block	Transfer Function	Transfer Function Units
PFD/CP	$H_{PFD}(s) = \frac{1}{2\pi} \cdot I_P = K_{PFD/CP}$	$[A/rad]$
LF	$H_{LF}(s) = \frac{1}{C_1 s} + R_1$	$[V/A]$
VCO	$H_{VCO}(s) = \frac{K_{VCO}}{s}$	$[rad/V]$
Open Loop	$H_{Open}(s) = H_{PFD}(s) \cdot H_{LF}(s) \cdot H_{VCO}(s) = \frac{K_{PFD/CP}K_{VCO}}{s}\frac{1}{C_1 s}(1 + R_1 C_1 s)$	$[rad/rad]$
Closed Loop	$H_{Closed}(s) = \frac{\frac{K_{PFD/CP}K_{VCO}}{C_1}(1+R_1C_1s)}{s^2+K_{PFD/CP}K_{VCO}R_1s+\frac{K_{PFD/CP}K_{VCO}}{C_1}}$	$[rad/rad]$
VCO Phase Noise Closed Loop	$\frac{\phi_{out}}{\phi_{VCO}} = \frac{1}{1-K_{PFD/CP}\frac{K_{VCO}}{s}\left(\frac{1}{C_1 s}+R_1\right)}$	$[rad/rad]$

We can design the loop to optimize for stability by examining the poles of the closed-loop transfer function for the loop. We re-write this transfer function for simplicity:

$$H_{Closed}(s) = \frac{2\zeta\omega_n s+\omega_n^2}{s^2+2\zeta\omega_n s+\omega_n^2} \tag{3.1}$$

Using

$$\omega_n = \sqrt{\frac{K_{PFD/CP}K_{VCO}}{C_1}} \tag{3.2}$$

$$\zeta = \frac{R_1}{2}\sqrt{K_{PFD/CP}K_{VCO}C_1} \tag{3.3}$$

It can be shown that the 3-dB bandwidth, ω_{3dB}, is equal to,

$$\omega_{3dB} = \omega_n\sqrt{1 + 2\zeta^2 + \sqrt{(1 + 2\zeta^2)^2 + 1}} \tag{3.4}$$

A value for ζ can be selected that maintains control loop stability. In the OPLLs designed in this dissertation, we will consider tunable laser components with limited modulation bandwidths, so we will impose a maximum bandwidth for the OPLL. This constrains the natural frequency of the OPLL:

$$\omega_n < \frac{\omega_{max\,BW}}{\sqrt{1+2\zeta^2+\sqrt{(1+2\zeta^2)^2+1}}} \tag{3.5}$$

The settling time of the PLL can be shown to lie in the vicinity of $\frac{1}{\zeta\omega_n}$. The discrete nature of a charge-pump phase/frequency detector requires the PLL settling time to be much longer than the input period of the reference oscillator, so that continuous-time approximations can be followed. In other words,

$$\frac{1}{\zeta\omega_n} \gg \frac{1}{\omega_{LO}} \tag{3.6}$$

In addition, general PLL design calls for increased closed-loop bandwidth in order to increase VCO phase noise suppression. In our designs, VCO input bandwidth is limited, while VCO phase noise is not. This is a consequence of the tunable laser's nature: electronic tuning is achieved through some mechanism (these could be thermal modulation, carrier injection, or MEMS modulation), while noise can be dominated by intrinsic spontaneous emission.

Using the open-loop transfer function given in the table, we can show that the phase margin of the PLL exhibits dependence on the VCO gain. In addition, we can also show that the VCO phase noise is effectively high-pass filtered in closed loop operation. VCOs typically exhibit certain spectral noise characteristics, but in this dissertation, we will not discuss those sources of noise since they are not relevant to our VCO design. Instead, we will introduce laser phase noise due to spontaneous emission and translate it into electrical VCO noise. As we will explain, the tunable-laser VCO noise will be correlated to the tunable-laser VCO gain. Thus, it will be necessary to define a different transfer function for laser phase noise in a closed-loop OPLL.

In studying phase noise behavior for OPLLs, we will examine dominant noise terms for various common tunable-laser noise sources, such as spontaneous emission, tuning-induced shot and thermal noise, and MEMS Brownian motion. While textbook analyses usually approach phase noise shaping with reference to the VCO, we will instead focus on the phase noise of the tunable laser itself, and study the shaping of laser phase noise by the OPLL.

3.2.2 Phase Noise in the Optoelectronic Phase-Locked Loop

In order to derive the laser phase noise transfer function, we will further examine the VCO block as it is designed in [41]. The VCO block consists of a tunable laser injected into a Mach-Zhender Interferometer (MZI), followed by a photodiode with RF amplification. The tunable laser and photoreceiver may exhibit electrical low-pass behavior, so it is important to consider poles introduced by the tuning mechanisms in a given laser. This is especially important

for MEMS-tunable devices, due to possible resonances in frequency response. We will examine resonant behavior in later sections.

The typical VCO transfer function is given in Table 3-1. Therefore, in order to effectively design an OPLL, we must approximate this transfer function appropriately with the tunable-laser/MZI VCO. This is achieved by using the blocks as shown in Fig. 3-2.

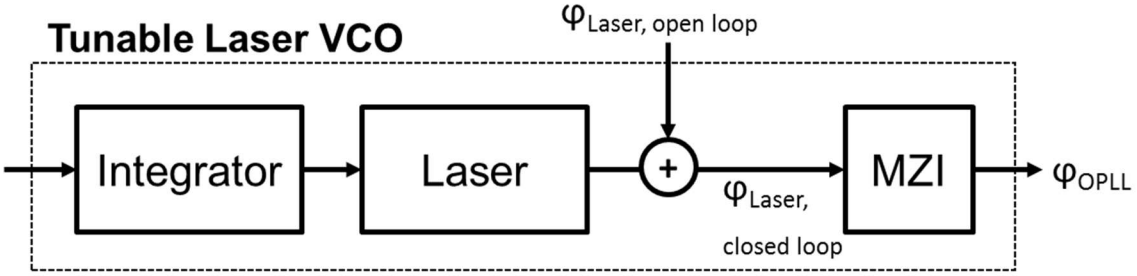

Fig. 3-2. VCO implemented with integrator, tunable laser, and Mach-Zhender Interferometer (MZI). Laser phase noise is modeled as injected noise on the phase before the MZI. VCO phase noise is modeled by propagating laser phase noise through the MZI.

The tunable laser itself is a voltage controlled oscillator at optical frequencies, so we can model the laser as an integrator with respect to phase:

$$H_{TL}(s) = H_{FM}(s)\frac{K_{laser}}{s}[rad/A] \tag{3.7}$$

Where K_{laser} represents the tuning gain of the laser, and $H_{FM}(s)$ represents the frequency-modulation (FM) response of the laser. If this term exhibits low-pass behavior, PLL parameters must be chosen so that this term can be approximated as unity within the PLL bandwidth.

The MZI output intensity is accurately modeled with the delay, τ:

$$H_{MZI}(s) = 1 - e^{-s} \approx s\tau[rad/Hz] \tag{3.8}$$

Where we have used the first-order Taylor expansion approximation for the exponential. In the following sections, we will use the first-order Taylor expansion approximation in analysis, for ease of use. However, in analytical plots and numerical simulations, we will use the full expression without simplification.

In order to generate a beat signal in intensity at the output of the MZI, we need to tune the laser frequency. The rate of this frequency sweep, γ, is proportional to the frequency at the output of the MZI. (We will assume, for the case of the OPLL, that the MZI path length difference is a design parameter.) Therefore, we will use an ideal integrator before the tunable laser, such that a constant input to the integrator generates a linear signal at the output. The integrator gain and the level of the input will set the γ-parameter. The integrator transfer function is given below:

$$H_{integrator}(s) = \frac{K_{integrator}}{s}[A/V] \tag{3.9}$$

Where $K_{integrator}$ is the integrator gain and has units of $\left[\frac{A}{V}\cdot Hz\right]$. Finally, the transfer function for the optoelectronic VCO is given:

$$H_{VCO}(s) = \frac{K_{int}}{s}H_{FM}(s)\frac{K_{laser}}{s}(1 - e^{-s\tau}) \approx \frac{K_{int}K_{laser}\tau}{s} \tag{3.10}$$

Thus, we have derived an approximate VCO transfer function, and assumed that the tunable laser has a flat FM response.

In order to study the laser phase noise-shaping properties of the OPLL, we will study the block diagram shown in Fig. 3-3. We can write the closed-loop transfer function for laser phase noise:

$$H_{\frac{laserPNout}{\phi n}}(\omega) = \frac{\phi_{laser,out}}{\phi_{laser,in}} = \frac{s^2}{s^2 + K_{PFD/CP}K_{int}K_{tune}\tau R_1 s + \frac{K_{PFD/CP}K_{int}K_{tune}\tau}{C_1}} \tag{3.11}$$

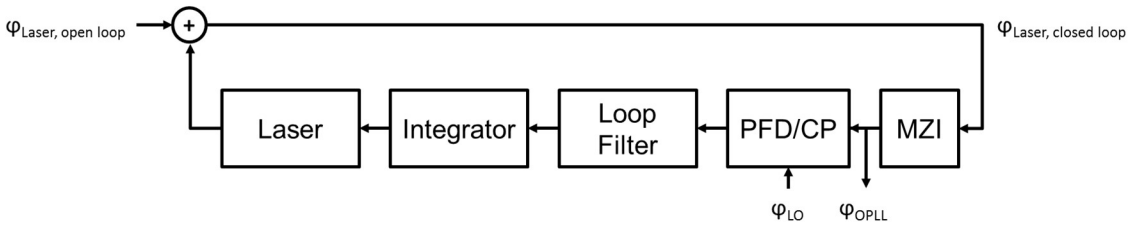

Fig. 3-3. Block diagram PLL for examining the transfer function of laser phase noise.

In contrast, we can write the closed-loop transfer function for laser phase noise with reference to VCO phase noise:

$$H_{\frac{VCOPN}{laserPN}}(\omega) = \frac{\phi_{VCO}}{\phi_{laser,in}} = \frac{s^2(s\tau)}{s^2 + K_{PFD/CP}K_{int}K_{tune}\tau R_1 s + \frac{K_{PFD/CP}K_{int}K_{tune}\tau}{C_1}} \tag{3.12}$$

If we were using this system as a frequency synthesizer, this noise transfer function would be important to consider. However, in our case, we will be using our laser signal to measure range, thus we must consider the phase noise on the laser signal. We will use a very slightly modified version of the VCO phase-noise transfer function to examine the phase noise spectral shape for target signals with delays other than τ.

It is prudent to express the OPLL-VCO phase noise transfer functions in terms of natural frequency and damping factor, as shown below:

$$H_{\frac{laserPNout}{\phi n}}(\omega) = \frac{s^2}{s^2 + 2\zeta\omega_n s + \omega_n^2} \tag{3.13}$$

$$H_{\frac{VCOPN}{laserPN}}(\omega) = \frac{s^2}{s^2 + 2\zeta\omega_n s + \omega_n^2}(s\tau) \tag{3.14}$$

Where $\zeta = \frac{R_1}{2}\sqrt{\tau K_{PFD/CP}K_{int}K_{tune}C_1}$ and $\omega_n = \sqrt{\frac{K_{PF\ /CP}K_{int}K_{tune}\tau}{C_1}}$. These expressions represent two-pole systems, but with two or three zeros at the origin. Therefore, we expect high-pass behavior for laser phase noise.

3.2.3 OPLL Loop Parameter Design

A limiting factor in PLL design for FMCW is the electronic bandwidth of the tuning mechanism for the tunable laser. This bandwidth can be deduced from the FM response of the tunable laser. Assuming the laser has a tuning bandwidth of B Hz, we can derive some limits on the design of an FMCW utilizing the laser. In order to preserve sharp corners given by harmonics for a triangular modulation scheme, we can specify a minimum ramp period:

$$T_{ramp} > T_{min} = \frac{20}{B} \tag{3.15}$$

T_{ramp} is a free parameter, though it will be advantageous to minimize this period for reasons that will be clear in the following analysis. We will treat T_{ramp} as a value derived from laser FM

bandwidth. Given a maximum frequency excursion for the laser, Δf, we can specify a maximum tuning rate, γ:

$$\gamma = \frac{\Delta f}{T_{ramp}} < \frac{\Delta f}{T_{min}} = \gamma_{max} \tag{3.16}$$

Finally, we have a free parameter, τ_{MZI}, which we can select to optimize OPLL performance. For this analysis, we will leave it as a free parameter. The nominal MZI beat frequency will be given by:

$$f_{MZI} = \gamma \tau_{MZI} = \frac{\Delta f}{T_{min}} \tau_{MZI} = \frac{B \cdot \Delta f}{20} \tau_{MZI} \tag{3.17}$$

Next, we will use the constraint that the PLL closed-loop bandwidth should be less than the nominal MZI beat frequency and the laser's tuning bandwidth. We will use a factor of 20x to guarantee this constraint and reduce the effects of loop delays and poles due to other parasitics.

$$\omega_{3dB} = 2\pi \cdot min\left(\frac{f_{MZI}}{20}, \frac{B}{20}\right) \tag{3.18}$$

In implementations considered in this dissertation, we will assume that the laser tuning bandwidth will be the dominant constraint on the loop bandwidth. This can be justified by examining the term, $\Delta f \cdot \tau_{MZI}$, which indicates the number of fringes during a single laser sweep through a particular MZI. In order for the MZI beat frequency to be the dominant loop bandwidth constraint, the number of fringes must be less than 1, which violates a continuous-time approximation for type-II PLLs.

Our goal now is to select loop parameters that will provide the loop bandwidth as constrained by the tuning bandwidth. We know that the loop bandwidth is parameterized by ω_n and ζ. We can treat the damping factor, ζ, as a free variable, though it will be important to consider that this parameter affects the settling time for the OPLL, and thus, the linearity of the laser frequency sweep. A typical value to achieve reasonable settling times is $\zeta = 0.7 \sim 1$. We can express eq. (3.5) as an equality to solve for the natural frequency of the closed loop system:

$$\omega_n = \frac{\omega_{3dB}}{\sqrt{1+2\zeta^2+\sqrt{(1+2\zeta^2)^2+1}}} = \frac{2\pi}{20} \frac{B}{\sqrt{1+2\zeta^2+\sqrt{(1+2\zeta^2)^2+1}}} \tag{3.19}$$

Therefore, we can write expressions for the loop filter parameters that maintain the desired maximum loop bandwidth given a selected value for the damping factor:

$$R_1 = \frac{2\zeta\omega_n}{K_{PFD/CP} K_{int} K_{laser} \tau} \tag{3.20}$$

$$C_1 = \frac{1}{\omega_n^2} K_{PFD/CP} K_{int} K_{laser} \tau \tag{3.21}$$

The natural frequency, ω_n, as specified in equation (3.19), represents a maximum value. In the design for a particular laser, it will be desirable to operate at the maximum loop bandwidth, but selection of the damping factor and natural frequency will depend on the requirements of the application in terms of settling time and laser phase noise reduction.

3.2.4 OPLL Laser Phase Noise Shaping

It has been shown that spontaneous emission leads to a flat frequency noise spectrum, exhibiting a power spectral density:

$$S_{\dot{\phi}_n}(\omega) \equiv \Delta\omega \text{ [rad/s]} \tag{3.22}$$

where $\dot{\phi}_n$ represents the radial frequency noise due to spontaneous emission, and $\Delta\omega$ is commonly referred to as the linewidth of spontaneous emission, with units of [radians/seconds]. Power spectral density of laser phase noise is derived by taking an integral in the time domain, so division by frequency parameter in the frequency domain:

$$S_{\phi_n}(\omega) = \frac{\Delta\omega}{\omega^2} \tag{3.23}$$

In order to derive the effect of the OPLL on this phase noise PSD, we can apply the previously-derived transfer functions in the following manner:

$$S_{laserPNout}(\omega) = \left|H_{\frac{laserPNout}{\phi_n}}(\omega)\right|^2 \frac{\Delta\omega}{\omega^2} = \frac{\omega^4}{\left(\omega^2-\omega_n^2\right)^2+4\zeta^2\omega_n^2\omega^2}\left(\frac{\Delta\omega}{\omega^2}\right) \tag{3.24}$$

$$S_{VCOPN}(\omega) = \left|H_{\frac{VCOPN}{laserPN}}(\omega)\right|^2 \frac{\Delta\omega}{\omega^2} = \frac{\omega^6\tau^2}{\left(\omega^2-\omega_n^2\right)^2+4\zeta^2\omega_n^2\omega^2}\left(\frac{\Delta\omega}{\omega^2}\right) \tag{3.25}$$

The first relation for output laser phase noise is a common expression for VCOs that exhibit white frequency noise. The second relation for VCO phase noise is unique to the case of a tunable-laser VCO exhibiting spontaneous emission noise. It corresponds to the phase noise spectrum for a beat signal in FMCW lidar as shaped by the OPLL transfer function. The expression can be adapted to analyze phase noise on a target beat signal by changing the delay parameter in the numerator (τ^2) to the delay parameter for the target (τ_{target}^2).

3.3 Implementation of Chip-Scale OPLL for Electronically-Tuned DBR Laser

As stated in Section 1.3, the primary driver for integrated photonics and electronics is the data communication industry. Progress in this field has led to fabrication processes that can be used for a plethora of other applications beyond data communications. In this section, I outline the design, packaging, and testing of heterogeneously integrated electronics and photonics for use in the OPLL design described in Section 3.2.

The chip-scale OPLL is used to support two research aims: first, to demonstrate the ability to integrate photonics heterogeneously with electronics, and second, to demonstrate the capability of creating a compact opto-electronic system that can be used as a lidar source. To meet these ends, we designed a process in which the optoelectronic components of the OPLL (fiber couplers, MZI, photodiodes, and interposer routing) could be fabricated on a silicon-on-insulator wafer, and the electronic components of the OPLL (TIA, phase-frequency detector, loop filter, and ramp generator) could be fabricated in a standard 180nm CMOS process. The chips would then be bonded together at the die level, in order to demonstrate the feasibility of extending the bonding process to the wafer-scale. Although we used in-house processing techniques at the time for the photonics chips, most of the silicon photonics fabrication can now be achieved through multi-project wafer (MPW) runs at the foundry level. An important novel development in this project was the use of through-silicon-vias (TSVs) to interface photodetectors on the topside of the photonics chip with the CMOS chip underneath. Fig. 3-4 shows a schematic cross-section of the silicon photonics wafer with TSVs for routing photodiode leads to the backside of the wafer.

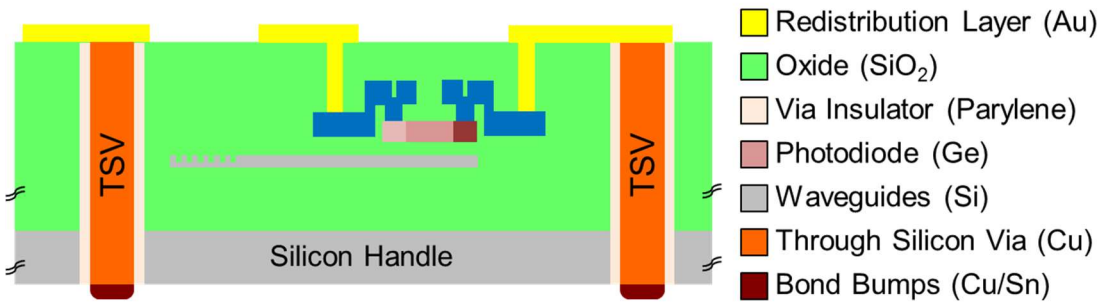

Fig. 3-4. Cross-section of silicon photonics chip processed with through-silicon-vias (TSVs). Cartoon depicts a grating coupler with photodiode, and photodiode is electronically routed to backside of the silicon wafer handle.

This section is structured as follows. First, I will describe several practical considerations, such as laser bandwidth, and chip fabrication errors, which limit the design space of the OPLL. Second, I will give an overview of the various components used in the OPLL which were integrated in a silicon photonics process. I will also review several important characteristics of the photonics fabrication process. Third, I will discuss the characterization and testing of these components, with an aim toward justifying the screening of photonics chips for packaging. Fourth, I will review the flip-chip packaging method for bonding the silicon photonics chip to the electronics chip. Lastly, I will review experimental results for system operation and show results of a demonstration which uses the linearized DBR source as an FMCW imaging source.

3.3.1 Silicon Photonics Design and Characterization

Photonic chips for the integrated FMCW source were fabricated in the UC Berkeley Marvell Nanolab in a 220nm silicon-on-insulator process. The process included two etch steps: a full silicon etch and a partial 70nm silicon etch. In addition, a rapid-melt-growth germanium process was used to create p-i-n photodiodes in a so-called “wrap-around” configuration, as described in [43]. Fig. 3-5 shows the layout of the silicon photonics chip, with labels for fiber couplers, on-chip optical delay lines, germanium photodiodes, wirebonding pads, and through-silicon-via (TSV) locations.

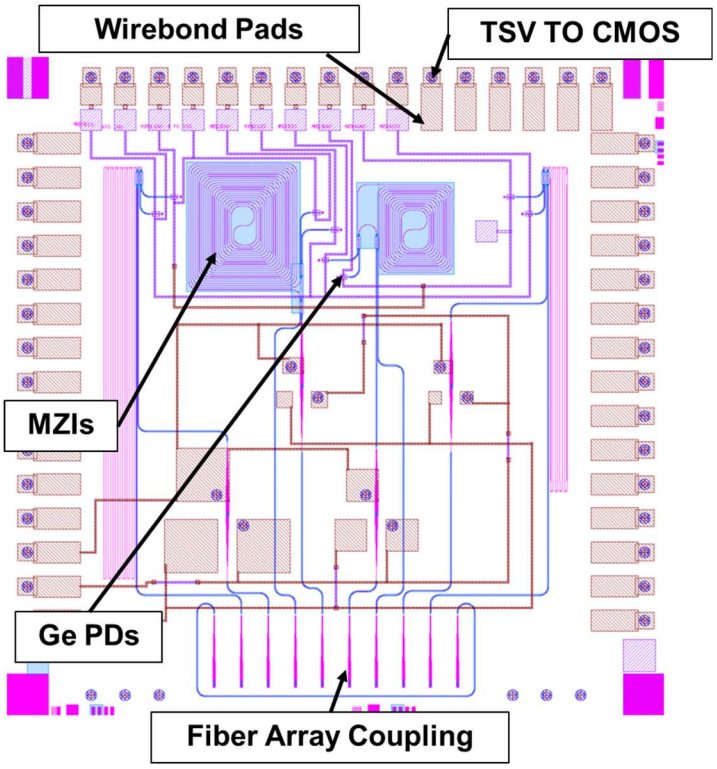

Fig. 3-5. Layout of silicon photonics chip with fiber couplers, directional couplers, Mach-Zehnder interferometers, germanium photodiodes, wirebonding pads, and through-silicon via (TSV) locations noted.

The on-chip photonic devices include fiber to waveguide grating couplers, directional couplers, low-loss delay lines, and photodetectors with electrical interface to the backside of the chip. Grating couplers are arranged in an array with 127um pitch, matched to the pitch of a fiber array. Delay lines are used to create fixed asymmetric Mach-Zehnder interferometers (MZIs) with free spectral ranges (FSR) of 1.5 GHz and 3 GHz. Photodiodes were designed for responsivities of 0.8 A/W.

The grating coupler array configuration allows repeatable and reliable fiber-to-chip coupling, through the use of a “loop-back coupler.” In the loop-back coupler, the first and last grating coupler are connected through a single mode waveguide. The first coupler is used as an input device, and the last as an output device. By adjusting the spatial position and orientation of a fiber array, we optimize the coupling through the loop-back device by maximizing the received optical power. When the optical power is maximized, the device grating couplers are optimally aligned with all other fibers in the array. This alignment technique allows the simultaneous or sequential testing of several on-chip components without the need to re-align the fiber and chip for each device. Using the grating coupler array, we typically achieved an insertion loss of 5-7dB per coupler. Fig. 3-6 shows the alignment structure for the fiber array and a microscope photograph of the manual fiber array alignment.

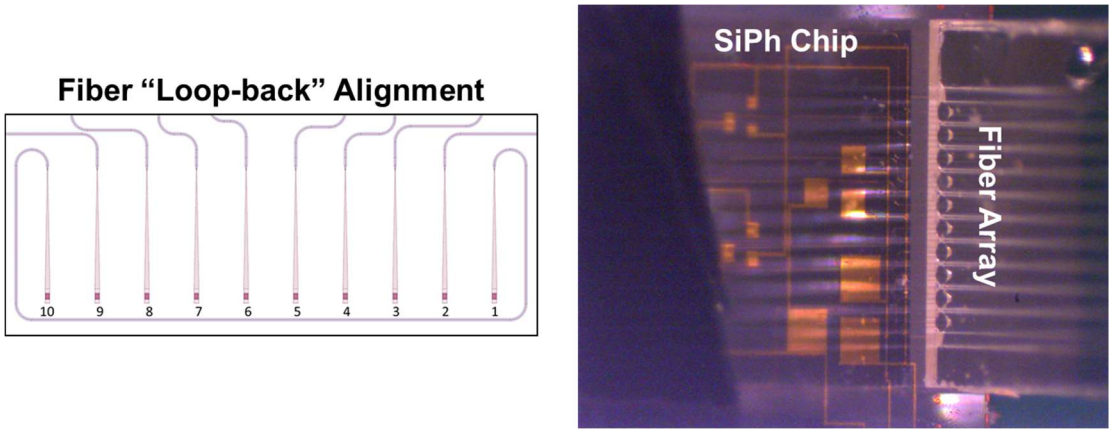

Fig. 3-6. Coupling light into the chip via grating coupler array.(Left) fiber loop-back configuration for alignment of 8 optical fibers simultaneously; (right) photograph showing microscope photograph of optical coupling to silicon photonics chip through a pitch-matched fiber array.

Germanium photodiodes (GePDs) were characterized by measuring reverse-bias IV curves in both dark and illuminated states, in order to determine dark current and responsivity. SOI-chips were selected for system integration based on photodiode dark current and responsivity, with minimum requirements determined by CMOS interface design: minimum responsivity ~0.7 A/W, maximum dark current ~0.5uA. Fig. 3-7 shows typical light and dark IV curves for a GePD on these chips.

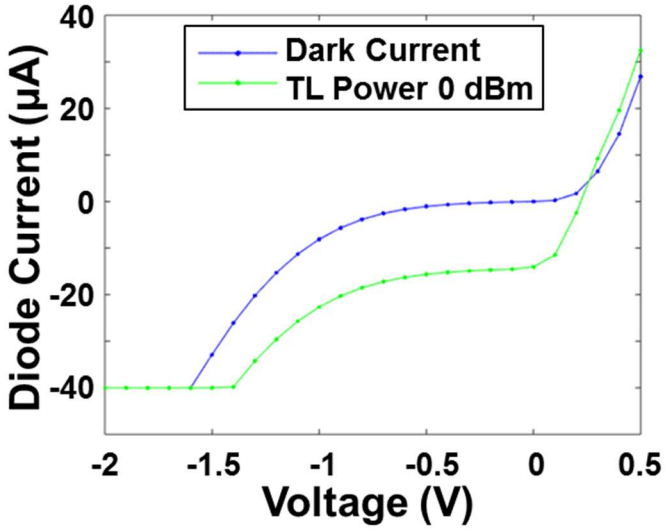

Fig. 3-7. Typical light- and dark-IV curves for the GePD on the silicon photonics chips.

The on-chip MZIs were designed with 150ps (2.5cm physical length) and 330ps (5.0cm) delays, using 50/50 directional couplers as splitter and combiner. Two different waveguide configurations were designed for the delay lines, and test structures verified the loss of each waveguide configuration. One configuration uses a so-called “ridge” configuration, while the other uses a wide (1.2um) waveguide, in order to reduce loss due to edge roughness. In order to avoid the excitation of multiple modes in the 1.2um waveguide bends, the waveguide is tapered to 500nm wide before bending. The loss in the 5cm delay line due to strip bending is negligible compared to the loss of the delay line itself. The output coupler of the MZI is a 2x2 directional

coupler where each output is coupled an on-chip Ge photodiode. We characterized the FSR of each on-chip MZI with a tunable laser and current meter, and typical results for the wide-waveguide MZI are shown in Fig. 3-8.

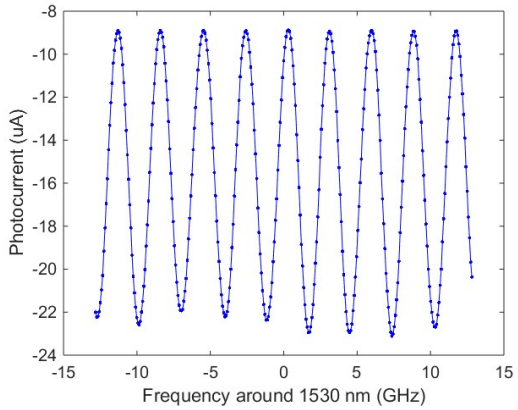

Fig. 3-8. Typical MZI response for a wide-waveguide MZI on a silicon photonics chip.

3.3.2 Known-Good-Die Screening

In order to demonstrate 3D integration of electronics and photonics, we screened individual wafers and individual dies on each wafer for successful bond metallization. Several characteristics needed to be evaluated to select candidates for flip-chip bonding. These included photonic functionality verification (photodiode and interferometer characterization), through-silicon-via (TSV) optical inspection, and CMOS metallization electrical inspection. Due to design rule-violations in CMOS layout, and the development nature of the SOI TSV process, this "known-good-die" (or, KGD) screening process was essential to ensuring some yield from the flip-chip packaging process.

After initial observations, we selected the 330ps wide-waveguide MZI as the design for OPLL operation, due to its low-loss and longer length than the 120ps MZI. Before continuing the chip-screening process with bond-bump characterization, each chip's MZI and photodiode responses were examined together. For each candidate KGD, we placed photonic chips under the fiber array, coarsely aligned the array for optical coupling, and performed four screening steps: 1) wavelength sweep to measure the alignment efficiency for measurement calibration; 2) dark IV curves for each photodiode at the output of the on-chip wide-waveguide 330ps MZI; 3) wavelength sweep to precisely calibrate MZI free spectral range; 4) light IV curves at an MZI peak output for each photodiode.

During chip screening, we did not finely optimize the grating alignment for each chip, instead calibrating each measurement to the "double grating loss" measured for a particular chip and a particular manual alignment. This allowed efficient die screening to take place. These "double-grating loss" measurements are shown in Fig. 3-9. Representative dark current measurements are shown in Fig. 3-10, as well as the distribution of dark current at 0.5V across 37 chips. Fig. 3-11 shows MZI response measurements used to quantify MZI response depth. MZI extinction ratio is a function of both waveguide loss and exact directional coupler ratios. Since the photodiode responsivities varied somewhat significantly from chip to chip, it was difficult to separate the effects of loss/coupling ratios and photocurrents. However, it was sufficient for this application to measure the holistic extinction ratio of each MZI with photodiodes, in order to select the best candidates for use in the integrated OPLL.

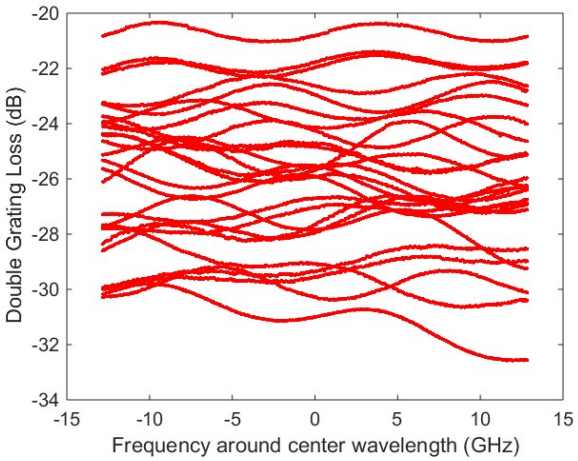

Fig. 3-9. Grating coupler wavelength responses for a selection of 37 chips in the screening process. Variation in level due to variation in manual alignment of fiber array.

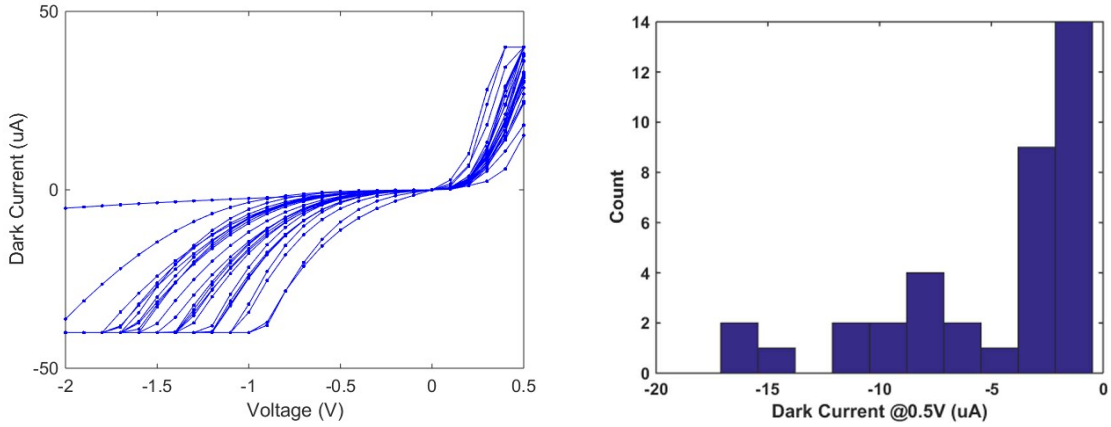

Fig. 3-10. On-chip germanium photodiode response characteristics.(Left) Dark IV curves taken for the same photodiode on 37 chips; (Right) distribution of dark current measurements. Responsivity of each photodiode was calculated after finding a peak in the MZI wavelength sweep.

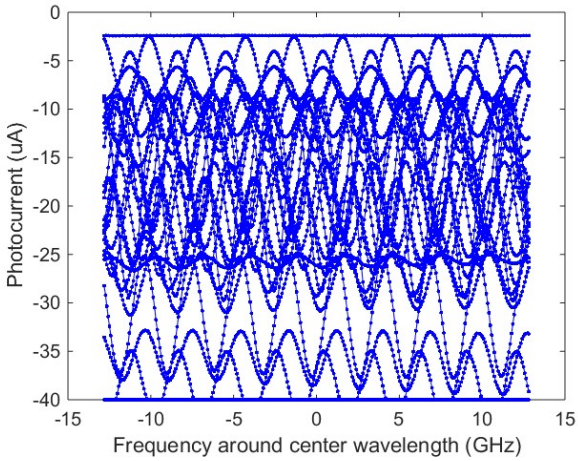

Fig. 3-11. Interferometer photodiode response with respect to wavelength for 37 chips.Extinction ratio of each MZI allows calculation of a relative responsivity for each photodiode candidate.

In addition to the optoelectronic components on the surface of each photonic chip candidate, we also needed to characterize the TSVs on each chip. In the fabrication process for the TSVs, vias were etched to a certain depth, with good uniformity. The vias were insulated with parylene before coated with copper. The backside of the wafer is then removed to reveal the bottom of the copper vias. Copper-tin bond bumps were deposited onto the backside at each via location, in order to assist in the flip-chip bonding process. However, we quickly observed that regions of the silicon photonics wafer did not have TSVs revealed in the backside removal process, and before bond-bumps were added to the backside. This required another KGD characterization step – to identify chip candidates that had proper backside removal. Fig. 3-12 shows an SEM cross-section of the TSVs fabricated on a silicon photonics die. Figs. Fig. 3-13 through Fig. 3-15 show examples of well-bumped and poorly-bumped photonic wafer backsides.

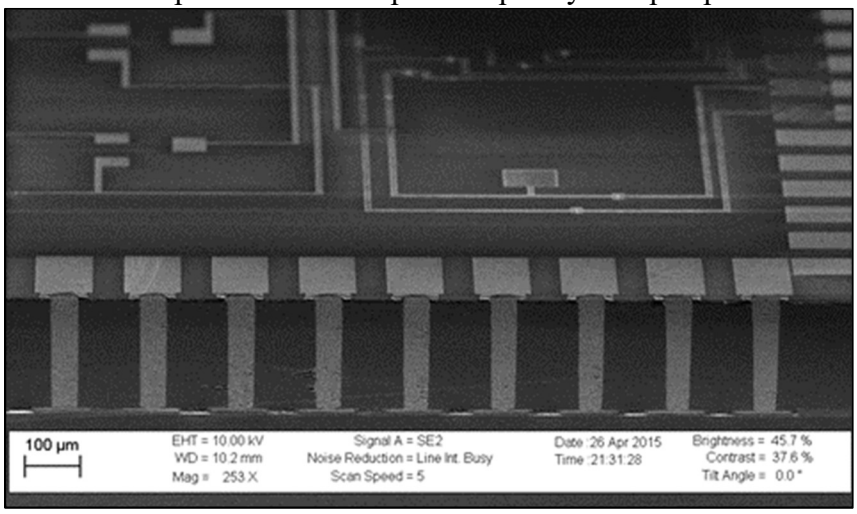

Fig. 3-12. SEM image of cross-section of silicon photonics chip with TSVs.Edge-on view shows metal wirebond pads connected to backside through copper-coated vias.

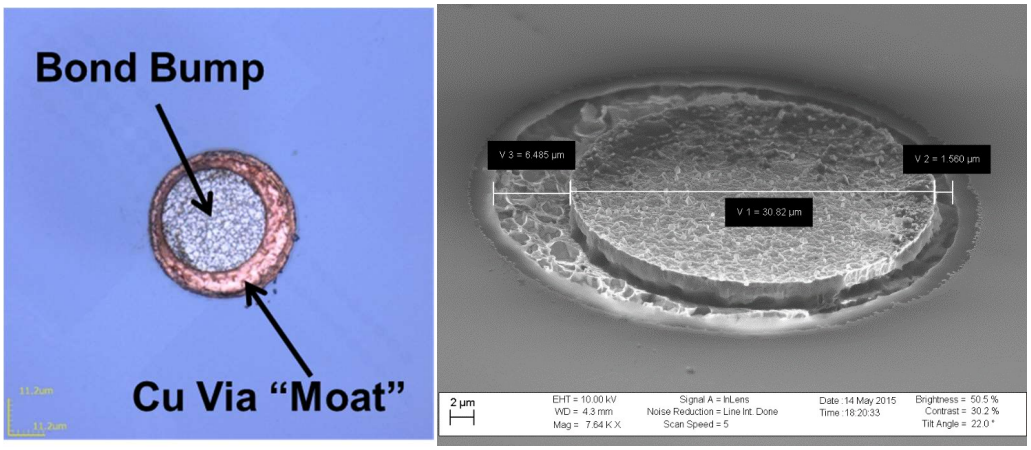

Fig. 3-13. Well-revealed TSV: (Left) Confocal microscope image of revealed TSV on backside of silicon photonics chip. Blue color is silicon wafer handle, orange "moat" shows a well-revealed TSV after backside removal. Silver color is the copper-tin bump deposited properly on top of the copper TSV. (Right) SEM image of revealed TSV with deposited copper-tin bond bump.

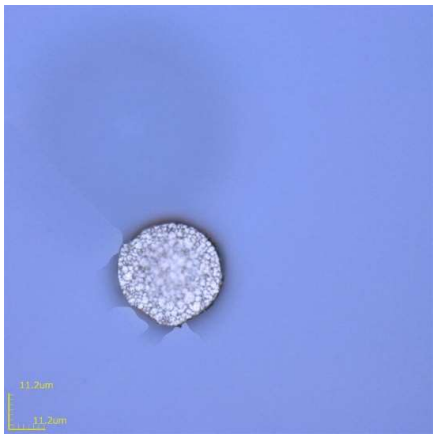

Fig. 3-14. Non-revealed TSV: Confocal microscope image of non-revealed TSV on backside of silicon photonics chip. Blue color is silicon wafer handle, silver color is the copper-tin bump deposited in proper location for TSV, but note absence of the orange copper "moat".

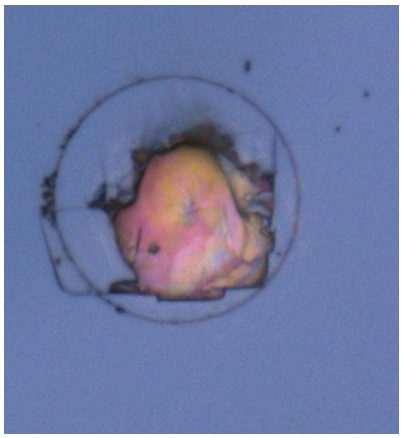

Fig. 3-15. Non-revealed TSV after attempted bonding with CMOS and shearing.Bond bump was not electrically connected with copper via, leading to an unsuccessful electrical bond.

TSV screening was achieved by examining each bond bump on each candidate chip. For each chip, all TSVs were required to exhibit an orange-colored copper "moat" with a grey-colored copper-tin bump within. For any "non-moat" TSV, a confocal microscope was used to examine the profile of the bond bump. A "dishing" feature would be observed for bond-bumps that were more likely to make contact with TSVs when the TSV was not fully revealed. Fig. 3-16 shows the "dishing" feature, where the copper-tin bump forms a crater, or dish-like profile.

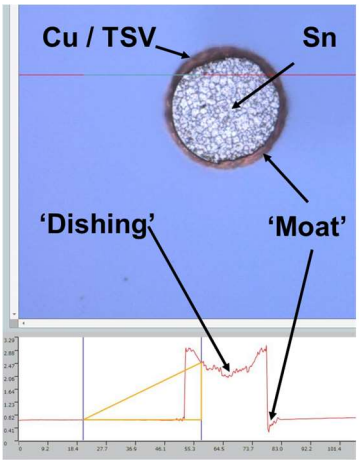

Fig. 3-16. Revealed TSV with both a "moat" and "dishing" feature. These features independently indicate likely electrical contact between the bond bump and TSV, and thus a good candidate for flip-chip bonding.

The CMOS chips were fabricated in a 180nm process with TSMC. Initially (immediately after the finished die fabrication and dicing of the MPW), exposed aluminum bond pads on CMOS are topographically below the passivation layer. In order to make contact with the silicon photonics interposer chip backside, the CMOS pads must be effectively elevated to roughly conform to the SOI backside bumps. We evaluated standard metallization processes offered by CV Inc., a vendor in the area of CMOS bonding and packaging. In collaboration with CV Inc., two electroless metallization processes were evaluated: electroless copper ("eCu"), and electroless nickel-immersion gold ("ENIG"). The eCu and ENIG processes were evaluated based on their apparent selectivity in growth between vertical and lateral directions. Vertical growth is required to meet required pad height for flip-chip packaging, while lateral growth is not desired, since it increases the chance of shorting multiple functional electronic pads.

In the design of the CMOS chip, there were two critical pad areas where the pads came into very close proximity, such that we encountered a very strict constraint on the lateral growth of the metallization processes. In order to prevent too much lateral growth, we evaluated metallization procedures with relatively short growth times. For ENIG processes, we were able to measure metallization heights of 1.7um below the highest feature on the CMOS die, while for the eCu process, we observed metallization as much as 3um above the surface.

3.3.3 Flip-Chip Packaging

In order to integrate the known-good-die photonic chips with known-good-die CMOS chips, we used a "flip-chip" bonding process, using the Finetech Fineplacer Lambda. The flip-chip process requires a thermal time profile and a fixed force to apply to the chip stack. A photonics die is loaded onto a chuck, and picked up by a small vacuum head. After the photonics chip has been picked up, a microscope can view the backside of the photonics chip and the chuck simultaneously. A CMOS die is loaded onto the chuck, and aligned with the future position of the photonics chip before it is lowered by the vacuum head. After lowering, the two chips come into contact and the lower vacuum chuck is heated according to a temperature profile specified for the bonding process. We used a temperature of 300°C for 30 seconds, with a force of 20N, in order to achieve Cu/Sn (photonics backside) bonding with ENIG (CMOS topside).

For process development, we used two different silicon photonic chip designs, that differed in their TSV and pad layout. These designs are shown side by side in Fig. 3-17. For early iterations, we planned to use a version of the SiPh chip with inset bonding pads and correspondingly inset TSVs. The CMOS chip was correspondingly designed to accommodate

both versions of the pad layout. The development layout could be diced closer to the pads of the device, thus exposing outer CMOS bond pads underneath. This allowed for development and debugging of the bonding process, TSV characterization, and ultimately, a successful demonstration of the flip-chip process. Fig. 3-18 shows a microscope photograph of the development SiPh chip bonded to the CMOS chip, with exposed CMOS pads for process development and debugging.

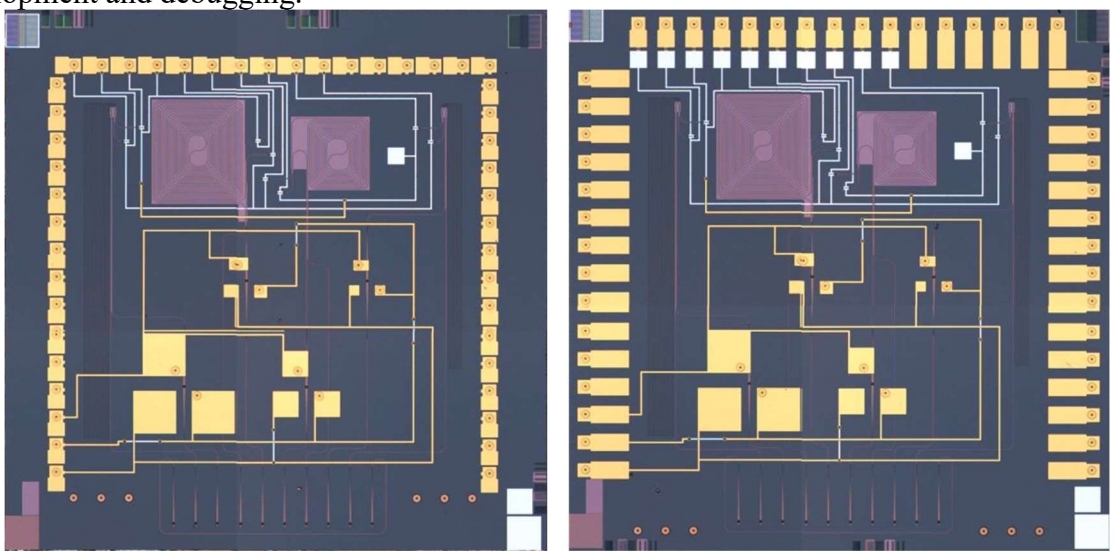

Fig. 3-17. Silicon photonic chip designs for flip-chip packaging tests. (Left) Development layout with inset bonding pads and correspondingly inset TSVs. (Right) Demonstration layout without inset pads and TSVs.

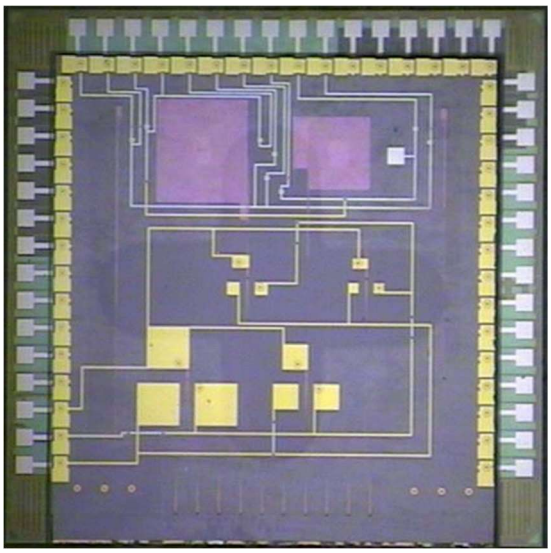

Fig. 3-18. Edge-diced silicon photonic development chip bonded to CMOS after flip-chip bonding.

3.3.4 Evaluating TSV Functionality through OPLL System Testing

In order to test the functionality of the system after flip-chip bonding, we first wirebonded the top-side of the silicon photonics chip to corresponding pads on a small printed circuit board (referred to as the “daughter board”). The daughter board with different integrated chip configurations is shown in Fig. 3-19. This daughter board was affixed to a larger motherboard which was mounted on an x-y-z stage. The motherboard contained electronics for various required chip voltages, as well as a mount for a compact Opal-Kelly FPGA for some

CMOS parameter selection. The motherboard routed the chip-generated voltage ramp to an external DBR tunable laser via an RF SMA connector. Light was coupled into the photonics chip via fiber array coupler; Fig. 3-20 shows the daughter board mounted with fiber array probe and microscope for coarse fiber array alignment. Functionality of the full system was evaluated using the testing configurations shown in Figs. Fig. 3-21 through Fig. 3-23.

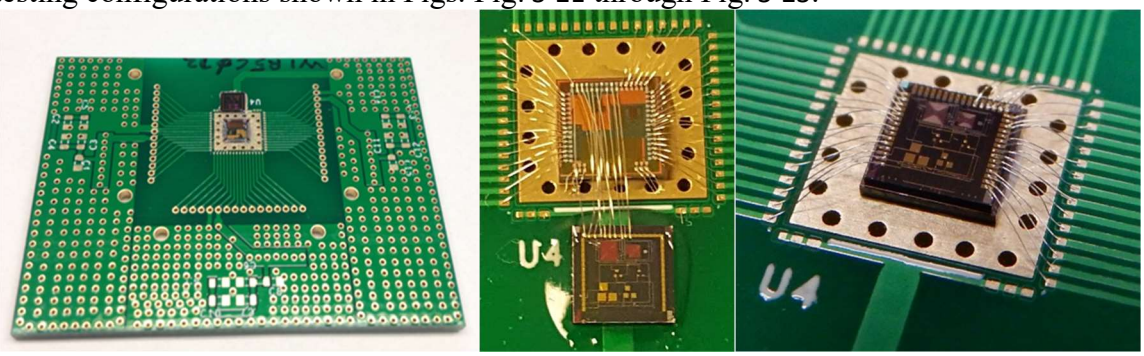

Fig. 3-19. Chip-level OPLL on PCB "daughter board."(Left) Chips mounted "side-by-side" on daughterboard. (Middle) Close-up photograph of photonics chip and electronics chip wirebonded in a "side-by-side" configuration for system testing. (Right) Single chip integration of photonic and electronic chips for "integrated OPLL testing.

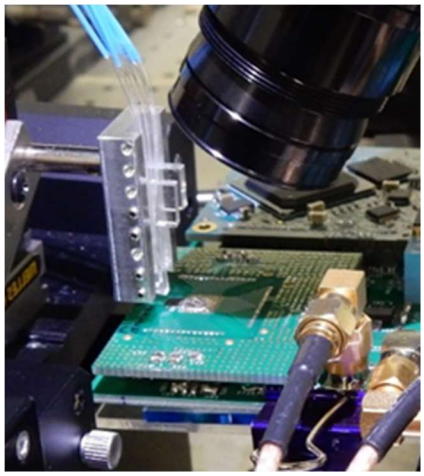

Fig. 3-20. Side-by-side chip probe measurement. A stage-mounted fiber array is coupled into the photonics chip, which is mounted on the daughter-board and wirebonded directly to CMOS. Integrated chip evaluation is performed with the same measurement setup.

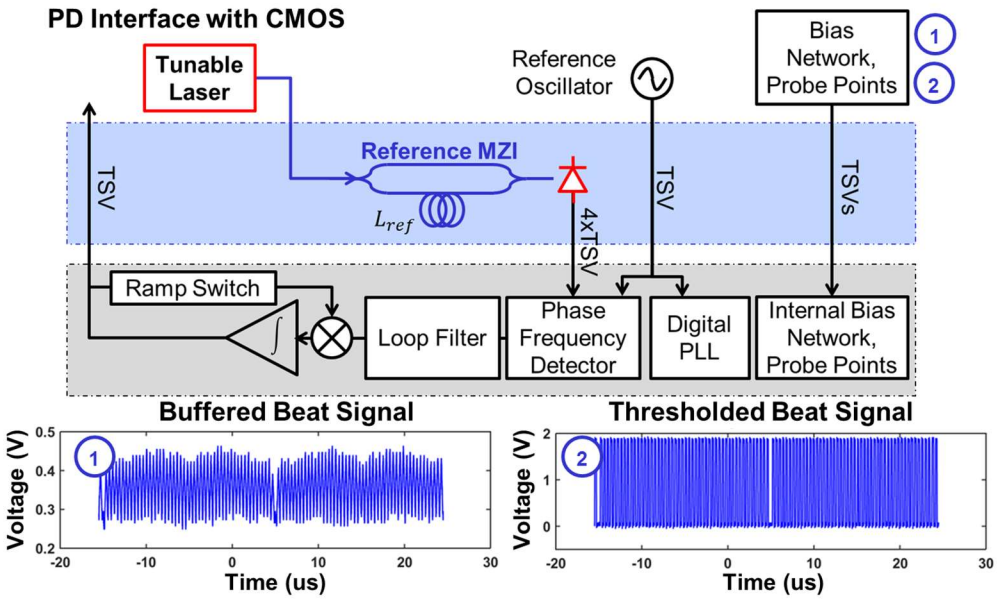

Fig. 3-21. Bonded stack configuration for verification of photodiode-TIA interface.A tunable laser is tuned externally (not by CMOS electronics) and the output of the TIA ((1) on the figure, labeled "Buffered Beat Signal") and Schmitt trigger ((2) on the figure, labeled "Thresholded Beat Signal") on CMOS are measured on motherboard probe points. This test indicates TIA/Schmitt bias networks are properly connected through TSVs, and that photodiodes on silicon photonics are properly connected through TSVs.

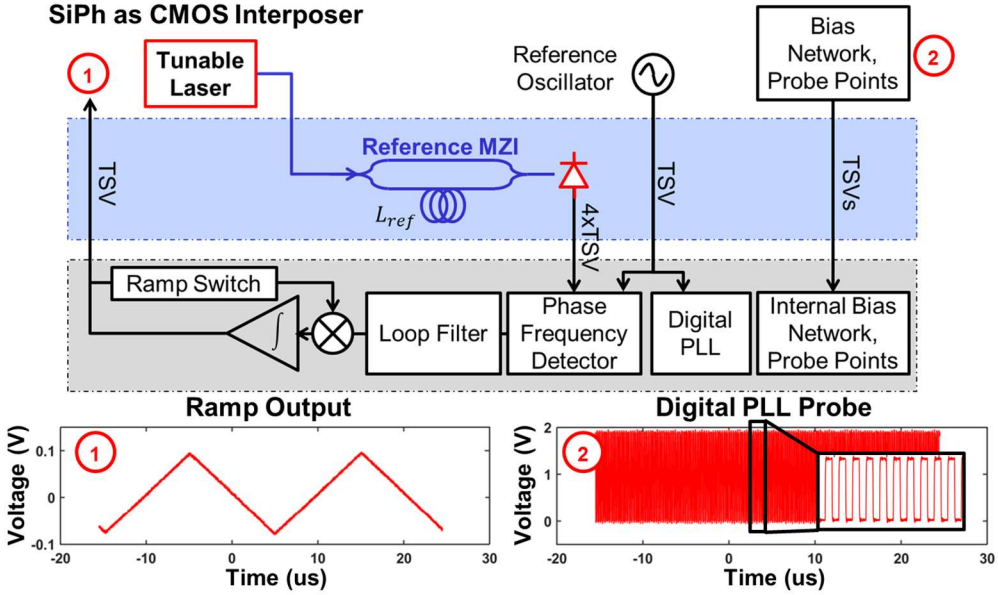

Fig. 3-22. Bonded stack configuration for verification of silicon photonics as an electrical interposer for CMOS. A reference oscillator (clock signal) is connected through SiPh TSV to a digital PLL on the CMOS chip, and ramp output is observed ((1) on the figure, labeled "Ramp Output") and digital PLL output is observed ((2) on the figure, labeled "Digital PLL Probe"). Output of the ramp signal indicates proper bias networks for the ramp generator, ramp switch, ramp output, and digital PLL output indicates proper digital bias networks.

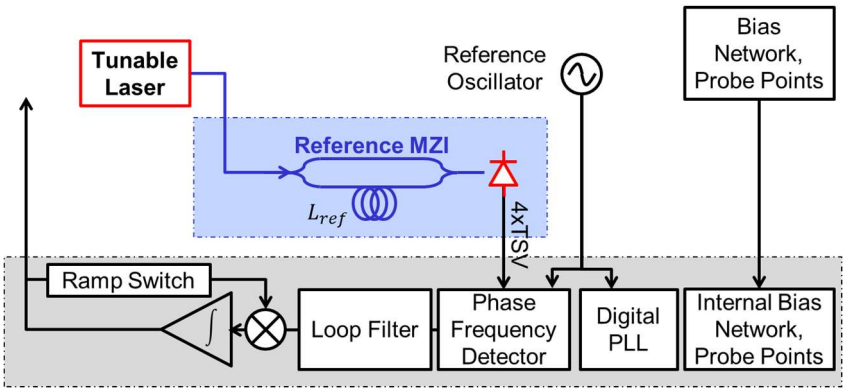

Fig. 3-23. Edge-diced chip testing configuration. A fully-functional OPLL system is constructed with the only required TSV connections at the MZI photodiode output. All other bond-pads are directly wirebonded from CMOS to the daughter-board.

3.3.5 OPLL Parameter Selection

The type-II PLL has a maximum stable bandwidth which is limited primarily by the off-chip path delay of 20ns (due to fiber pigtail lengths for off-chip components). This results in a maximum stable bandwidth of ~1MHz. This limits the maximum modulation frequency to ~100KHz, in order to resolve sharp ramp switching corners for laser modulation. The laser chosen for implementation at the chip-scale has 120GHz excursion, and the silicon photonics MZI used has a delay of 330ps. This indicates that the local oscillator frequency needed to match the beat frequency of this laser/MZI combination is ~8MHz. These parameter values fluctuate with laser conditions, so the values written here are only approximate, and don't necessarily represent exact values used in the successful experiment.

3.3.6 Experimental Results: Open-Loop vs. Closed-Loop Operation

In this section, we report the performance of the integrated OPLL in FMCW configuration. Fig. 3-24 illustrates the block diagram of ranging experiments using the integrated OPLL. Fig. 3-25 shows a photo of the ranging setup used to obtain range-precision measurements and 3D images.

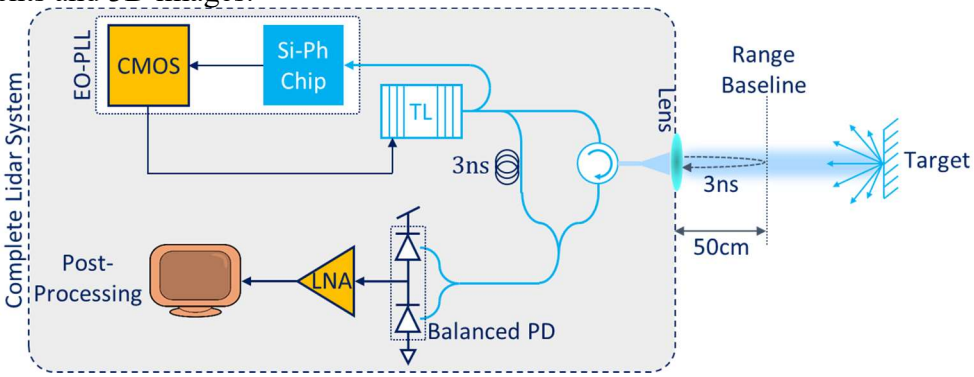

Fig. 3-24: Block diagram of ranging experiments using integrated OPLL. Optical taps and single-mode fiber are used to emulate a lidar receiver.

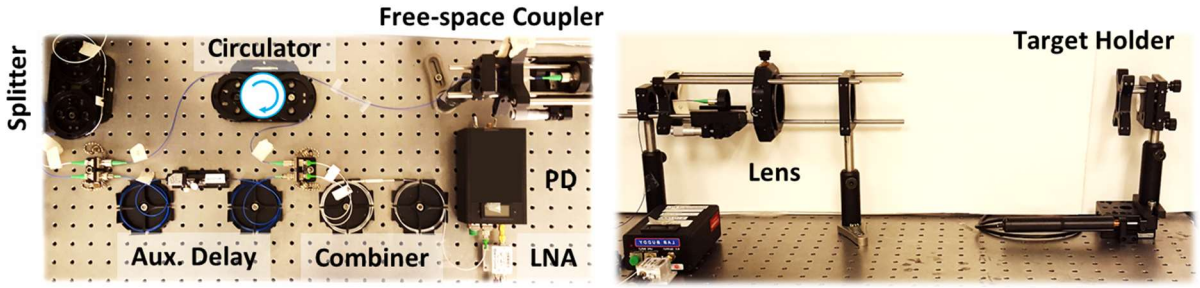

Fig. 3-25: Photograph of free-space ranging setup. The optical chirp is focused onto a target at arbitrary standoff distances, and the target position is stepped to emulate single-beam rastering.

Under closed-loop configuration, the optical chirp is considered linear with chirp-rate, gamma. With a target that creates the long arm of an interferometer, the measured beat frequency at the output of the interferometer is proportional to the round-trip target distance (with some offset). We know gamma by design, so we can calculate absolute target distance simply by measuring target frequency.

We employ a post-processing method to obtain a frequency measurement for use in range acquisition. First, zero-crossing measurements of the sinusoidal trace are performed. Second, we find the average of all zero-crossing measurements for a single up- or down-ramp to obtain a single-ramp beat frequency estimate. We measure the accuracy of this estimate by calculating its standard deviation over many ramp periods. In order to achieve high range resolution, it is desired to average beat frequency estimates over several ramps, which contributes to acquisition time for a single pixel.

Several artifacts can have effects on these final beat frequency estimate, including optical chirp settling time, chirp slope inaccuracy (offsets in gamma from designed value), and chirp non-linearity (deviation of gamma from constant). We expect the ranging precision of the lidar system to scale with the locking precision of the OPLL, thus we expect to see improved lidar performance with closed-loop configuration over open-loop configuration.

We can perform several measurements regarding range precision using our system. In simple precision verification experiments, we can displace a cooperative target with micrometer accuracy, measuring target beat frequency for many successive ramps. For example, Fig. 3-26 shows the target beat frequency for a target that is stepped with 200um increments. It is important to perform this experiment at several ranges in order to determine the phase noise-limited range of the system, since there is a tradeoff between range and range accuracy for FMCW systems. We perform these measurements at 5cm, 30cm, and 70cm range, illustrating two results: first, improvement of closed-loop ranging accuracy over open-loop accuracy; and second, a very high ranging precision of 4.4um at 5cm. These results are shown in Fig. 3-27.

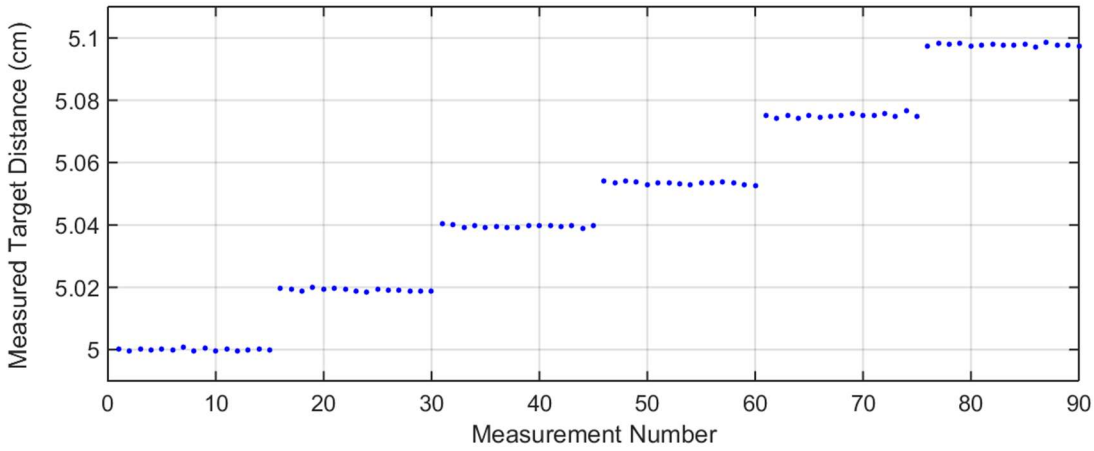

Fig. 3-26: Average beat frequency per ramp over successive ramps, with target displacement at increments of 200 um. Target distance from baseline ~5cm.

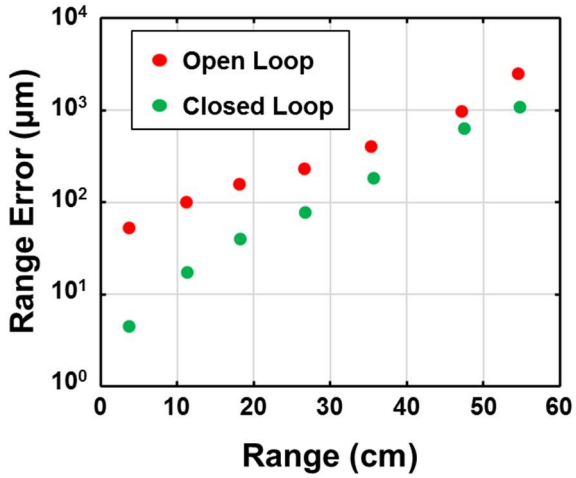

Fig. 3-27: Range precision as a function of range and OPLL condition (open- or closed-loop).

Measurements in FMCW systems can be performed with different "baseline" distances because the interferometer beat frequency is related to the path *difference* between the two arms, and not the absolute length of the target arm. Effects of laser phase-noise are minimized when the path difference between the arms is zero, resulting in precise ranging measurements only limited by target SNR. In our imaging setup, we use a baseline delay of 3ns, equivalent to a 50cm baseline distance in free-space. Therefore, targets present at ~40cm and ~60cm will yield measured distances of 10cm and corresponding range precisions. The actual target distance is calculated after adding the baseline delay to the measured delay.

3.3.7 Experimental Results: Imaging

We demonstrated the use of this system in an imaging configuration, in which we used this system to obtain a three-dimensional image of a small (~1mm thick) gear. This image is shown in Fig. 3-28. The image was taken at ~40cm standoff distance from the lens with 50cm baseline distance, and achieves ~11um precision, limited by the residual phase-noise in the chip-level OPLL. The data in Fig. 3-28 represents data that is post-processed to map range to x-y position. This post-processing step can later be integrated into CMOS or PCB electronics. We

also implemented the Thorlabs GVS001 Galvo Scanning tool with the OPLL in order to demonstrate imaging for metrological applications, such as the 3D images of fine features on a US Quarter, shown in Fig. 3-29.

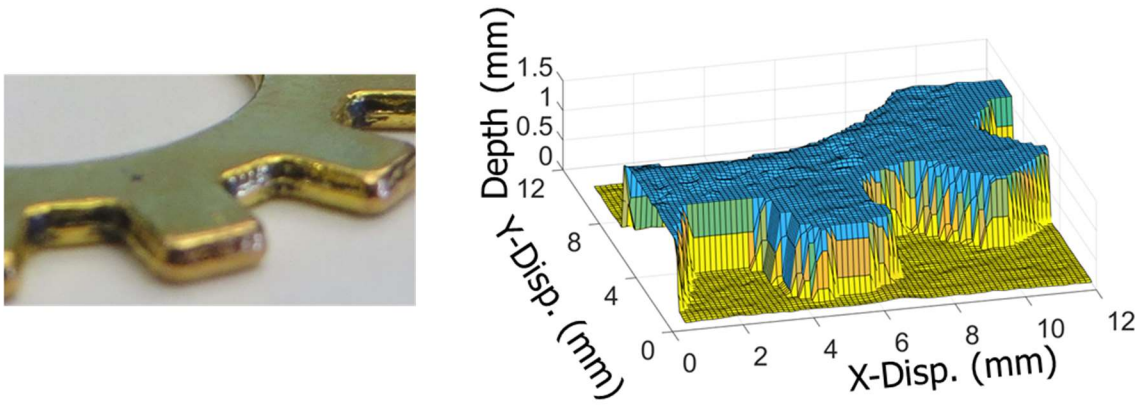

Fig. 3-28: Photograph of 1.1mm thick gear (left) and a 3D image of a gear (right) with 1.1mm thickness placed at 40cm distance from the imager taken with chip-level OPLL.

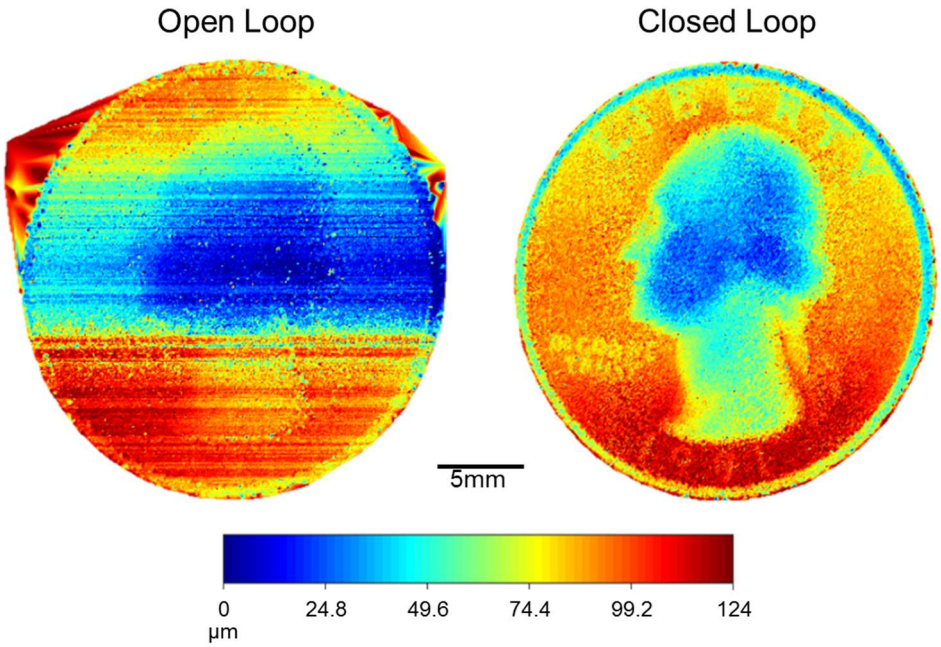

Fig. 3-29. FMCW 3D images of a US quarter for open-loop OPLL (Left) and closed-loop OPLL (right).

4 Wide-Range Non-Linear FMCW Lidar

In this chapter, I will explain in detail the "k-clock" method for range measurement, in which a non-linear FMCW signal is resampled in order to make it linear. I will show several modifications and improvements to the k-clock method, first to increase the speed with which measurements can be made, and second, to increase the phase-noise-limited range of non-linear FMCW signals. The improvements are justified with analytical, numerical, and experimental arguments. The resampling methods presented here represent a possible implementation for high-resolution imagers using cost-effective components.

4.1 Principles of Non-Linear FMCW Lidar

In previous sections, we have usually assumed that the tunable laser chirp is required to be a linear chirp, as shown in Fig. 4-1a), leading to a constant beat frequency which is observable by Fourier transform, as shown in Fig. 4-1c). However, in many cases, the linear ramp is difficult or impossible to create. For example, if a laser is modulated at its band limit, a triangular waveform will have its highest harmonics attenuated, so that the laser chirp is close to sinusoidal in shape, as shown in Fig. 4-1d). Depending on the degree of non-linearity introduced into the chirp, the frequency can be broadened significantly, as shown in Fig. 4-1f), so that a simple peak-finding algorithm cannot be used to determine target depth. The goal of a resampling algorithm is to measure and correct for the non-linearity by measuring its effect in a fixed reference interferometer. This can manifest in a hardware solution, in which the target signal is directly sampled at a non-uniform rate, or in a software solution, in which the target signal is interpolated at non-uniformly distributed points after it is recorded by an ADC. In this chapter, we will discuss the latter, in which we use a software implementation to resample the target signal in post-processing.

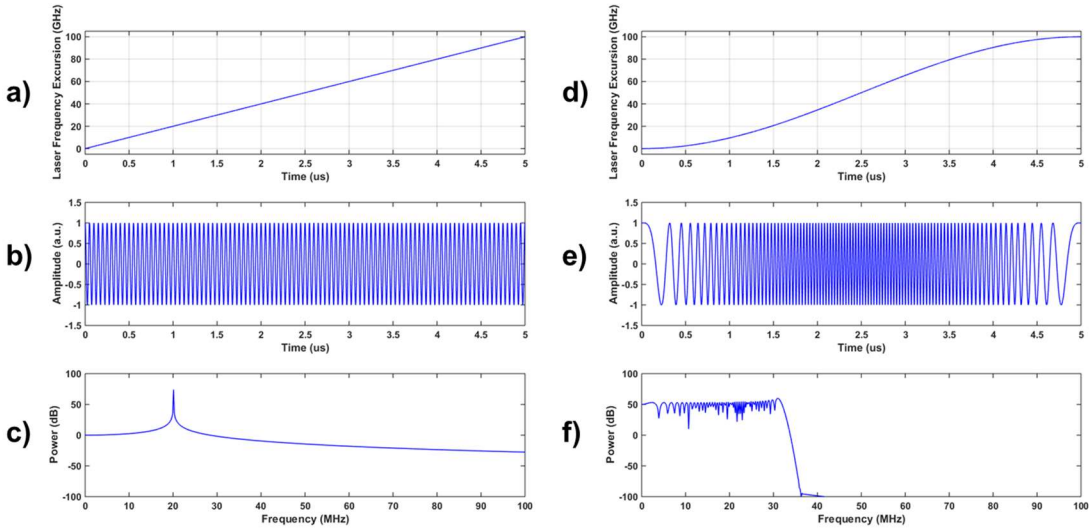

Fig. 4-1. Linear vs Non-linear laser chirp for FMCW Lidar a) laser frequency excursion for a linearly chirped laser (nominal); b) beat frequency with linear chirp through an MZI; c) discrete Fourier transform of the beat in b); d) laser frequency excursion for a sinusoidally chirped laser (non-ideal); e) beat frequency with sinusoidal chirp through an MZI; f) discrete Fourier transform of the beat in e).

4.2 Resampling Experimental Design

We implemented a ranging system composed of a thermally-tunable VCSEL, one fiber interferometer (the reference interferometer), and one fiber/free-space interferometer with focusing optics and scanning mirrors (the target interferometer), see Fig. 4-2. We report three particular configurations of an FMCW lidar sensor with various reference lengths, modulation rates, and acquisition limitations, as summarized in Table 4-1.

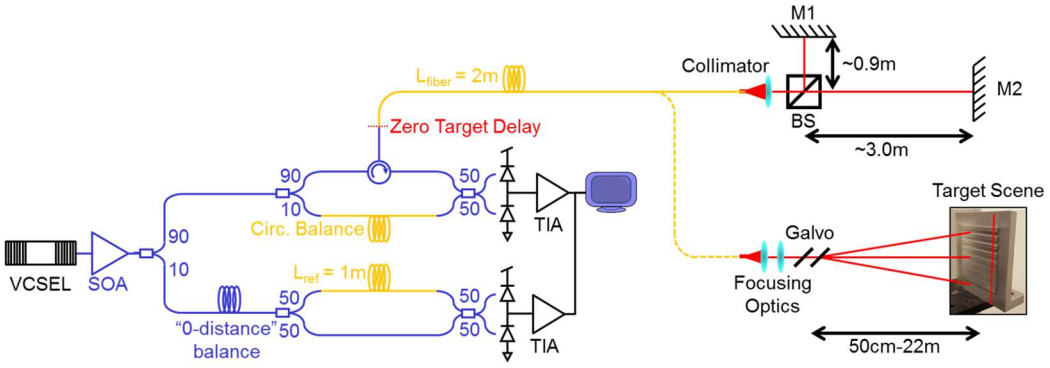

Fig. 4-2. Imaging system configuration with reference interferometer and two target configurations: (top) multi-target measurement setup, (bottom) scene measurement setup. VCSEL refers to the tunable laser; SOA refers to an optical amplifier; split ratios are noted as percentages; "Circ. Balance" refers to a length of fiber used to balance the delay of the circulator so that the end-facet of the circulator gives a target delay close to 0-seconds; "0-distance balance" refers to a length of fiber used to match delays between the target interferometer and reference interferometer; "L_{fiber}" and "L_{ref}" can be adjusted for different experimental configurations; TIA refers to the electronic amplifiers in the same package of the balanced photodiodes; BS represents a 50:50 prism beam splitter.

We use Configuration 1 to demonstrate an imaging system that approaches practical frame rates for fast 3D imaging. The frame rates are limited by the speed of the particular scanning tool used in the demonstration. We use Configuration 2 to demonstrate the performance of standard k-clock resampling at high laser modulation rates, and to justify the need for MK-resampling. We use Configuration 3 to justify using a long-distance reference interferometer in MK-resampling in order to extend the phase noise limited range.

We chose these configurations to confine target beat frequencies within the sampling rates of available ADCs in our lab; they do not represent fundamental limitations of the methods presented herein. With these configurations, we demonstrate an application ranges an order of magnitude longer than that demonstrated by [17,18], but with a more modest resolution, for application in manufacturing or robotic navigation. Demonstration of our system with a thermally-tunable VCSEL without active feedback control illustrates the potential of a low-cost solution for high-precision lidar, leading FMCW technology towards ubiquitous consumer applications.

Table 4-1 Experimental Configurations for Wide-Range Non-Linear FMCW Lidar

Parameter	Configuration 1 Demonstration Platform (limited by ADC sampling rate)	Configuration 2 Fast Resampling (limited by phase noise)	Configuration 3 Phase Noise Limit Extension (limited by phase noise)
Laser Modulation Depth (Fourier Resolution)	412 GHz (364 um)	47 GHz (3.2mm)	47 GHz (3.2mm)
Laser Modulation Rate	4 KHz	100 KHz	5 KHz

Reference Length (physical length of SMF-28 optical fiber)	1-meter	1-meter	30-meter
Target Distance (one-way)	0-1.4 meter	0-2 meters (standard k-clock resampling) 0-6.5 meters (MK resampling)	0-21 meter (MK resampling)
ADC Sampling Rate	100 MS/s	5 GS/s	250 MS/s
ADC-Limited Maximum Range	1.45 meter	25.4 meter	31.7 meter

We configured the target interferometer using a fiber circulator, which guides light from input 1 to output 2, and light from input 2 to output 3. This allows light to be transmitted out of and received into the same single-mode fiber. We chose to balance the path length delay of the circulator with a matched length of fiber on the other arm of the interferometer, to remove this path length distance from the measurement before signal-processing (referred to as "Circ. Balance" in Fig. 4-2).

In order to ensure that a target chirp was synchronized with the reference chirp corresponding to an identical delay, we included a balance fiber before the reference interferometer. This ensures that if the target interferometer has a path delay difference that exactly matches the reference path delay difference, the chirps will be synchronized before post-processing. This does not have to be true in general, since this delay can be compensated for in post-processing, but maintaining this balance minimizes the complexity of signal processing.

We configured the free-space section of the target interferometer for multiple experiments. First, as shown in the top right of Fig. 4-2, we constructed a multi-target single point measurement with a 50:50 beam splitter and two mirrors with different path length delays. Second, as shown in the bottom right of Fig. 4-2, free-space optics were mounted with a stepper motor-actuated pair of scanning mirrors, in order to obtain 1D images ("line-scans") and 2D images ("image scans").

4.3 Resampling as a Method to Ensure Linearity in Signal-Processing

We will first construct a mathematical model of the standard "k-clock" resampling method and analyze the deterministic error of such a resampling method. We will refer to this method as "k-clock resampling." We will then introduce "multi-k-clock" resampling in order to remove deterministic error due to target signal delay. Fig. 4-3a) shows the block-diagram of a typical software k-clock resampling implementation. The method of multi-k-clock resampling presented here is similar to the method presented in [18], in which an optimization method is used to determine an appropriate non-linear transform. In this dissertation, the method we describe is based on an assumption of sinusoidal frequency tuning, and is therefore deterministic in its formulation.

We implement k-clock resampling as follows. First, the phase of the recorded reference beat is extracted by Hilbert transform, as shown in [44]. An interpolation of the reference phase at uniformly-spaced phase steps yields new resampling times, $t_r[m]$. These resampling times are used to interpolate the time-domain target signal. A Fourier transform of the resampled target signal yields a spectrum that can be used to estimate the distance of the target relative to the reference. First, we will analyze the error in this measurement for sinusoidal laser frequency chirps, and secondly, we will show the reduction of the error in sinusoidal laser frequency chirps by adding delay. We call the method of error reduction "multi-k-clock (MK) resampling," which is outlined

in the block diagram in Fig. 4-3b. In the case of MK resampling, the target signal is resampled several times after application of a delay bank.

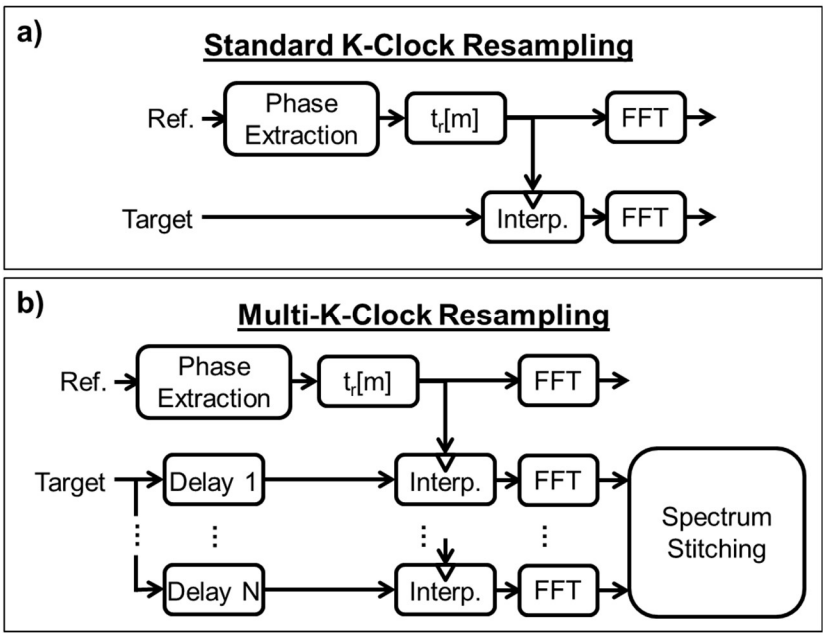

Fig. 4-3. Block diagrams of resampling architectures: a) k-clock resampling in software: phase of the reference signal is measured using a Hilbert transform, new non-uniform time samples are used to interpolate the target signal before spectral analysis with FFT; b) "multi-k-clock" resampling: the target signal is delayed before resampling in order to compensate for desynchronization between the reference and target signals, and different pieces of the spectrum are stitched together to form a complete spectrum.

4.3.1 Resampling Analysis with Delay-Matched Clock and Target

In general, the reference beat photocurrent signal is proportional to a cosine with a phase argument, as in Eq. (4.1):

$$I_{PD}(t) \propto \cos\left(\Delta\phi\left(t,\tau_{ref}\right)\right) \tag{4.1}$$

The phase argument, $\Delta\phi\left(t,\tau_{ref}\right)$, represents the photocurrent's dependence on the shape of the laser frequency chirp and the path length delay of the reference interferometer, τ_{ref}. In the case of sinusoidal laser frequency tuning, the photocurrent phase can be written as a sum of sines:

$$\Delta\phi\left(t,\tau_{ref}\right) = \frac{\Delta f_{laser}}{f_{mod}}\left[\sin\left(2\pi f_{mod} t\right) - \sin\left(2\pi f_{mod}\left(t-\tau_{ref}\right)\right)\right] + 2\pi f_0 \tau_{ref} \tag{4.2}$$

where Δf_{laser} is the total laser frequency excursion, f_{mod} is the modulation frequency of the laser chirp, and f_0 is the initial laser frequency. With uniform sampling, we create discrete-time signal by replacing t with nT_s. If we were to take a discrete Fourier transform (DFT) over discrete-time variable n, we would not recover a range spectrum.

Instead, we can sample the signal with non-uniformly space samples, $t_r[m]$, where the samples are chosen such that the non-uniformly sampled phase is linear over the new discrete-time variable, m. This would require $\Delta\phi\left(t_r[m],\tau_{ref}\right) = am + b$. With linear phase, the DFT over m would

create a spectrum where each bin corresponds to a possible target distance. We can write the new phase (and change using a trigonometric identity):

$$\Delta\phi\left(t_r\left[m\right],\tau_{ref}\right)=\frac{\Delta f_{laser}}{f_{mod}}2\left[\cos\left(2\pi f_{mod}\left(t_r\left[m\right]-\frac{\tau_{ref}}{2}\right)\right)\sin\left(\pi f_{mod}\tau_{ref}\right)\right] \\ +2\pi f_0\tau_{ref} \tag{4.3}$$

If we want $\Delta\phi\left(t_r\left[m\right],\tau_{ref}\right)=am+b$ (linear phase), we would choose

$$t_r\left[m\right]=\frac{\arccos\left(cm\right)}{2\pi f_{mod}}+\frac{\tau_{ref}}{2}+t_{offset} \tag{4.4}$$

where *c* is a fixed parameter chosen so that *cm* is in the principal domain of arccosine. This formulation gives us expressions for *a* and *b*: $a=\left(\Delta f_{laser}/f_{mod}\right)2c\sin\left(\pi f_{mod}\tau_{ref}\right)$; $b=2\pi f_0\tau_{ref}$. Our ultimate goal is to choose resampling times $t_r[m]$ to resample some arbitrary target signal. Consider the resampled *target* signal phase, $\Delta\phi\left(t_r\left[m\right],\tau_{targ}\right)$, where we have made the change of τ_{ref} to τ_{targ}. We can show that $\Delta\phi\left[m,\tau_{targ}\right]=a'm+b'+e\left[m\right]$, where *a*`and *b*` are constant over *m*, but *e*[*m*] is an error term that depends on *m* and the difference between target and reference path lengths, $\Delta\tau=\tau_{ref}-\tau_{targ}$. The error term for a sinusoidal signal is given:

$$e\left[m\right]=\frac{\Delta f_{laser}}{f_{mod}}2\sin\left(\pi f_{mod}\tau_{targ}\right)\cdot\left(-\sqrt{1-\left(cm\right)^2}\right)\cdot\sin\left(2\pi f_{mod}\frac{\Delta\tau+2t_{offset}}{2}\right) \tag{4.5}$$

Since the DFT is taken over m, we can see that the significance of the error term grows as $\Delta\tau+2t_{offset}$ increases from 0. This has the effect of blurring target beat signals with τ_{targ} greater than τ_{ref}. We can use t_{offset} to "re-focus" the DFT spectrum at a particular distance. We must choose t_{offset} such that the argument of the second sine term in *e*[*m*] is close to 0. In this case of sinusoidal tuning, we would choose:

$$t_{offset}=\frac{\tau_{targ}-\tau_{ref}}{2} \tag{4.6}$$

Since this t_{offset} depends on τ_{targ}, the offset corresponds to a particular bin, *k*, in the DFT of the resampled data:

$$k=\frac{\Delta f_{laser}}{f_{mod}}cM\sin\left(\pi f_{mod}\left(2t_{offset}+\tau_{ref}\right)\right)\approx\Delta f_{laser}cM\left(2t_{offset}+\tau_{ref}\right) \tag{4.7}$$

where *M* is the total number of data points after resampling. This corresponds to a beat frequency (in Hz),

$$f_{beat,k}\approx\overline{\gamma}\left(cM\right)\left(2t_{offset}+\tau_{ref}\right) \tag{4.8}$$

This reveals an expression for beat frequency similar to that of a linear chirp, where we note that $\overline{\gamma}$ represents the "average chirp slope."

Eq. (4.5) reveals several important parameters for sinusoidal resampling error. First, the error in phase grows approximately linearly with modulation frequency, for modest-length targets where the small-angle approximation holds. Secondly, the error in phase also grows with target interferometer delay difference. Also of note is eq. (4.7), which relates the DFT index of a "synchronously" resampled signal to the offset time required to resolve targets in that bin. Note

that these relationships are derived for a sinusoidally-modulated laser, but a similar approach could be applied to derive single-k-clock resampling error for other arbitrary tuning patterns.

The phase-error term in eq. (4.5) can be assessed in terms of its effects on the DFT of the target signal after resampling. The Fourier-limited resolution of a target at a specified distance is calculated as a function of f_{mod} and Δf_{laser}, through DFT analysis of a chirp exhibiting the error term of Eq. (4.5). In reality, the chirp exhibited by the laser deviates from a sinusoid, thus the error term exhibited in experiment deviates from that described by Eq. (4.5).

4.3.2 Multi-K-Clock (MK) Resampling Architecture Description

The analysis performed above shows that we can select offset times that eliminate the phase error term entirely. Eq. (4.6) shows that the offset time is directly related to the target distance. Since the DFT bin is directly related to the target distance, we can use this offset time to deterministically "re-focus" the target signal for a particular distance. This offset time effectively synchronizes the target chirp with the reference chirp, thus we call the offset time a "synchronization delay." By introducing a bank of synchronization delays before resampling, we can implement the "multi-k-clock" (MK) resampling scheme, in which each delay corresponds to a re-focused area of the DFT spectrum. This is outlined by the block diagram in Fig. 4-3b. After resampling each delayed target signal, we stitch the corresponding windows of the DFT together to form the MK distance spectrum.

We analyze the effect of standard k-clock and MK resampling by performing the DFT of the analytical expression for photocurrent after resampling and doing peak analysis of the results. Fig. 4-4a) shows an example of this numerical study for a target beat frequency resolved at 600MHz. The effect of the error term in standard k-clock resampling evidently changes the peak behavior for this beat signal, while MK resampling removes the effect of the error term. We show analytical results for signal power, range error, and FWHM for a bank of eight, equally-time-spaced synchronization delays in Fig. 4-4b-d). The number and spacing of the delays could be selected based on application specification.

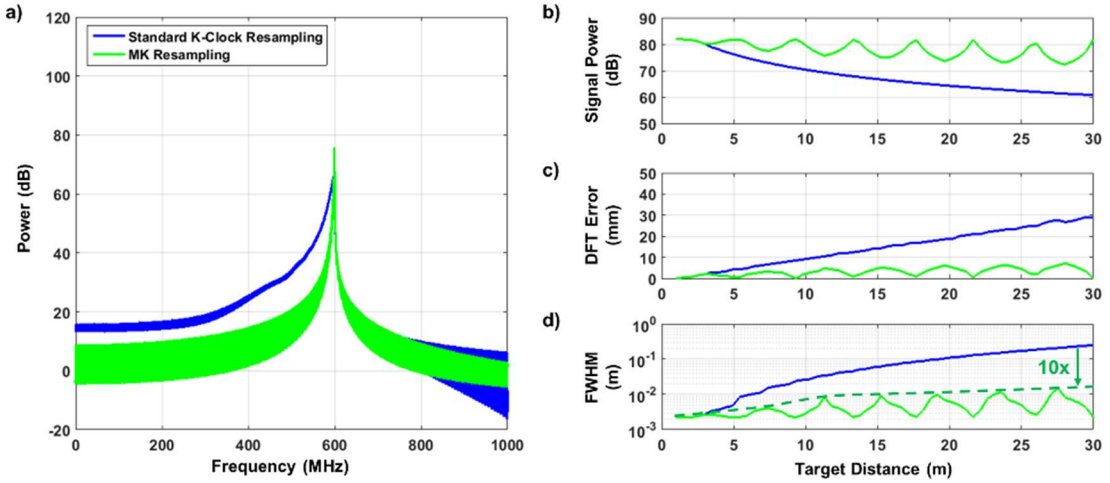

Fig. 4-4 Numerical analysis of standard k-clock and multi-k-clock resampling algorithms; a) power spectral density result for standard k-clock resampling (blue) and multi-k-clock resampling (green); b-d) DFT peak analysis for targets resampled using the standard k-clcok algorithm and the multi-k-clock method.

4.3.3 Experimental Characterization of Standard K-Clock and MK Resampling Methods

We implemented the standard k-clock resampling algorithm using custom LabVIEW software. The following protocol is followed in order to make a range measurement for use in a raster-scanned image: 1) perform Hilbert transform on reference beat signal to extract reference beat phase; 2) interpolate time axis to obtain samples where the reference phase is uniformly spaced; 3) interpolate target beat signal at new re-sampled times; 4) perform FFT on target beat signal; 5) find peaks in resampled target beat spectrum by windowing and thresholding. The architecture of method is illustrated in Fig. 4-3)b. An example of the results of each step are presented in Fig. 4-5)a-h.

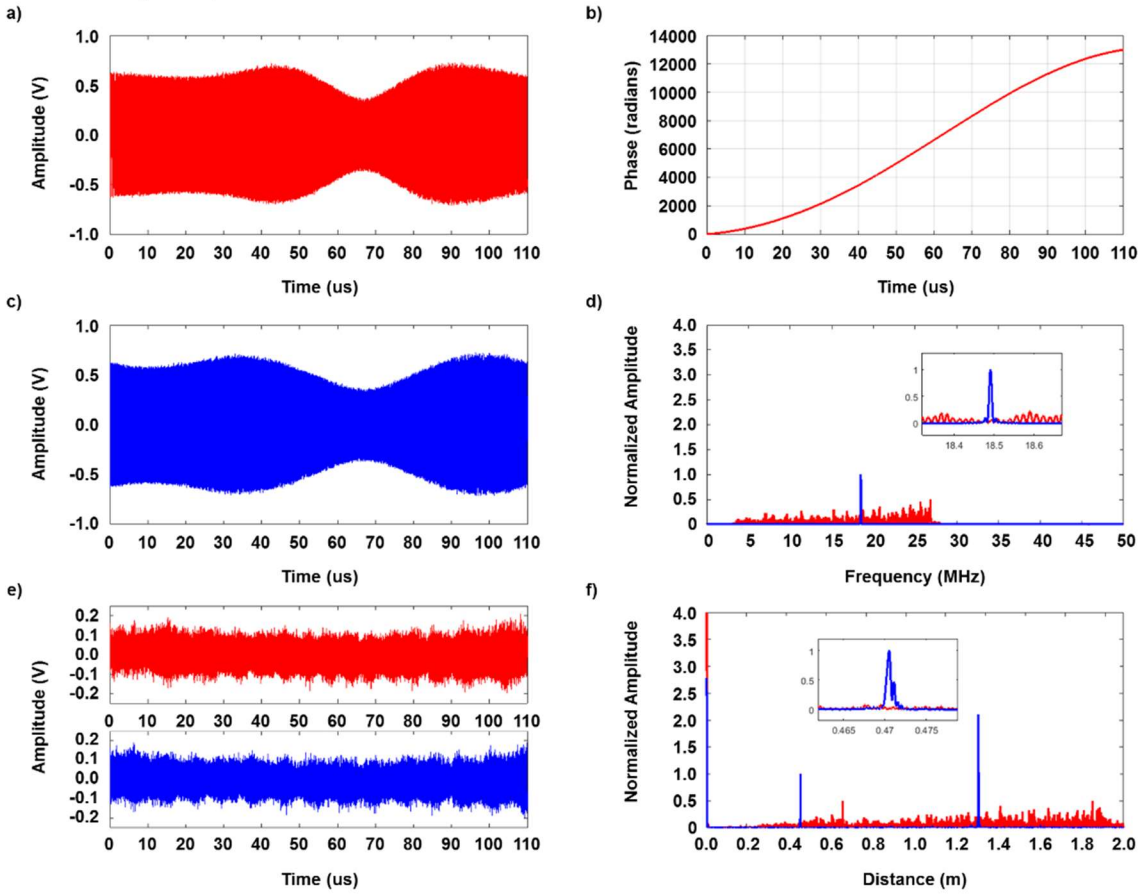

Fig. 4-5. Standard k-clock resampling processing. a) measured time-domain reference signal (red); b) phase of reference signal as measured by Hilbert transform; c) time-domain resampled reference signal (blue); d) PSD of non-linear and resampled reference signals; d) (inset) zoom on the resampled PSD to show Fourier-limited resolution; e) time-domain target signal (red) and resampled target signal (blue); f) PSD of non-linear and resampled target signals; note that there are two reflections in this measurement, which are both resolved after resampling; g) (inset) zoom on the resampled PSD to show Fourier-limited resolution for the target signal.

To characterize the performance of the standard k-clock system, we used Configuration 1 from Table 4-1, in which we use a modest modulation rate of 4KHz and a reference length of 1-meter. Image scanning is achieved using a stepper-motor-actuated 2D galvanometer scanning tool from Thorlabs, with a point-to-point small angle step response of 400us. Data acquisition is performed with the NI PXIe-5122 Digitizer with 100MS/s sampling rate and 14-bit ADC resolution, and transferred over the NI PXIe-8360 bus, and the resampling algorithm is performed

in a custom designed LabVIEW application, compiled onto an Intel Core I7-3520M CPU with 2.90GHz clock speed. Data acquisition speed is limited by the mirror step response, while the data processing speed is limited by the particular implementation of the LabVIEW application.

With the current implementation, a 200x200 pixel frame can be acquired in 20 seconds, and processed in ~100 seconds with the standard k-clock algorithm. This demonstrates a path towards video frame rates, so we demonstrate scanning objects of interest such as full faces, hands, and other handheld objects.

We characterized Configuration 1 by imaging the "resolution block" shown in Fig. 4-6a,b). The measurement of the block is rendered in Fig. 4-6c), in which we observe steps as small as the 13th step, corresponding to a single-target precision of 30 microns (one-way). Images can be acquired and rendered using this configuration, and several examples are illustrated in Fig. 4-7. These results emphasize possible applications of the high-resolution system for use in scene identification, gesture recognition, and facial recognition.

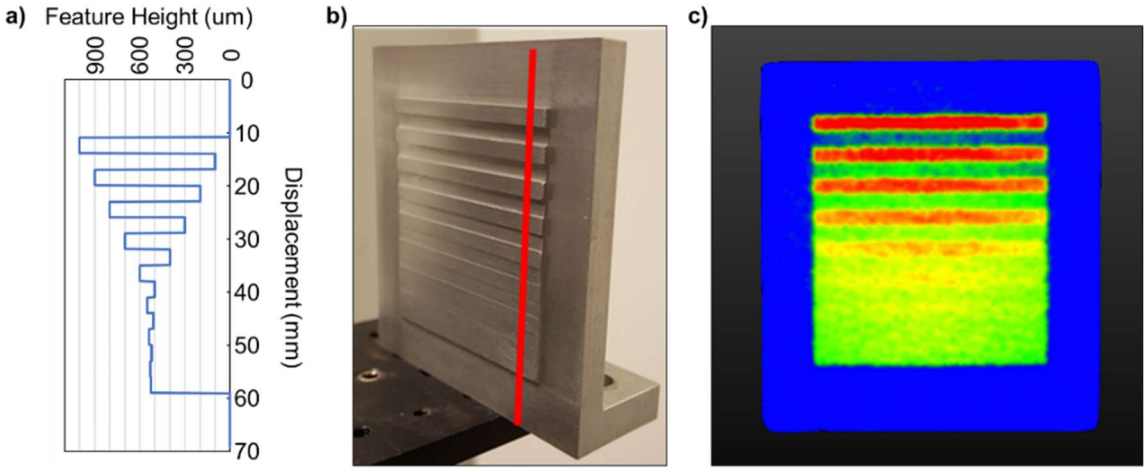

Fig. 4-6. Standard K-clock resampling characterization result; a) machined specification for the resolution block; b) photo of machined resolution block c) resolution block image rendered using Configuration 1 from Table 4-1.

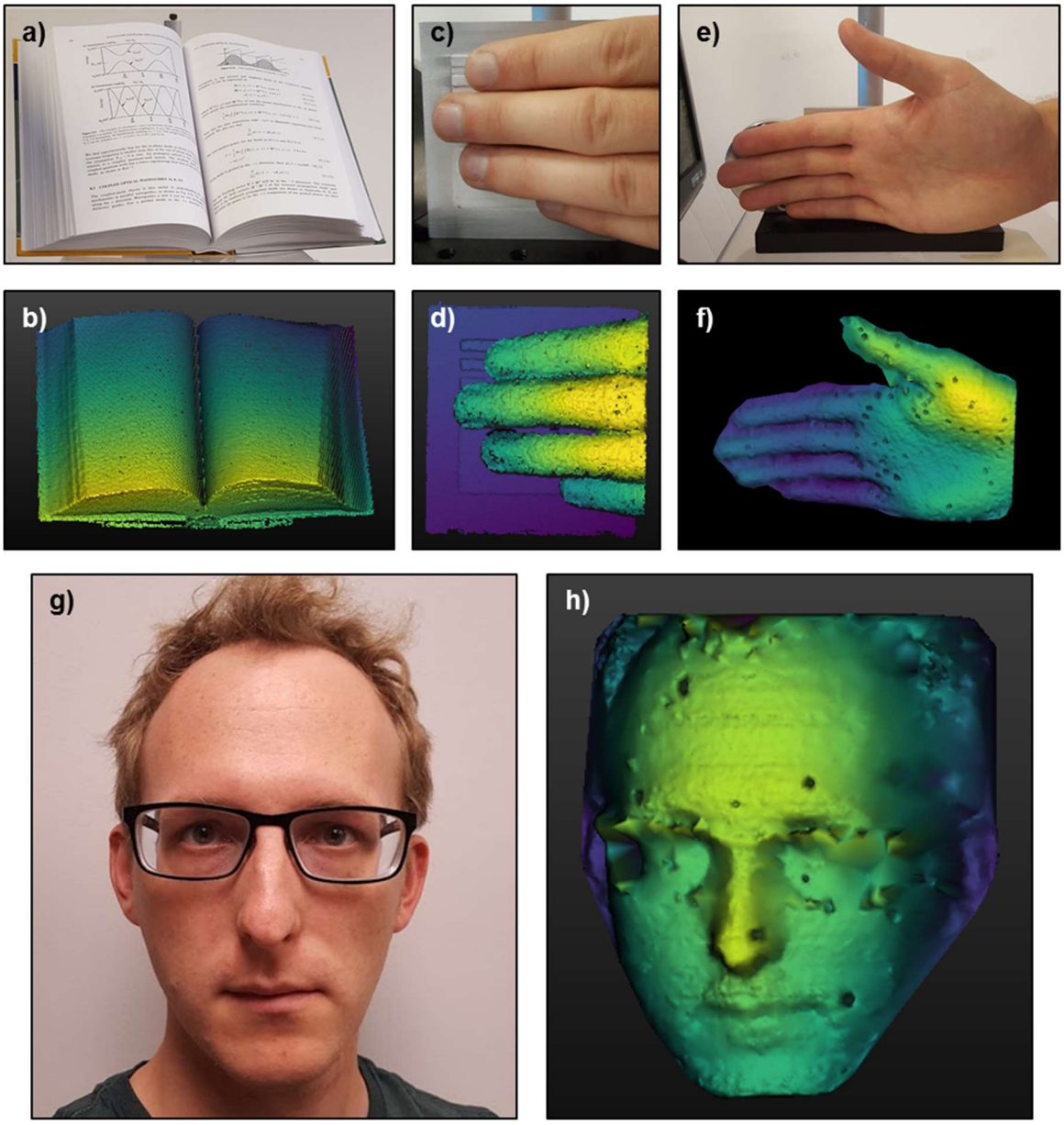

Fig. 4-7. Standard k-clock resampling imaging results. a-b) photograph and 3D rendering of an open textbook; c-d) photograph and 3D rendering of fingers in front of the resolution block; e-f) photograph and 3D rendering of a hand; g-h) photograph and rendering of the author's face. Artifacts in the rendering are the result of mesh conditioning parameters, and can be post-processed to infer surfaces and other features. Note that the rendering of the face includes artifacts from glasses, including effects of lens refraction, which are not compensated for in the rendering software.

We implemented a multi-k-clock resampling method using optical Configuration 2, with a bank of delayed resamplers implemented in software. Since the MK resampling analysis outlined in Fig. 4-3b) requires a delay before resampling, each element in the bank performs the following operations: 1) delay the uniformly-sampled target signal; 2) re-sample by interpolation of the target signal at the reference resample-times; 3) perform FFT, keeping FFT result in vicinity of the k^{th} bin (where k is given by eq. (4.7), and corresponds to the delay from Step 1). Data acquisition is performed with a digital oscilloscope, and, as a proof-of-concept, the resampling bank is implemented in post-processing software.

For our ranging experiment, we observe two targets simultaneously that are several meters apart in order to illustrate the need for MK resampling over a broad range. A beam splitter directed the optical chirp to targets at ~3.9m and ~6m ranges. We used a 1550nm commercially available distributed Bragg reflector (DBR) thermally tunable VCSEL laser with a 100kHz modulation frequency and an optical frequency excursion of 25 GHz. The process of delay/re-sample/FFT is performed over ~20 meters in range with bank windows of ~0.42m. In the spectrum shown in Fig. 4-8a), the targets appear approximately 2 meters apart. The re-sampled spectrum with standard k-clock resampling is shown in Fig. 4-8a), and the re-sampled spectrum with multi-k-clock resampling is shown in Fig. 4-8d). The MK-resampled spectral result in Fig. 4-8d) shows that we can approach Fourier-limited resolution of 6mm from a 25GHz excursion.

A statistical study in which we measured the locations of target peaks for standard k-clock and multi-k-clock resampling spectra shows a systematic improvement in the precision of this system at longer distances. Fig. 4-8 (b,c,e,f) show the distribution of measurements for the 3.9m and 6m targets over 200 successive range measurements for the standard k-clock and multi-k-clock resampling methods. Measurement standard deviation improves from 7.5mm without MK-resampling to 0.23mm with MK-resampling at 3.9m, and improves from 27.9mm without MK-resampling to 0.42mm with MK-resampling at 6m. The measurements assume that there is at most a single target in each range bin. Fig. 4-9 shows results of this experimental analysis performed at several target distances, demonstrating resolution improvement by using MK-resampling.

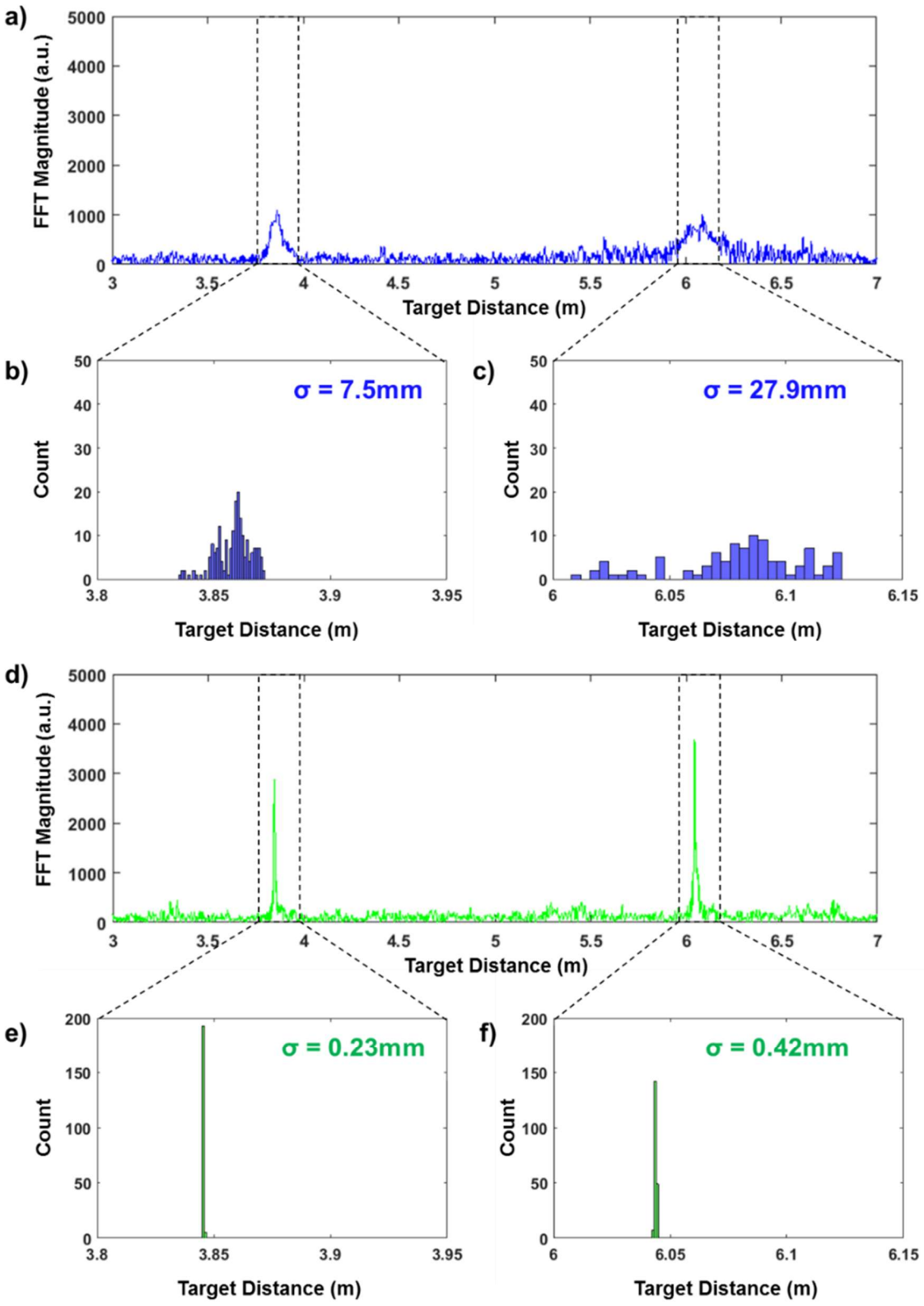

Fig. 4-8. Experimental analysis of standard k-clock and multi-k-clock resampling algorithms; a) power spectral density result for standard k-clock resampling (blue); b-c) DFT peak analysis for targets resampled using the standard k-clock method; d) PSD result for MK-resampling of same data (green); e-f) DFT peak analysis for targets resampled using the MK-resampling method.

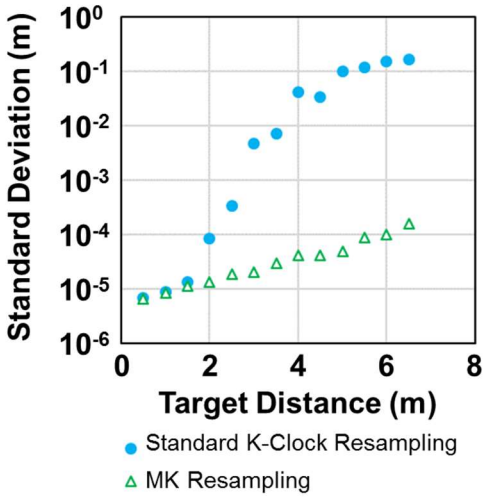

Fig. 4-9. Experimentally determined resolution of standard k-clock and MK-resampling methods as a function of range. MK-resampling improves resolution in the 6-meter range from 10s of cm to sub-millimeter. Target distance is in terms of free-space distance with retro-reflector. Use of a retroreflector isolates the results from free-space loss effects, which would need to be considered in a real lidar sensor.

With the measurement system in place, we used a stepper-motor-actuated 2D galvanometer scanning tool from Thorlabs to raster scan objects in a long working distance. We performed several image scans in order to demonstrate the effectiveness of the multi-k-clock resampling method for 3D imaging. In the following imaging experiments, the target of a resolution block with a "Cal" keychain was placed at 0.5m and 6.5m. Fig. 4-10a) shows a photograph of the target objects. Fig. 4-10b) shows the reference and target interferometer configurations for this experiment. Due to the short frequency excursion of 47GHz, we neglected the effects of dispersion and did not implement any dispersion correction.

Fig. 4-10c) and d) show 3D scanning results for standard k-clock resampling at 0.5m and 6.5m, respectively. Colors in Fig. 4-10c) are mapped to range, while colors in Fig. 4-10d) are mapped to intensity. The inset of Fig. 4-10d) shows a side view of these points, demonstrating that the image contains only noisy data for depth measurement. Fig. 4-10e) and f) show 3D scanning results for MK-resampling of the same data as in the standard k-clocked case. These results show that MK-resampling is required to recover range information at the longer distance for this experimental configuration.

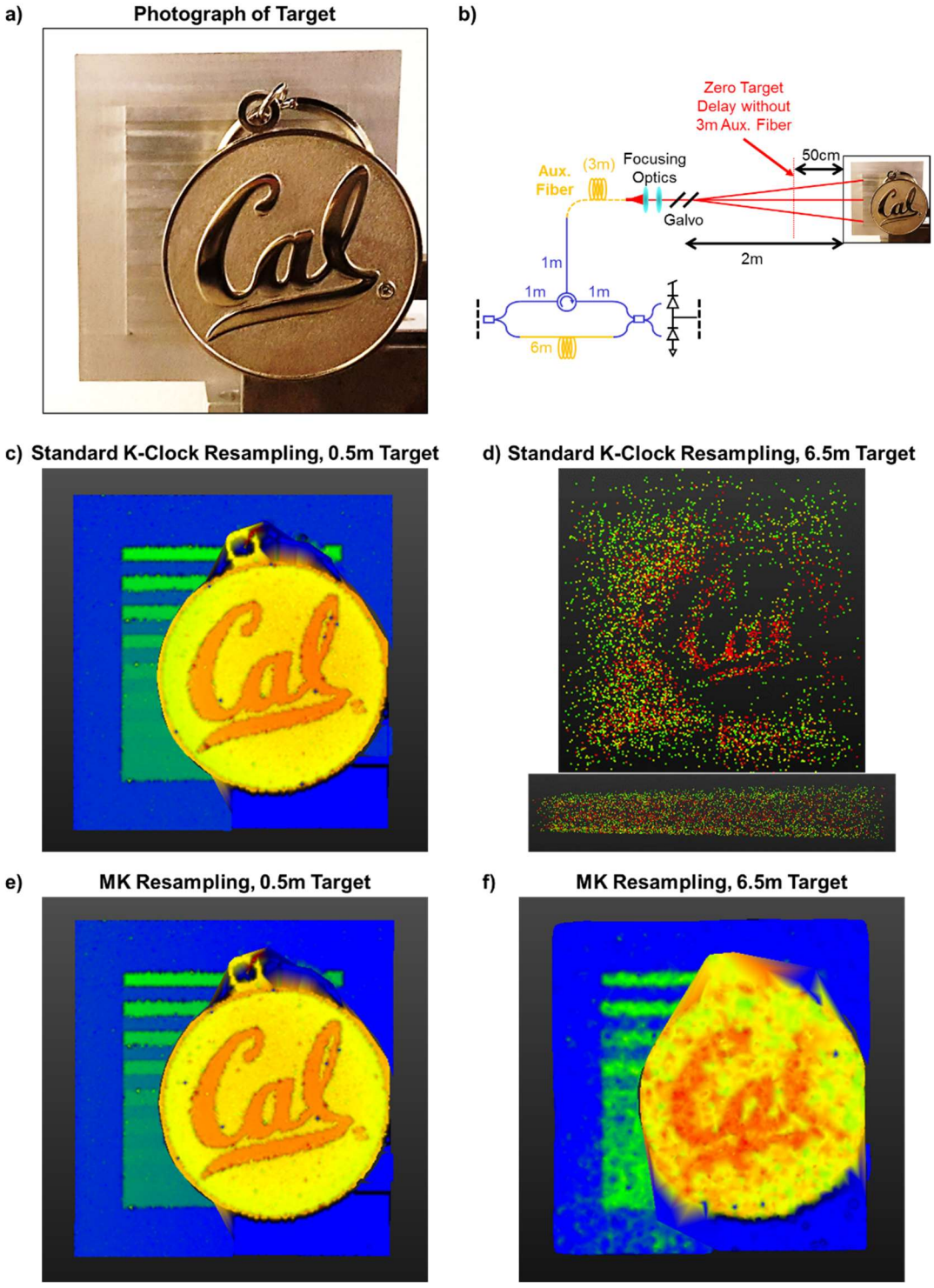

Fig. 4-10. MK-resampling 3D imaging results. a) photograph of target objects for reference; b) setup for imaging target objects: 0.5m targets are measured without the fiber labeled "Aux. Fiber," such that the "zero-target distance is 1.5m from the tx/rx aperture, while 6.5m targets are measured with the 3-meter "Aux. Fiber"; c) meshed 3D image for standard k-clock resampling at 0.5m; d) noisy data with no discernable range for 3D image at 6.5m target distance with standard k-clock resampling; e) meshed 3D image for MK-resampling at 0.5m; f) meshed 3D image for MK-resampling at 6.5m. Without multi-k-clock resampling, targets at the longest distance could not be resolved. Resolving Range Ambiguity with MK Resampling

Asymmetric Mach-Zhender interferometers (MZIs) can exhibit ambiguity in detected range if real-valued time-domain signals are used in signal processing. Intuitively, this means that one cannot distinguish positive and negative target distances from one another. For example, targets at +1-meter will exhibit a DFT symmetric about 0-Hz frequency if the time-domain signal is real, thus an ambiguity in the frequency's sign cannot be resolved without more information.

The range ambiguity problem can be solved by using coherent detection methods, such as I-Q detection [27]. Essentially, this involves construction of a complex time-domain signal in order to induce systematic asymmetry in the DFT analysis of time-domain signals. FMCW detection by Fourier-transform of the time-domain signal is directly related to the FMCW radar method known as "stretch processing," which exhibits range ambiguity when I-Q detection is not utilized. However, the MK-resampling method exhibits properties related to the signed distance of the target relative to the reference interferometer signal. This allows range-ambiguity to be resolved in limited cases without the use of I-Q detection. It should be noted that the capability to resolve this ambiguity degrades as the reference distance approaches zero.

Our approach to resolving ambiguity can be explained by referring back to Eqs. (4.6), (4.7), (4.8). In these equations, we note that the target delay, τ_{targ}, can be signed (positive or negative). Physically, this indicates that the length of the upper arm of the target interferometer is shorter than the length of the lower arm. In order to ensure convenience in analysis (and signal processing), we use a 10-meter "zero-distance" balance, as shown in Fig. 4-11a. In the configuration shown, the target interferometer can exhibit two possible optical path differences: -4-meters, or +4-meters.

When we apply a delay, t_{offset}, that does not correspond to the target distance through eq. (4.6), it should be noted that the resampled target still exhibits some signal power in the vicinity of the corresponding bin. This indicates that there will be some significant amount of leakage into the oppositely-signed frequency bin in the DFT. This "conjugate leakage" represents two possible problems in terms of resolving range ambiguity. Firstly, conjugate leakage is most severe about the zero-distance. This is due to the fact that targets about zero-distance have conjugate leakage into adjacent synchronous windows. This represents a significant drawback of using this method for resolving ambiguity. Some analysis may be required to determine whether this method of ambiguity resolution is sufficient for a specific application. Secondly, conjugate leakage can increase the false-alarm rate for target detection as an inverse function of distance. Conjugate leakage can also occlude low-power targets, causing missed detection.

We analytically examined the effect of conjugate leakage for sinusoidal chirps. We note that the amount of conjugate leakage vs. range depends on the shape of optical frequency modulation. It may be possible to select and optimize waveforms in order to maximize conjugate-leakage-limited SNR, however we did not perform this optimization in this dissertation. Fig. 4-11 shows the conjugate suppression ratio in dB as a function of target distance. Three results are shown: first, an ideal case in which perfectly synchronous resampling is assumed (every possible delay is accounted for); second, a multi-synchronous resampling case with eight resampling windows; and third, a multi-synchronous resampling case with two resampling windows.

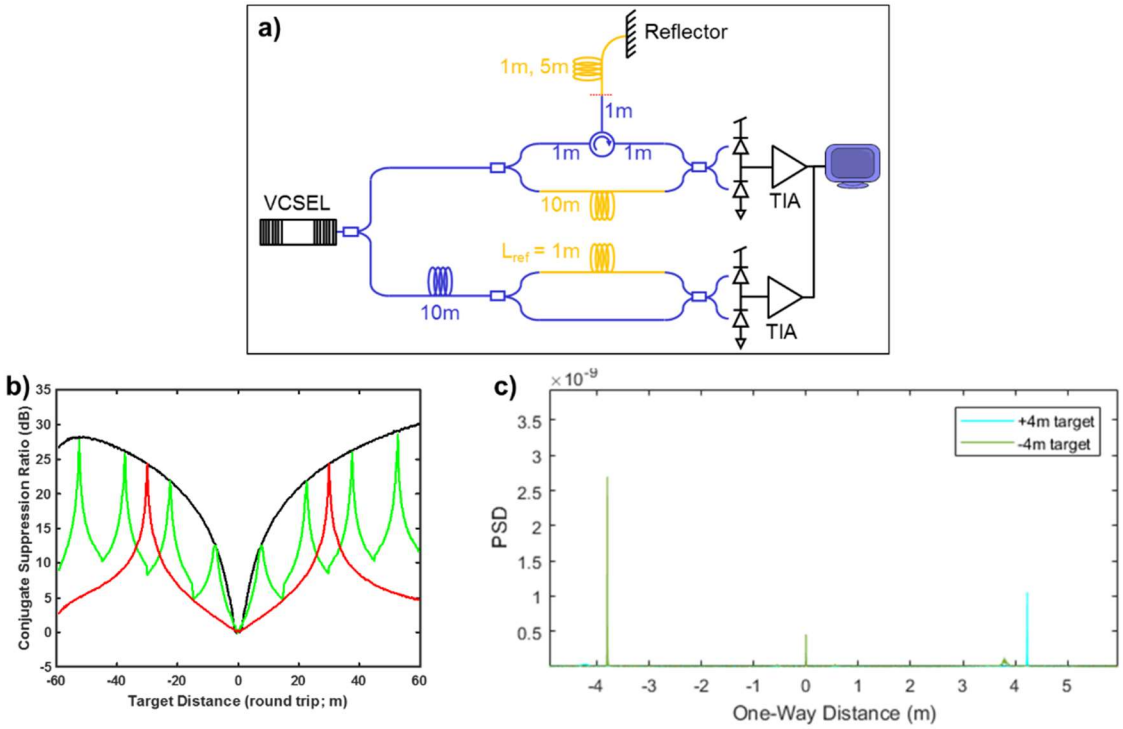

Fig. 4-11. Conjugate suppression through MK-resampling. a) System configuration for conjugate suppression experiment: the target interferometer has an asymmetry of +4-meters or -4-meters, and a 10-meter zero-distance balance is used to synchronize 1-meter targets with 1-meter reference; b) conjugate suppression ratio vs target distance for three synchronous cases: Case 1 (black solid line): perfectly synchronous resampling; this represents the best possible conjugate suppression ratio for every target distance. Case 2 (green solid line): MK-8 resampling; this shows that the ideal case can be approached with appropriately spaced MK windows. Case 3 (red solid line): MK-2 resampling; this case shows significant degradation in conjugate suppression ratio at target distances shorter than 13 meters. Each analysis performed with a reference length of 1-meter and offset of 30-meters, and the target's balance arm at 30-meters; c) experimental result for conjugate suppression through MK-resampling.

4.4 Phase Noise Reshaping in Resampling FMCW Systems

While MK-resampling can compensate for range-dependent signal broadening, the range may still be limited by laser phase noise. In this section, we describe the use of numerical Monte Carlo simulations to show that the signal-to-noise ratio for long range targets can be improved by using MK-resampling in conjunction with a long reference interferometer.

Linear FMCW lidar typically suffers from signal-to-noise ratio degradation as target distance increases. Noise on laser phase, usually due to spontaneous emission or tuning mechanisms, causes random fluctuation on the laser frequency. If the laser is used to probe an interferometer, as is the case in FMCW lidar, the interference signal at the output of the interferometer will experience random fluctuations related to the variance of the laser phase noise and the path length difference in the interferometer. Ultimately, this leads to an SNR-degradation with target distance, and defines a phase-noise-limited maximum range. We claim that the resampling technique extends the phase-noise-limited maximum range under particular conditions. We demonstrate 20-meter ranging (40-meter total path length) with millimeter accuracy using a laser with a coherence length of 30-meters.

Phase noise is often described by "laser linewidth," the optical spectral width of a single-wavelength source. This description assumes that the frequency noise of the laser has a uniform power spectral density. For analytical purposes in this dissertation, we will use this assumption about laser frequency noise, but we note that it is important to verify this assumption before

applying this analysis to other systems. Tuning mechanisms may have colored noise which could impact the phase noise performance of such systems.

4.4.1 Analytical Intuition

For an intuitive explanation of phase noise in resampling, we rely on the time-domain description of the FMCW beat signal, given below:

$$\begin{aligned} i(t) &\propto \cos\left(\Delta\phi(t,\tau)+\Delta\phi_n(t,\tau)\right) \\ &= \cos\left(\left[\phi(t)-\phi(t-\tau)\right]+\left[\phi_n(t)-\phi_n(t-\tau)\right]\right) \end{aligned} \tag{4.9}$$

One can deduce that for a given random laser phase fluctuation, $\phi_n(t)$, the noise difference term, $\Delta\phi_n(t,\tau)$, grows as a function of the time difference, τ. We note that the Hilbert transform phase-analysis yields a result that is the sum of the intended modulation (linear, sinusoidal, or otherwise) and a phase noise term (the statistics of which is dependent on the interferometer delay difference). If we assume that the phase noise in this photocurrent is dominated by the phase noise of the tunable laser source, we can assume that the phase noise terms on two different interferometers of the same length will be identical. We can use this principle to our advantage to reduce the effects of phase noise on the maximum range of FMCW systems.

In this dissertation, we will not outline a derivation of the power spectral density of the photocurrent with noise, but we refer readers to the result of analysis performed in [35], reproduced below:

$$S_i^o(\omega,T) = T\,\mathrm{sinc}^2\left(\frac{T\omega}{2}\right)e^{-\frac{2\tau}{\tau_c}} + \frac{\tau_c}{1+\left(\frac{\omega\tau_c}{2}\right)^2}\left\{1-e^{-\frac{2\tau}{\tau_c}}\left[\cos(\omega\tau)+\frac{2}{\omega\tau_c}\sin(\omega\tau)\right]\right\} \tag{4.10}$$

where T is the modulation ramp length in seconds, τ is the target delay in seconds, and τ_c is the coherence time of the laser source (defining the statistical parameters of white noise on laser phase). The "coherence time" is related to linewidth, $\Delta\nu$, through the relation, $\tau_c = 1/(\pi\Delta\nu)$. This analytical result for linear FMCW lidar shows that the windowed signal will exhibit sinc-shaped behavior, with a noise pedestal centered around the sinc's peak. We verify this result with Monte Carlo analysis using the assumption that laser frequency noise is a Gaussian random process (see Fig. 4-12). We can also use Monte Carlo analysis to model the effects of phase noise in resampling for targets at different lengths.

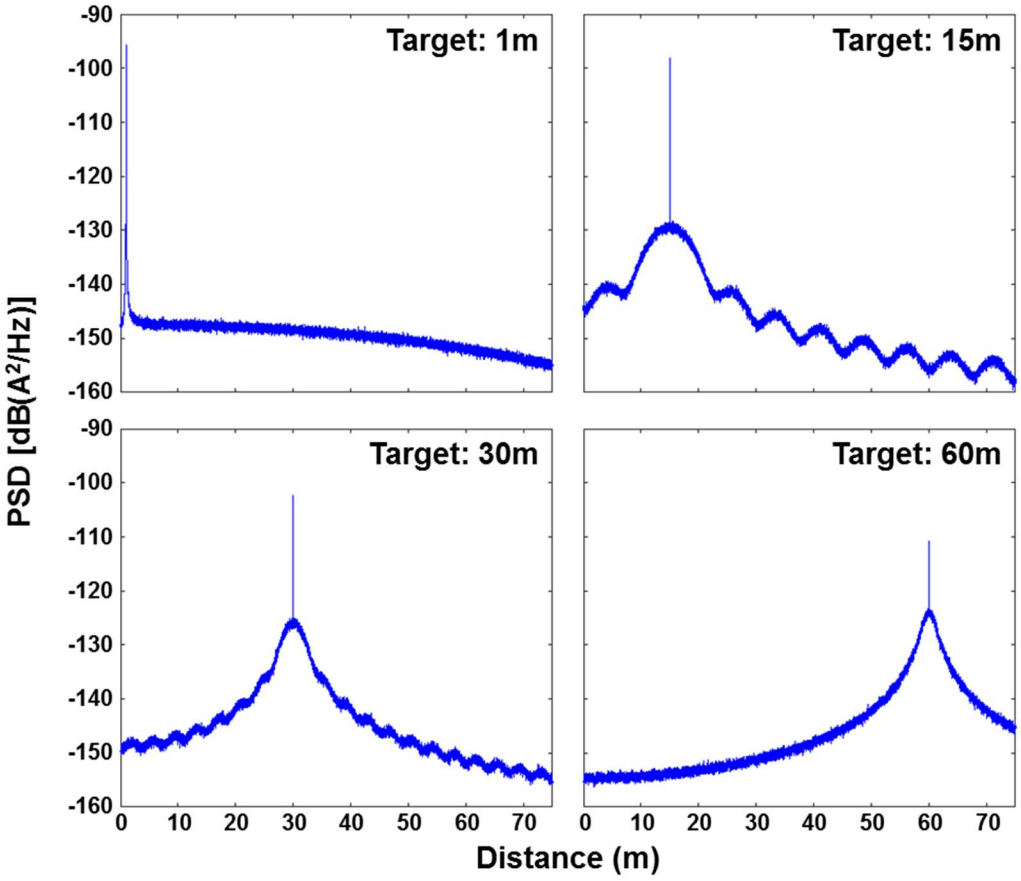

Fig. 4-12. Monte Carlo verification of laser phase noise effects on FMCW beats for linear sweep, targets at 1m, 15m, 30m, and 60m, for coherence length defined as 30m. We note that the typical definition of coherence length does not correspond to the phase-noise limited target length in an FMCW sense.

4.4.2 Proposed Phase Noise Suppression for Resampling using Long Reference Length

An important parameter in this resampling architecture is the choice of reference interferometer length. We have previously shown that the reference beat delay can be chosen arbitrarily and residual chirps on the target can be removed with MK-resampling. However, in the case of laser phase noise, reference interferometer length defines the spectral parameters of noise in the resampled target signal. Fig. 4-13(b-d) shows Monte Carlo model results for three choices of reference interferometer length.

We emphasize the selection of reference delay in the non-linear resampling architecture and propose that this parameter be selected to increase the phase-noise-limited range of non-linear FMCW lidar. This design calls for the selection of a reference interferometer length that is chosen to be as long as possible, such that phase-noise-limited SNR is recovered across an application-defined window.

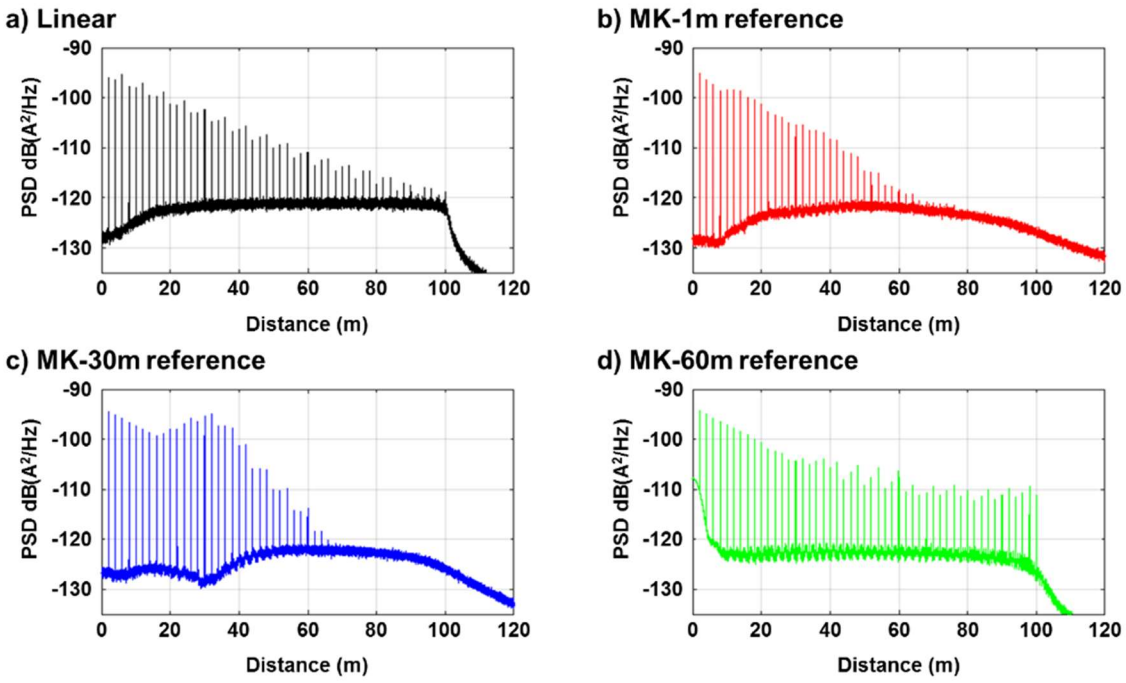

Fig. 4-13. Monte Carlo modeling of linear and non-linear FMCW beats with three different reference lengths; 50 simultaneous targets at 2-meter steps; coherence length modeled as 30-meters. a) Beat signals for linear modulation; b) MK-resampled targets for sinusoidal modulation and 1-meter reference; c) MK-resampled targets with 30-meter reference; d) MK-resampled targets with 60-meter reference.

In this section, we demonstrate the advantage of long-reference design in FMCW resampling systems by performing Monte Carlo parameter sweeps. In Section 4.4.4, we present imaging results using a long reference to recover repeatability and SNR for long-distance targets.

It is important to note that these improvements do not fully compensate for all laser phase noise effects. Using a long-reference is important when considering lidar ranging at distances comparable to the coherence length of the tunable laser. This work does not obviate the need to design lasers with inherently longer coherence length, nor does it replace the need for other high-bandwidth feedback solutions for phase noise reduction. We propose that the long-reference resampling method ought to be used once the previous measures have been taken, in order to further extend the phase-noise-limited range of FMCW systems.

We performed several parameter-sweeps in a Monte Carlo modeling framework, under the following conditions: 1) The laser frequency sweep is sinusoidal; 2) laser frequency noise has a white spectrum; 3) other noise sources, such as receiver thermal or shot noise, are neglected; and, 4) optical losses are assumed to be zero.

In the following parameter sweeps, we apply a certain modulation characteristic (sinusoidal shape, 4KHz modulation frequency, and 100GHz laser modulation depth/laser frequency excursion) and a fixed reference length with associated signal conditioning parameters. The target length parameter is simulated at 50 different fixed lengths, as shown in Fig. 4-13. For each step of the reference length parameter, we perform 100 numerical simulations with phase noise, apply dense MK-resampling to each, and perform a simple peak-analysis on the resampled spectra to estimate peak location, peak power, and SNR. We expect that this Monte Carlo simulation framework gives results that converge to an underlying analytical phase-noise result. Further work is needed to derive an analytical relationship between SNR/precision and phase noise models for sinusoidal modulation with resampling.

In Fig. 4-14, we show the results of Monte Carlo parameter sweeps. First, we show lidar accuracy, defined as the standard deviation of peak location for 100 simulations, mapped over reference length and target length. Second, we show phase-noise limited SNR for those same simulations, in which signal power is defined as the peak value and noise power is defined as the average value in the neighborhood of the peak. We show these parameter sweeps for both standard k-clock resampling and MK resampling.

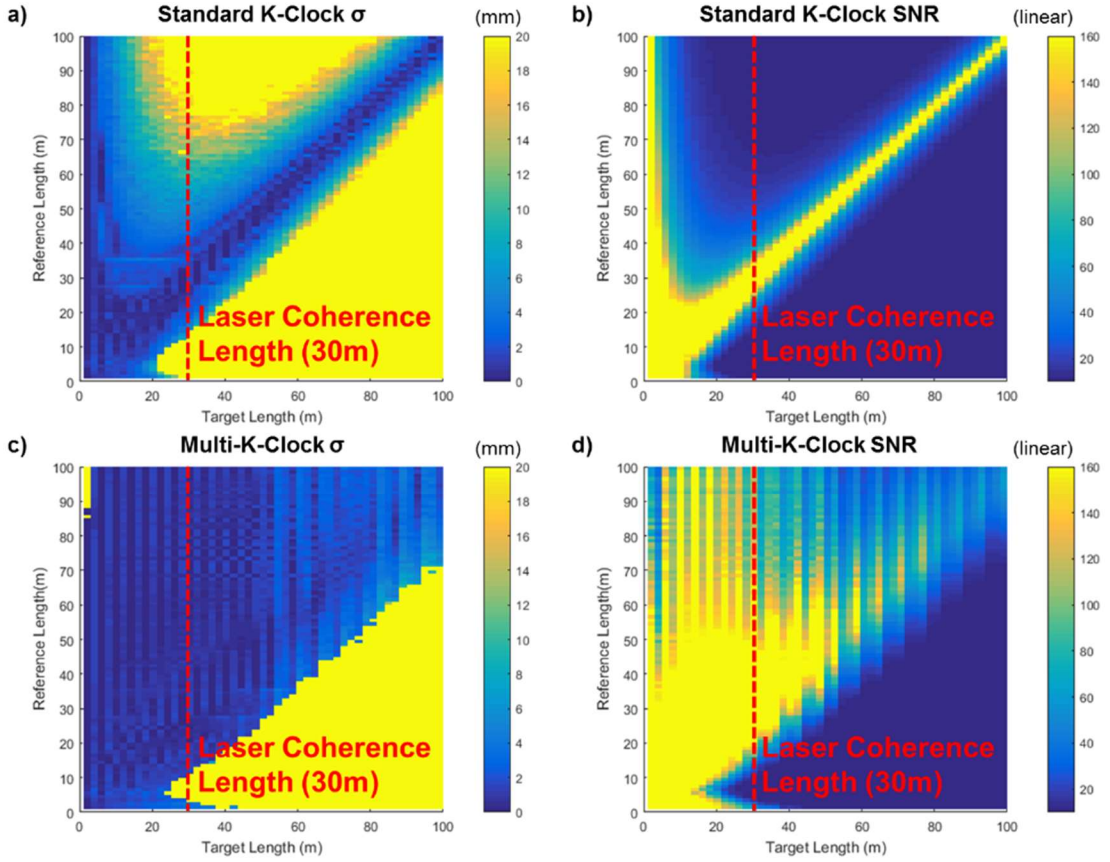

Fig. 4-14. Accuracy and SNR vs. reference and target length. For a given reference length, we also plot the worst-case accuracy (maximum standard deviation) and worst-case SNR (minimum SNR) over the simulated target lengths to illustrate a simple phase-noise-minded design process.

4.4.3 Analysis of Noise in Long-Reference Resampling

The method of resampling in non-linear FMCW lidar fits into a category of range-finding techniques where the frequency of the laser is tracked with some accuracy. In our implementation, we are using a Mach-Zhender Interferometer to infer the laser frequency. The phase at the output of an MZI with known asymmetry will ideally be proportional to the frequency of the laser. With the addition of laser noise and MZI drift, noise and drift appear on the phase of the MZI beat, causing an error in the frequency-tracking capability of the MZI resampling architecture. Since we are using the phase of the MZI to resample the target MZI signal, noise and error on the frequency-track will correspond to a jitter in the sampling of the target signal.

The phase of an MZI beat signal with delay τ_{ref} is given as:

$$\Delta\phi_{beat}(t,\tau_{ref}) = \phi_0(t) - \phi_0(t-\tau_{ref}) + \phi_n(t) - \phi_n(t-\tau_{ref}) \tag{4.11}$$

Where $\phi_0(t)$ is the laser phase, and $\phi_n(t)$ is the laser phase noise process. We can estimate the relative laser frequency by dividing $\Delta\phi_{beat}(t,\tau_{ref})$ by τ_{ref}, so

$$\widetilde{\omega}_{laser}(t,\tau_{ref}) = \frac{\Delta\phi_{beat}(t,\tau_{ref})}{\tau_{ref}} = \frac{\phi_0(t)-\phi_0(t-\tau_{ref})}{\tau_{ref}} + \frac{\phi_n(t)-\phi_n(t-\tau_{ref})}{\tau_{ref}} \quad (4.12)$$

We note that this calculation is an approximation of the derivative of laser phase, which should be proportional to laser frequency. It is evident that this estimate of instantaneous laser frequency will exhibit error if the phase noise derivative approximation is inaccurate. We will leave this term present in the analysis to include its effects.

Similar to the reference MZI beat signal, the phase of a target MZI beat signal with delay τ_1 is given as:

$$\Delta\phi_{beat}(t,\tau_1) = \phi_0(t) - \phi_0(t-\tau_1) + \phi_n(t) - \phi_n(t-\tau_1) \quad (4.13)$$

And the relative laser frequency is calculated as:

$$\widetilde{\omega}_{laser}(t,\tau_1) = \frac{\Delta\phi_{beat}(t,\tau_1)}{\tau_1} = \frac{\phi_0(t)-\phi_0(t-\tau_1)}{\tau_1} + \frac{\phi_n(t)-\phi_n(t-\tau_1)}{\tau_1} \quad (4.14)$$

We are interested in the difference between the estimate from the reference and the estimate from the target, since this will yield a difference in the resampling of the reference and the target beat signals. Thus, we take the difference of eqs. (4.12) and (4.14),

$$\Delta\widetilde{\omega}(t,\tau_1) = \widetilde{\omega}_{laser}(\tau_{ref}) - \widetilde{\omega}_{laser}(\tau_1) = \phi_0(t)\left[\frac{1}{\tau_{ref}} - \frac{1}{\tau_1}\right] - \left[\frac{\phi_0(t-\tau_{ref})}{\tau_{ref}} - \frac{\phi_0(t-\tau_1)}{\tau_1}\right] + \phi_n(t)\left[\frac{1}{\tau_{ref}} - \frac{1}{\tau_1}\right] - \left[\frac{\phi_n(t-\tau_{ref})}{\tau_{ref}} - \frac{\phi_n(t-\tau_1)}{\tau_1}\right] \quad (4.15)$$

The first terms with $\phi_0(t)$ only sum to zero if the low-order Taylor expansion of $\phi_0(t)$ is well-behaved, but in general is a systematic difference that can be removed with predistortion or calibration. If the laser is linearly modulated, this sum is identically zero, but, in fact, the multi-synchronous method outlined in previous chapters reduces this sum for sinusoidal $\phi_0(t)$, for which the Taylor expansion is not well-behaved. For noise analysis, we will neglect the systematic terms, and treat only the noise terms, assuming that methods can be used to remove non-linearities actively or in post-processing. We define the noise term as,

$$\Delta\widetilde{\omega}_n(t,\tau_1) = \phi_n(t)\left[\frac{1}{\tau_{ref}} - \frac{1}{\tau_1}\right] - \left[\frac{\phi_n(t-\tau_{ref})}{\tau_{ref}} - \frac{\phi_n(t-\tau_1)}{\tau_1}\right] \quad (4.16)$$

We aim to characterize the noise on this frequency, and characterize it as a jitter in resampling the target signal. Therefore, we analyze the variance of this random process. We will refer to the definition of auto-correlation given by eq. (4.17) below:

$$R_x(u) = \langle x(t)x(t-u)\rangle_t \quad (4.17)$$

First, we examine the auto-correlation of the signal in eq. (4.16):

$$R_{\Delta\widetilde{\omega}_n}(s,\tau_1) = \langle\Delta\widetilde{\omega}_n(t,\tau_1)\Delta\widetilde{\omega}_n(t-s,\tau_1)\rangle_t \quad (4.18)$$

$$R_{\Delta\widetilde{\omega}_n}(s,\tau_1) = (a_1^2+a_2^2+a_3^2)R_{\phi_n}(s) - a_1a_2\left[R_{\phi_n}(s+\tau_{ref}) + R_{\phi_n}(s-\tau_{ref})\right] + a_1a_3\left[R_{\phi_n}(s+\tau_1) + R_{\phi_n}(s-\tau_1)\right] - a_2a_3\left[R_{\phi_n}(s+\tau_1-\tau_{ref}) + R_{\phi_n}(s+\tau_{ref}-\tau_1)\right] \quad (4.19)$$

where we have used $a_1 = \frac{1}{\tau_{ref}} - \frac{1}{\tau_1}$; $a_2 = 1/\tau_{ref}$; and $a_3 = 1/\tau_1$. The power spectral density for $\Delta\widetilde{\omega}_n$ is given:

$$S_{\Delta\widetilde{\omega}_n}(\omega,\tau_1) = \mathcal{F}_s\left[R_{\Delta\widetilde{\omega}_n}(s,\tau_1)\right] = S_{\phi_n}(\omega)\omega^2\left[\left(1 - \frac{\tau_{ref}}{\tau_1} + \frac{\tau_{ref}}{\tau_1}cos(\omega\tau_1)\right)sinc^2\left(\frac{\omega\tau_{ref}}{2}\right) + sinc^2\left(\frac{\omega\tau_1}{2}\right) - 2\,sinc(\omega\tau_1)\,sinc\left(\omega\tau_{ref}\right)\right] \quad (4.20)$$

$$S_{\Delta\tilde{\omega}_n}(\omega,\tau_1) = \Delta\omega\left[\left(1-\frac{\tau_{ref}}{\tau_1}+\frac{\tau_{ref}}{\tau_1}cos(\omega\tau_1)\right)sinc^2\left(\frac{\omega\tau_{ref}}{2}\right)+sinc^2\left(\frac{\omega\tau_1}{2}\right)-2\,sinc(\omega\tau_1)\,sinc\left(\omega\tau_{ref}\right)\right] \quad (4.21)$$

where we have used the assumption for spontaneous emission ($S_{\phi_n}(\omega) = \Delta\omega/\omega^2$ from eq. (3.23)). One can perform a simple check for this result by ensuring that the spectrum is identically zero when the target delay matches the reference delay. In order to find the variance of $\Delta\tilde{\omega}_n$, $\sigma^2_{\Delta\tilde{\omega}_n}$, we can integrate the PSD over all frequencies:

$$\sigma^2_{\Delta\tilde{\omega}_n}(\tau_1) = \frac{1}{2\pi}\int_{-\infty}^{\infty} S_{\Delta\tilde{\omega}_n}(\omega,\tau_1)d\omega \quad (4.22)$$

$$\sigma^2_{\Delta\tilde{\omega}_n}(\tau_1) = \Delta\omega\left(\frac{1}{\tau_{ref}}+\frac{|\tau_1-\tau_{ref}|-|\tau_1|}{\tau_1\tau_{ref}}\right) \quad (4.23)$$

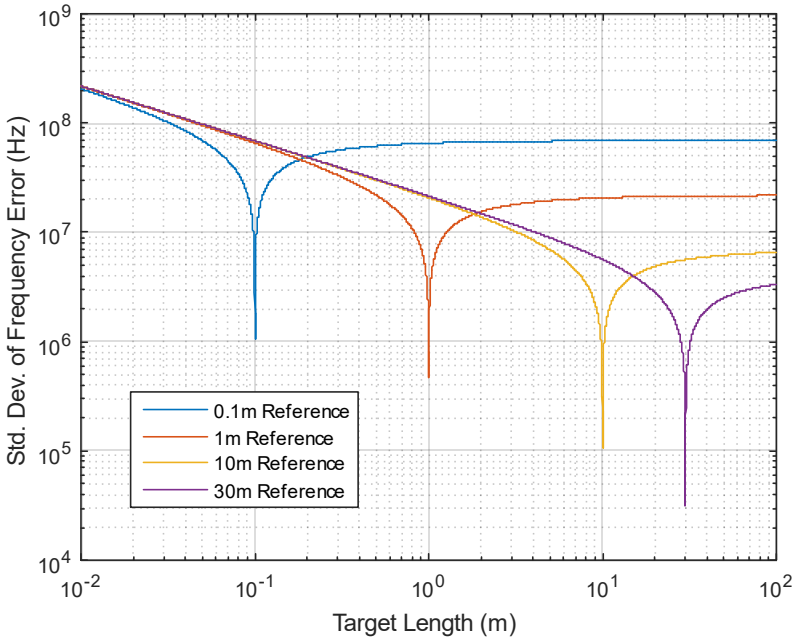

Fig. 4-15. Frequency-tracking error as a function of reference length and target length. This "error" represents the deviation of the laser frequency estimate made via the reference interferometer and the laser frequency estimate made via a target interferometer. If the deviation between the estimates is low, this indicates that the effective linear phase noise on the target signal will be small. If the deviation between the estimates is high, this indicates a high effective linear phase noise on the target signal.

Noise on the frequency estimates made via reference and target interferometer can be represented by phase noise. Consider a beat signal represented in the real time domain:

$$s(t,\tau_{ref}) = cos\left(\Delta\phi_{beat}(t,\tau_{ref})\right) \quad (4.24)$$

Under resampling, the reference is transformed to have a perfectly linear phase at each sample, so we can represent the signal in the resampled time domain:

$$s(t',\tau_{ref}) = cos\left(\Delta\phi_{beat}(t',\tau_{ref})\right) = cos(a_0\tau_{ref}t' + b_0\tau_{ref}) \quad (4.25)$$

Where $a_0\tau_{ref}$ represents the frequency after resampling, $a_0\tau_{ref} = 2\pi\frac{B}{T}\tau_{ref}$, and b_0 represents a beat phase offset after resampling. The resampled target signal can be written in the resampled time domain:

$$s(t', \tau_{targ}) = cos\left(\Delta\phi_{beat}(t', \tau_{targ})\right) = cos(a_0\tau_{targ}t' + b_0\tau_{targ} + \Delta\tilde{\omega}_n(t', \tau_{targ}, \tau_{ref}) \cdot \tau_{targ}) \quad (4.26)$$

In order to find spectrum of the FMCW photocurrent after resampling, we will examine the noise term in eq. (4.26). We will first calculate the autocorrelation of the signal, by plugging eq. (4.26) into eq. (4.17):

$$R_s(u) = \langle cos(a_0\tau_{targ}u + \Delta\tilde{\omega}_n(t', \tau_{targ}, \tau_{ref})\tau_{targ} - \Delta\tilde{\omega}_n(t' - u, \tau_{targ}, \tau_{ref})\tau_{targ})\rangle_{t'} \quad (4.27)$$

Defining $\theta(t, \tau_{tar}\ , \tau_{ref}) \equiv \Delta\tilde{\omega}_n(t, \tau_{targ}, \tau_{ref})\tau_{targ} - \Delta\tilde{\omega}_n(t - u, \tau_{targ}, \tau_{ref})\tau_{targ}$, and assuming that the random process $\Delta\tilde{\omega}_n(t, \tau_{targ}, \tau_{ref})$ possesses Gaussian statistics, we can write:

$$R_s(u) = cos(a_0\tau_{targ}u)\, exp\left(-\frac{\sigma_\theta^2(\tau_{targ}, \tau_{ref}, u)}{2}\right) \quad (4.28)$$

The baseband spectrum of the photocurrent is given by:

$$S_i^o(\omega) = \mathcal{F}_u\left\{exp\left(-\frac{\sigma_\theta^2(\tau_{targ}, \tau_{ref}, u)}{2}\right)\right\} \quad (4.29)$$

We can derive a useful identity for calculating the variance, $\sigma_\theta^2(\tau_{targ}, \tau_{ref}, u)$. First, we can define,

$$\sigma_{\Delta\tilde{\omega}_n}^2(u) = \langle[\omega_n(t) - \omega_n(t-u)]^2\rangle_t = 2\sigma_{\omega_n}^2 - 2\langle\omega_n(t)\omega_n(t-u)\rangle_t \quad (4.30)$$

We can find an expression for the autocorrelation of $\omega_n(t)$ by re-arranging eq. (4.30):

$$R_{\omega_n}(u) = \langle\omega_n(t)\omega_n(t-u)\rangle_t = \sigma_{\omega_n}^2 - \frac{\sigma_{\Delta\tilde{\omega}_n}^2(u)}{2} \quad (4.31)$$

We can write the autocorrelation of $\Delta\tilde{\omega}_n$ by plugging in eq. (4.16) into eq. (4.17),

$$R_{\Delta\tilde{\omega}_n}(s, u) = \frac{\sigma_{\Delta\tilde{\omega}_n}^2(s+u)}{2} + \frac{\sigma_{\Delta\tilde{\omega}_n}^2(s-u)}{2} - \sigma_{\Delta\tilde{\omega}_n}^2(s) \quad (4.32)$$

A useful identity is given by Vasilyev in [35]: $\sigma_\theta^2(\tau, u) = 2\sigma_{\Delta\tilde{\omega}_n}^2(\tau) - 2R_{\Delta\tilde{\omega}_n}(u, \tau)$. The variance of the process, $\theta(t, \tau_{targ}, \tau_{ref})$, can be calculated with by plugging in eq. (4.32) into the identity for variance and autocorrelation:

$$\sigma_\theta^2(\tau, u) = 2\sigma_{\Delta\tilde{\omega}_n}^2(\tau) + 2\sigma_{\Delta\tilde{\omega}_n}^2(u) - \sigma_{\Delta\tilde{\omega}_n}^2(u + \tau) - \sigma_{\Delta\tilde{\omega}_n}^2(u - \tau) \quad (4.33)$$

Finally, plugging the result of eq. (4.24) into eq. (4.33), we can write an expression for the variance of $\theta(t, \tau_{targ}, \tau_{ref})$,

$$\sigma_\theta^2(\tau, u) = \frac{2\Delta\omega}{\tau_{ref}}\left(1 + \frac{|\tau - \tau_{ref}| - |\tau|}{\tau}\right) + \frac{2\Delta\omega}{\tau_{ref}}\left(1 + \frac{|u - \tau_{ref}| - |u|}{u}\right) - \frac{\Delta\omega}{\tau_{ref}}\left(1 + \frac{|u + \tau - \tau_{ref}| - |u + \tau|}{(u+\tau)}\right) - \frac{\Delta\omega}{\tau_{ref}}\left(1 + \frac{|u - \tau - \tau_{ref}| - |u - \tau|}{(u-\tau)}\right) \quad (4.34)$$

$$\sigma_\theta^2(\tau, u) = \frac{\Delta\omega}{\tau_{ref}}\left[2\left|1 - \frac{\tau_{ref}}{\tau}\right| + 2\frac{|u - \tau_{ref}| - |u|}{u} - \frac{|u + \tau - \tau_{ref}| - |u + \tau|}{(u+\tau)} - \frac{|u - \tau - \tau_{ref}| - |u - \tau|}{(u-\tau)}\right] \quad (4.35)$$

We calculate the baseband photocurrent spectrum by plugging eq. (4.35) into eq. (4.29),

$$S_i^o(\omega) = exp\left(-\frac{\Delta\omega}{\tau_{ref}}\right) exp\left(\left|1 - \frac{\tau_{ref}}{\tau}\right|\right) \mathcal{F}_u\left\{exp\left(\frac{|u - \tau_{ref}| - |u|}{u}\right) exp\left(-\frac{|u + \tau - \tau_{ref}| - |u + \tau|}{2(u+\tau)}\right) exp\left(-\frac{|u - \tau - \tau_{ref}| - |u - \tau|}{2(u-\tau)}\right)\right\} \quad (4.36)$$

We can consider so-called "cycle-jitter" on this signal, which is represented by a random fluctuation on $n\Delta t$:

$$s[n] = cos(\omega_0[n\Delta t + \delta t]) = cos(\omega_0 n\Delta t + \omega_0\delta t) \quad (4.37)$$

In this formulation, $\omega_0 \delta t$ represents the phase noise term. In the resampling method, we are using the reference MZI frequency estimate to re-sample the target signal. If we assume that the target is synchronized with the reference prior to the resampling step (which is not necessarily the case for multi-synchronous resampling), we can estimate the jitter-induced phase noise on the resampled target signal.

The spectral noise floor due to jitter is approximately the spectrum of the phase noise term, $\omega_0 \delta t$, for the example above. In the case of frequency-estimation via reference MZI, the radial frequency of the signal is given by:

$$\omega_0 = \frac{2\pi N}{T} = \frac{2\pi \Delta f_{laser} \tau_{ref}}{T} \tag{4.38}$$

Jitter on the frequency estimate manifests itself in the following manner:

$$s[n] = cos\left(\frac{2\pi \Delta f_{laser} \tau_{ref}}{T}[n\Delta f + \delta f]\right) = cos\left(\frac{2\pi \Delta \ _{laser} \tau_{ref}}{T} n\Delta f + \frac{2\pi \Delta f_{laser} \tau_{ref}}{T} \delta f\right) \tag{4.39}$$

Therefore, frequency-estimate-jitter will have a spectrum related to:

$$\frac{2\pi \Delta f_{laser} \tau_{ref}}{T} \delta f \tag{4.40}$$

where δf is the random variable represented by the standard deviation given previously.

4.4.4 Long Reference Resampling System Characterization and 3D Image Scans

We designed an experiment using a 30-meter reference with multiple target distances to demonstrate the effectiveness of the long-reference in MK-resampling (Configuration 3). Fig. 4-16 shows our experiment modified so that the target interferometer includes a fiber retro-reflector with two different fiber delays (21m fiber, or 1m fiber by removing the auxiliary fiber).

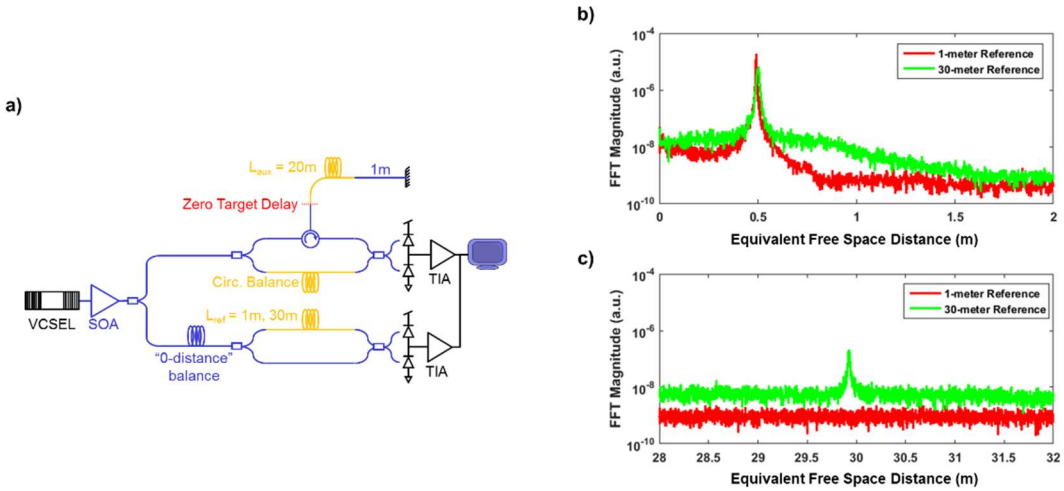

Fig. 4-16. Experiment for long-reference resampling. a) Experimental configuration for short reference resampling (L_{ref} is 1m fiber) and long reference resampling (L_{ref} is 30m fiber). Fiber retroreflector target is adjusted between 1m and 21m lengths with an auxiliary fiber. b) Range spectra for 1m target with 1m and 30m reference; c) Range spectra for 21m target. The long-reference results show that we can resolve targets at distances >20-meters in fiber, whereas the 1-meter reference cannot be used to resolve long-distance targets.

We can perform similar measurements, but replace the CFBG with focusing and scanning optics to perform 2-D imaging at long distance. Results in Fig. 4-17 show 3D point cloud acquisition with >20-meter standoff distance and millimeter-scale precision. These results demonstrate the possibility of using this system to acquire high depth-resolution 3D point clouds over a 20-meter range (40-meter total path length) using a tunable laser with coherence length <30-meters.

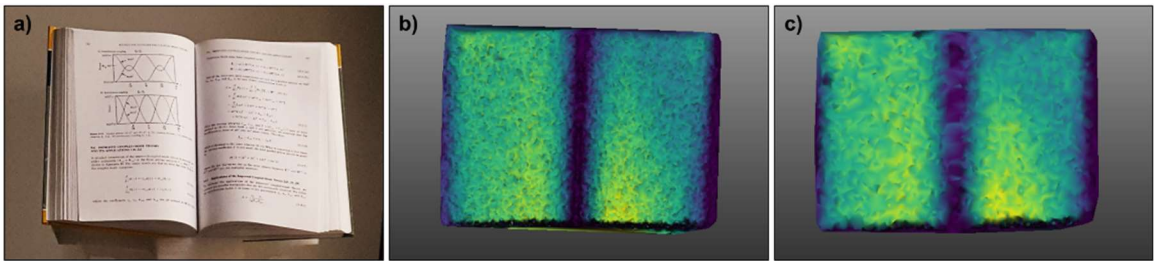

Fig. 4-17. Spot-size-limited imaging with 30-meter fiber reference; a) photograph of textbook object; b) 3D rendering of textbook at 1.5-meter standoff; c) 3D rendering of textbook at 22-meter standoff. Only adjustments to lidar system between 1-meter and 20-meter image are scanning x-y resolution and focal distance.

5 Summary, Outlook and Open Questions

5.1 Summary

In this dissertation, we have covered several topics and results in detail. Primary outcomes of this work include comprehensive FMCW link SNR analysis with ambient noise and laser phase noise, comprehensive phase noise simulation, OPLL design and verification for use in FMCW systems, implementation of k-clock resampling for non-linear FMCW imaging, simulation verification for new "multi-k-clock" methods, and experimental proof-of-concept for the use of multi-k-clock methods in long range, high resolution non-linear FMCW imaging.

5.2 Discussion and Future Work in OPLL Techniques and Chip-Scale Integration for FMCW Imaging

We have shown the successful implementation of an optoelectronic phase locked loop using integrated photonics and electronics. The OPLL is critical to achieving a linear frequency ramp over a short period of a few microseconds, and maintaining precise range measurements while laser conditions drift over hours. Integration of OPLL components at the chip scale demonstrates the potential to develop a compact FMCW system.

Integration may also lead to other benefits not addressed by this dissertation. In particular, the OPLL demonstrated herein is bandwidth-limited primarily due to path delay in fiber components. Reducing this delay increases the bandwidth of the OPLL, enabling the use of lasers with poorer linewidth in coherent imaging systems. Integration of laser and semiconductor amplifier components onto the photonics platform can reduce fiber delay, in addition to making the system significantly more compact. After integration of these components, the system will likely reach electronic noise and bandwidth limits of the packaging process. The TSVs presented in this work exhibit relatively high capacitance due to their large surface area, so other solutions would need to be explored to produce wafer-scale integrable photonic-to-electronic interconnects. An example of promising work in this area is presented in [45], in which 3fF parasitic capacitance is achieved with "through-oxide-vias" (TOVs).

Going forward, OPLLs will be important for two primary reasons: first, to reduce the need for and relax the requirements of complex signal post-processing (e.g., k-clock resampling and its variants presented in Chapter 4), and to make marginal improvements on the maximum range of FMCW sensors with significant phase noise. Flexible OPLL platforms with loop parameters that can be software-controlled will be important to the development of commercial FMCW systems that can tolerate large variations in laser performance. I envision that these optoelectronic systems will be critical in the monitoring of lasers in high-precision systems, thus they are critical tools for making high-precision depth sensors robust over long product lifetimes.

5.3 Discussion and Future Work in Resampling Methods for FMCW Imaging

Resampling methods for FMCW lidar have been implemented in several instantiations to achieve very high precision with extremely long range [46,47] with application in metrology. In addition, short range (0.1m to 2m), very high resolution resampling systems have been demonstrated in the field of SS-OCT [17,18], with application in medical diagnostics. In this study, we have demonstrated the use of an inexpensive thermally tunable laser with low coherence length in a resampling FMCW lidar sensor with >20m range and millimeter-scale precision for applications in consumer grade automation technology.

Using a standard k-clock resampling algorithm, we demonstrate an FMCW lidar scanning tool with sub-millimeter precision and a range of 1.4 meters using a non-linearly tuned VCSEL. Extending the system to accommodate faster acquisition rates causes significant degradation in

maximum range with the standard k-clock resampling algorithm. The "multi-k-clock" resampling algorithm compensates for this degradation and extends the range of the non-linear FMCW system to a noise-limited regime, while maintaining sub-millimeter precision. In addition, use of long-reference multi-k-clock resampling promises to extend the laser-phase-noise-limited range of non-linear FMCW lidar to free-space distances of 20-meters using lasers with coherence lengths of 30-meters. We expect that implementation of each of these solutions (standard k-clock resampling, multi-k-clock resampling, and long-reference resampling) will be necessary to the development of highly-capable and cost-effective FMCW lidar sensors.

Non-linear tuning characteristics exhibit adverse effects on simple resampling methods with increased modulation frequency and increased target distance. Absolute methods for tracking laser frequency, such as [46], eliminate most of the adverse dependence on modulation frequency and target distance. SS-OCT literature has addressed non-linearities due to receiver RF phase distortion at high frequencies [17]. This work shows that modulation frequency and target distance must be considered when assessing the performance of resampling methods. MK-resampling or an equivalent processing method must be used to recover SNR and resolution at the longest target distances for non-linear FMCW systems.

The cost of FMCW and OCT systems can be dominated by the cost of the tunable laser sources. Previous work has studied non-linear resampling systems using expensive tunable lasers with long coherence length, thus laser phase noise in resampling systems were not extensively studied. This work demonstrates the use of a low-cost tunable laser with a very modest coherence length ~30-meters. This laser phase noise limit is typically cited as a fundamental limit for FMCW ranging sensors. However, as we have shown through numerical simulation and imaging demonstrations, long-reference resampling can remove some dependence on this laser phase noise. This work demonstrates that judicious design of a resampling system can have benefits in noise performance of FMCW systems in general. This feature of resampling methods deserves closer treatment in future work.

Fundamentally, fixed-acquisition rate FMCW systems exhibit a tradeoff between maximum range and resolution. For a given modulation rate, receiver acquisition rate determines the largest target frequency that can be detected, and thus limits the maximum range of the FMCW sensor. The frequency excursion can be reduced, thus increasing the maximum range of the sensor, but this is traded with the fundamental Fourier-limited resolution of the system, which is inversely proportional to the frequency excursion. Fortunately, the modulation rate and modulation depth are relatively flexible elements in an FMCW system with a free-running tunable laser. Therefore, systems without active feedback on tuning mechanisms, such as those presented in this dissertation and in previous studies [17,18,46] can be designed to take advantage of this tradeoff for many applications.

The free-running tunable VCSEL laser sources used in our resampling experiments and in [3,19,20] contrast with tunable sources implemented with active feedback to linearize the frequency sweep. Active feedback systems such as those implemented in [9,10] have shown success in laser phase noise reduction and non-linearity reduction. However, phase noise reduction of the lidar beat signal is typically limited to cases in which the active feedback has very high bandwidth (and thus expensive) [3] or when the target is at extremely long distances (and thus not immediately applicable to consumer-grade technology) [10]. Resampling methods attempt to reconcile non-linearity as a deterministic problem, thus removing some dependence on the tunable laser sweep characteristic of a given tunable laser. However, the performance of a resampling system in terms of resolution and maximum range does depend on the type of non-linearity

exhibited by the tunable laser. This dissertation demonstrates the performance limitations of a sinusoidally-tuned laser. However, a more general analysis of resampling methods including other non-linear tuning mechanisms (e.g., MEMS tunable lasers with parabolic wavelength excursion) can still be performed. In general, other non-linear tuning characteristics would require modification to the MK-resampling scheme presented in this dissertation.

References

1. S. Choi, F. Thalmayr, D. Wee, and F. Weig, "Advanced driver-assistance systems: Challenges and opportunities ahead | McKinsey & Company," https://www.mckinsey.com/industries/semiconductors/our-insights/advanced-driver-assistance-systems-challenges-and-opportunities-ahead.
2. D. Geronimo, A. M. Lopez, A. D. Sappa, and T. Graf, "Survey of Pedestrian Detection for Advanced Driver Assistance Systems," IEEE Trans. Pattern Anal. Mach. Intell. **32**, 1239–1258 (2010).
3. M. Kuehn, T. Hummel, and J. Bende, "Advanced Driver Assistance Systems for Trucks – Benefit Estimation from Real-Life Accidents," in (2011).
4. M. Gerla, E. K. Lee, G. Pau, and U. Lee, "Internet of vehicles: From intelligent grid to autonomous cars and vehicular clouds," in *2014 IEEE World Forum on Internet of Things (WF-IoT)* (2014), pp. 241–246.
5. J. Levinson, J. Askeland, J. Becker, J. Dolson, D. Held, S. Kammel, J. Z. Kolter, D. Langer, O. Pink, V. Pratt, M. Sokolsky, G. Stanek, D. Stavens, A. Teichman, M. Werling, and S. Thrun, "Towards fully autonomous driving: Systems and algorithms," in *2011 IEEE Intelligent Vehicles Symposium (IV)* (2011), pp. 163–168.
6. G. R. Widmann, M. K. Daniels, L. Hamilton, L. Humm, B. Riley, J. K. Schiffmann, D. E. Schnelker, and W. H. Wishon, *Comparison of Lidar-Based and Radar-Based Adaptive Cruise Control Systems* (SAE Technical Paper, 2000).
7. R. Leitgeb, C. K. Hitzenberger, and A. F. Fercher, "Performance of fourier domain vs. time domain optical coherence tomography," Opt. Express **11**, 889–894 (2003).
8. R. F. Spaide, H. Koizumi, and M. C. Pozonni, "Enhanced Depth Imaging Spectral-Domain Optical Coherence Tomography," Am. J. Ophthalmol. **146**, 496–500 (2008).
9. S. R. Chinn, E. A. Swanson, and J. G. Fujimoto, "Optical coherence tomography using a frequency-tunable optical source," Opt. Lett. **22**, 340–342 (1997).
10. C. A. Puliafito, M. R. Hee, C. P. Lin, E. Reichel, J. S. Schuman, J. S. Duker, J. A. Izatt, E. A. Swanson, and J. G. Fujimoto, "Imaging of Macular Diseases with Optical Coherence Tomography," Ophthalmology **102**, 217–229 (1995).
11. T. V. Flügge, S. Schlager, K. Nelson, S. Nahles, and M. C. Metzger, "Precision of intraoral digital dental impressions with iTero and extraoral digitization with the iTero and a model scanner," Am. J. Orthod. Dentofacial Orthop. **144**, 471–478 (2013).
12. R. Myllylä, J. Marszalec, J. Kostamovaara, A. Mäntyniemi, and G.-J. Ulbrich, "Imaging distance measurements using TOF lidar," J. Opt. **29**, 188 (1998).
13. M. A. Itzler, M. Entwistle, S. Wilton, I. Kudryashov, J. Kotelnikov, X. Jiang, B. Piccione, M. Owens, and S. Rangwala, "Geiger-Mode LiDAR: From Airborne Platforms To Driverless Cars," in *Imaging and Applied Optics 2017 (3D, AIO, COSI, IS, MATH, pcAOP) (2017), Paper ATu3A.3* (Optical Society of America, 2017), p. ATu3A.3.
14. R. Knowlton, *Airborne Ladar Imaging Research Testbed* (MASSACHUSETTS INST OF TECH LEXINGTON LINCOLN LAB, MASSACHUSETTS INST OF TECH LEXINGTON LINCOLN LAB, 2011).
15. R. Whyte, L. Streeter, M. J. Cree, and A. A. Dorrington, "Application of lidar techniques to time-of-flight range imaging," Appl. Opt. **54**, 9654–9664 (2015).
16. C. S. Bamji, P. O'Connor, T. Elkhatib, S. Mehta, B. Thompson, L. A. Prather, D. Snow, O. C. Akkaya, A. Daniel, A. D. Payne, T. Perry, M. Fenton, and V.-H. Chan, "A 0.13 #x03BC;m CMOS System-on-Chip for a 512 #x00D7; 424 Time-of-Flight Image Sensor

With Multi-Frequency Photo-Demodulation up to 130 MHz and 2 GS/s ADC," IEEE J. Solid-State Circuits **50**, 303–319 (2015).
17. Z. Wang, B. Potsaid, L. Chen, C. Doerr, H.-C. Lee, T. Nielson, V. Jayaraman, A. E. Cable, E. Swanson, and J. G. Fujimoto, "Cubic meter volume optical coherence tomography," Optica **3**, 1496–1503 (2016).
18. S. Song, J. Xu, and R. K. Wang, "Long-range and wide field of view optical coherence tomography for in vivo 3D imaging of large volume object based on akinetic programmable swept source," Biomed. Opt. Express **7**, 4734–4748 (2016).
19. J. Xi, L. Huo, J. Li, and X. Li, "Generic real-time uniform K-space sampling method for high-speed swept-Source optical coherence tomography," Opt. Express **18**, 9511–9517 (2010).
20. K. Wang, Z. Ding, T. Wu, C. Wang, J. Meng, M. Chen, and L. Xu, "Development of a non-uniform discrete Fourier transform based high speed spectral domain optical coherence tomography system," Opt. Express **17**, 12121–12131 (2009).
21. J. C. Hulme, J. K. Doylend, M. J. R. Heck, J. D. Peters, M. L. Davenport, J. T. Bovington, L. A. Coldren, and J. E. Bowers, "Fully integrated hybrid silicon free-space beam steering source with 32-channel phased array," in (2014), Vol. 8989, pp. 898907-898907–15.
22. D. N. Hutchison, J. Sun, J. K. Doylend, R. Kumar, J. Heck, W. Kim, C. T. Phare, A. Feshali, and H. Rong, "High-resolution aliasing-free optical beam steering," Optica **3**, 887–890 (2016).
23. J. Sun, E. shah Hosseini, A. Yaacobi, D. B. Cole, G. Leake, D. Coolbaugh, and M. R. Watts, "Two-dimensional apodized silicon photonic phased arrays," Opt. Lett. **39**, 367 (2014).
24. L. Eldada, T. Yu, and A. Pacala, "Solid state optical phased array lidar and method of using same," U.S. patent US20150293224 A1 (October 15, 2015).
25. B. Schwarz, "LIDAR: Mapping the world in 3D," Nat. Photonics **4**, 429–430 (2010).
26. F. Aflatouni, B. Abiri, A. Rekhi, and A. Hajimiri, "Nanophotonic coherent imager," Opt. Express **23**, 5117 (2015).
27. Z. Wang, H.-C. Lee, D. Vermeulen, L. Chen, T. Nielsen, S. Y. Park, A. Ghaemi, E. Swanson, C. Doerr, and J. Fujimoto, "Silicon photonic integrated circuit swept-source optical coherence tomography receiver with dual polarization, dual balanced, in-phase and quadrature detection," Biomed. Opt. Express **6**, 2562–2574 (2015).
28. B. Aull, "Geiger-Mode Avalanche PHotodiodes for Three-Dimensional Imaging," Linc. Lab. J. **13**, (2002).
29. P. Qiao, G.-L. Su, Y. Rao, M. C. Wu, C. J. Chang-Hasnain, and S. L. Chuang, "Comprehensive model of 1550 nm MEMS-tunable high-contrast-grating VCSELs," Opt. Express **22**, 8541–8555 (2014).
30. W. Yang, Y. Rao, C. Chase, M. C. Huang, and C. Chang-Hasnain, "Linewidth Measurement of 1550 nm High Contrast Grating MEMS-VCSELs," in *CLEO: 2013 (2013), Paper CF2F.4* (Optical Society of America, 2013), p. CF2F.4.
31. Y. Matsui, W. Li, H. Roberts, H. Bulthuis, H. Deng, L. Lin, and C. Roxlo, "Transceiver for NG-PON2: Wavelength tunablity for burst mode TWDM and point-to-point WDM," in *2016 Optical Fiber Communications Conference and Exhibition (OFC)* (2016), pp. 1–3.
32. A. Vasilyev, N. Satyan, G. Rakuljic, and A. Yariv, "Terahertz Chirp Generation Using Frequency Stitched VCSELs for Increased LIDAR Resolution," in (OSA, 2012), p. CF3C.1.

33. P. Sandborn, T. Hariyama, and M. C. Wu, "Resolution-Enhancement for Wide-Range Non-Linear FMCW Lidar using Quasi-Synchronous Resampling," in *Imaging and Applied Optics 2017 (3D, AIO, COSI, IS, MATH, pcAOP) (2017), Paper DW3F.3* (Optical Society of America, 2017), p. DW3F.3.
34. M. Nazarathy, W. V. Sorin, D. M. Baney, and S. A. Newton, "Spectral analysis of optical mixing measurements," J. Light. Technol. **7**, 1083–1096 (1989).
35. A. Vasilyev, "The optoelectronic swept-frequency laser and its applications in ranging, three-dimensional imaging, and coherent beam combining of chirped-seed amplifiers," phd, California Institute of Technology (2013).
36. B. Behroozpour, P. A. Sandborn, N. Quack, T.-J. Seok, Y. Matsui, M. C. Wu, and B. E. Boser, "Electronic-Photonic Integrated Circuit for 3D Microimaging," IEEE J. Solid-State Circuits (2016).
37. N. Satyan, W. Liang, and A. Yariv, "Coherence Cloning Using Semiconductor Laser Optical Phase-Lock Loops," IEEE J. Quantum Electron. **45**, 755–761 (2009).
38. M. Bagheri, F. Aflatouni, A. Imani, A. Goel, and H. Hashemi, "Semiconductor laser phase-noise cancellation using an electrical feed-forward scheme," Opt. Lett. **34**, 2979–2981 (2009).
39. N. Satyan, W. Liang, F. Aflatouni, A. Yariv, A. Kewitsch, G. Rakuljic, and H. Hashemi, "Phase-Controlled Apertures Using Heterodyne Optical Phase-Locked Loops," IEEE Photonics Technol. Lett. **20**, 897–899 (2008).
40. F. Aflatouni, "Electronically assisted relative and absolute phase control of semiconductor lasers :: University of Southern California Dissertations and Theses," http://digitallibrary.usc.edu/cdm/ref/collection/p15799coll127/id/675092.
41. N. Satyan, A. Vasilyev, G. Rakuljic, V. Leyva, and A. Yariv, "Precise control of broadband frequency chirps using optoelectronic feedback," Opt. Express **17**, 15991 (2009).
42. B. Razavi and R. Behzad, *RF Microelectronics* (Prentice Hall New Jersey, 1998), Vol. 1.
43. R. Going, T. J. Seok, J. Loo, K. Hsu, and M. C. Wu, "Germanium wrap-around photodetectors on Silicon photonics," Opt. Express **23**, 11975–11984 (2015).
44. T.-J. Ahn and D. Y. Kim, "Analysis of nonlinear frequency sweep in high-speed tunable laser sources using a self-homodyne measurement and Hilbert transformation," Appl. Opt. **46**, 2394–2400 (2007).
45. K. T. Settaluri, S. Lin, S. Moazeni, E. Timurdogan, C. Sun, M. Moresco, Z. Su, Y. H. Chen, G. Leake, D. LaTulipe, C. McDonough, J. Hebding, D. Coolbaugh, M. Watts, and V. Stojanović, "Demonstration of an optical chip-to-chip link in a 3D integrated electronic-photonic platform," in *ESSCIRC Conference 2015 - 41st European Solid-State Circuits Conference (ESSCIRC)* (2015), pp. 156–159.
46. E. Baumann, F. R. Giorgetta, J.-D. Deschênes, W. Swann, I. Coddington, and N. Newbury, "Comb-calibrated FMCW ladar for Ranging and Imaging," in (OSA, 2015), p. LM4F.1.
47. R. Reibel, N. Greenfield, T. Berg, B. Kaylor, P. Roos, Z. Barber, and D. Klumpar, "Ultra-Compact LADAR Systems for Next Generation Space Missions," AIAAUSU Conf. Small Satell. (2010).